Investigation of Focused Ion Beam/Scanning Electron Microscope parameters for Slice and View and Energy Dispersive X-ray Spectroscopy of Embedded Brain Tissue

Steffen Knut Fagerland

Abstract

This Thesis investigates the optimization of a Focused Ion Beam/Scanning Electron Microscope (FIB/SEM) Slice and View protocol of brain tissue. Using a Slice and View protocol in a Dualbeam instrument, the ion and electron beams are used in sequence to alternately mill and image the newly exposed surface of a predefined volume. This creates serial section images that may be used for 3D reconstruction. Research questions addressed include finding FIB parameters most beneficial for accurate milling of the tissue, use of different software strategies and image processing for 3D reconstruction of selected subsets enclosed within the volume sectioned, and the use of Energy Dispersive X-ray Spectroscopy for revealing the volume contents *a priori* of the Slice and View. The reults showed that FIB parameters of $30kV$ and $0.9nA$ provided sufficient accuracy and consistency; that the DAB labeling protocol provided characteristics easily identifiable of the morphology of selected interneurons which were reconstructed, but was difficult to use in a generalized semi-automatic reconstruction protocol; and a model created to test EDX tracing did show potential for its use to increase protocol efficiency by narrowing down the regions of interest of the FIB block.

Preface

Numerous people have contributed to events leading up to this Master Thesis, both by direct assistance during the writing and by inspiration through the years before cuminating in this thesis; I am very grateful for their contribution and I would like to highlight important events.

First and foremost, I would like to thank Professor Pawel Sikorski who in addition to initially granting me the Thesis, also gave me all the required training for the Dualbeam FIB/SEM, assisted with required MATLAB coding, and provided very insightful scientific input throughout the investigations. I am very grateful for his patience and guidance and for allowing me to investigate the EDX tracing potential. Also of high importance for the work conducted is Staff Engineer Ken Roger Ervik; mr. Ervik provided me with additional information and lessons of the capabilities of the the FIB, tutoring concerning the software used (Avizo Fire, ImageJ/Fiji), and provided helpful guidance when problems arose, even during long hours at the Nanolab. I also want to thank Marianne Sandvold for discussions and her insights regarding the use of FIB/SEM for 3D reconstructions of brain tissue. The work presented here has a strong foundation in the Master Theses of Ken Roger Ervik and Marianne Sandvold. I am also grateful for the assistance, discussions and brain tissue provided by Ph.D student Jørgen Sugar and Profesor Menno Witter, who saw the possibilities inherent in this technology for the investigation, mapping and 3D reconstruction of interneurons.

I would also like to thank Professor Shu-Itchi Okamoto and Dr. Scott McKercher for the internship at Sanford-Burnham Medical Research Insitute, where I was further inspired to pursue neurological reserach; and Brain Lee, Anthony Nutter and Rameez Zadi for teaching me the general laboratory procedures for the neuroscientific research. Also of inspiration was the time I spent in the lab of anna Blois at UiB, Haukeland, who introduced

me to the practise and importance of animal models. And finally back to the time I spent with Professor Rune Raudeberg who initially spawned the interest in the investigation of the brain and thus the field of Neuroscience.

Table of Contents

Abbreviations

BSE   =   Bacscattered Eletron

CPS   =   Counts Per Second

EDX   =   Energy Dispersive X-ray

FIB   =   Focused Ion Beam

IBID   =   Ion Beam Induced Deposition

GIS   =   Gas Injection System

ROI   =   Region Of Interest

SE   =   Secondary Electron

SEM   =   Scanning Electron Microscope

TEM   =   Transmission Electron Microscope

Chapter 1

Introduction

Visualizing what we cannot resolve with microscopes has been of interest since the invention of the optical microscope by Robert Hooke in 1665 [48]. But the diffraction limit discovered in 1896 sets bounds for the resolution required for highly detailed investigations [66]. Around the same time (1895), X-rays were discovered by Wilhelm Conrad Röntgen. The unknown origin of these 'X' rays with obvious similarities with light (shadows form the rays) were identified by Thomson as electrons in 1897 [85]. Further utilizing electrons allowed to transcend the optical diffraction limit with the invention of the Transmission Electron Microscope (TEM) around 1940 [12]. TEM utilizes the wave nature of electrons to obtain a much higher resolution than allowed by light. 3D rendering of entities within the images began in the 1950's with serial analysis of TEM images [1].

3D reconstruction of brain tissue started in the 1960's ([50]), and methods for reconstruction be obtained are diverse. All the methods have their strengths and weaknesses. This Thesis explores the use of a Dualbeam Focused Ion Beam Scanning/Electron Microscope (FIB/SEM) for 3D reconstruction of brain tissue in a 'Slice and View' protocol. This procedure uses an ion and an electron beam to alternately cut away and image a sample, and as such create serially aligned images to be used in 3D reconstructions.

The Thesis investigates optimization of this protocol. This includes investigation of FIB parameters for the most accurate slicing; aspects of embedding and labeling of brain tissue; reconstructions using software (FIJI and Avizo Fire), and data quality measurements using MATLAB. Lastly, the use of Energy Dispersive X-ray Spectroscopy (EDX) for preliminary mapping of the tissue to be sectioned was explored.

Neuroscience volume problem

How brain function influences our behavior has been of interest for almost 5000 years with The Edwin Smith surgical papyrus in ancient Egypt [2]. Interest for brain circuitry came with the connection meshes by Gerlach, which were contested by Santiago Ramón y Cajal who constructed circuit diagrams (method of Golgi) of the brain [21]. The paradigm shift of distinct regions of the neurons was shown histologically in the 1930's (membranous synaptic barrier [7, 9]). But since optical microscopy and can only follow scarsely labeled neurites ([48]), the resolution for the verification came with the TEM in the 1950's. The pre- and post-synaptic elements are separated with a synaptic cleft of $10 - 20nm$ [21].

The reconstruction of neuronal circuits may be one way we might understand human behavior [77]. But for the carthographic approach, the mindboggling estimated number of 100 billion neurons connected through 100 000 miles of axons at $10^{14} - 10^{15}$ synaptic connections sets the problem of mapping the 'connectome' in persepctive [78]. The mouse brain is smaller, but 76 billion neurons is still a challenge [45, 71]. (Another problem is that our present knowledge mostly concerns animal models, and we do not just have large mouse brains [21, 45]; but rapid fixation of post-mortem tissue can be done [70].) Detailed mapping of the brain might shead light on underlying connective mechanisms of cognitive illnesses and adverse effects, as they might be caused by e.g. misrouting of neuronal wires, and all may at some point be caused by structural variations [78, 90].

The complexity of the human brain predisposes that the information is gathered in subsets of the volume at a time. High quality reconstructions of the tissue with FIB/SEM is one approach. A number of optional approaches exists, some of which are described in **Sec. 2**.

Chapter 2

Volume rendering in Neuroscience

This section introduces volume rendering in Neuroscience. Entities of interest within brain tissue often has dimensions of $10 - 50nm$, thus the resolution of electron microscopy (EM) is required [6, 10, 78]. A primary distinction is between imaging by signals transitted through thin sections by Transmission Electron Microscopy (TEM) or by signals obtained from bulk surface interactions by Scanning Electron Microscopy (SEM). This section introduces approaches used for 3D reconstruction of brain tissue, and ends with an introduction to EDX in Life Science and 3D reconstructions.

3D reconstructions at the nano- and micro-scale concerns minimizing the information lost when collecting the data used in the regeneration. Different approaches and resolutions are shown in **Fig. 2.1**.

2 Photon Laser Scanning Microscopy

Despite the limitations in resolution, fluorescently labeled brain tissue is used e.g. in the sophisticated use of genetically modified mice expressing fluorescent proteins in subsets of cells (Brainbow mice [69]), and 3D reconstruction using 2 Photon Excitation Microscopy (2PE). The use of fluorescent microscopy allows selective excitation with a discrimination
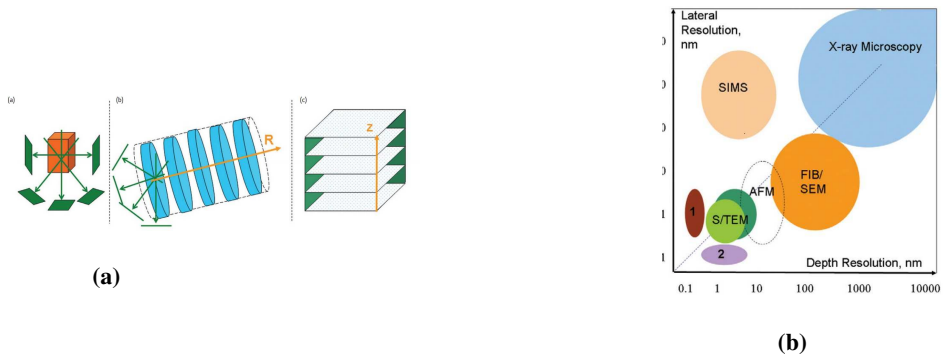
Figure 2.1: (a): different approaches to 3D reconstruction; (b): the obtainable resolution for different approaches (2007). In the figure, 1: atom probe tomography, 2: scanning transmission electron microscopy focal sectioning. Figures from [40].

sensitivity of 1 fluorescent molecule in 10^{11} non-fluorescent, and genetically encoded fluorescent proteins allows the labeling of most cellular structures [59]. 2PE uses two low energy photons (longer penetration depth) to excite a fluorophore in a non-linear process. This leads to modelcules being excited in a $1\mu m^3$ volume, thus also limiting the area exposed to photodamage [59].
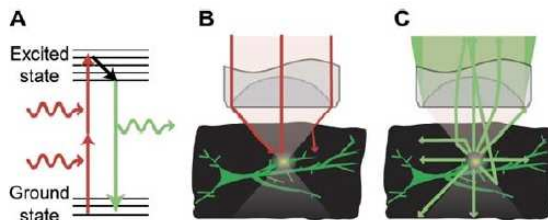
Figure 2.2: (a): simplified Jablonski diagram; (b): excitation beam focused to a diffraction limited spot; (c): isotropically emitted fluorescent photons. Figure from [59].

One approach scannned the xy plane and reconstructed cellular network dynamics in 3D with suplementary software [100]. Limitations of this technique includes that only the superficial layers (a few hundred μm) may be investigated [31, 59]. A benefit of using 2PLSM is that live cellular networks may be imaged, despite having a resolution limited to $(x, y) = 200nm$ and $z = 500nm$ [27]. 2PE may also be beneficial combined with other methods for 3D reconstruction.

TEM and ssTEM

The use of TEM within Neuroscience started in the 1950's [26, 50]. The resolution of TEM allows identification of all entities within the brain tissue, even quantification of synapses. The ultrastructure is revealed with a resolution of $0.1nm$. TEM uses thin slices ($40-90nm$) that allows highly accelerated ($80-120keV$) electrons to pass through the specimen [10]. The electron trajectories are deviated by selected labeled entities.
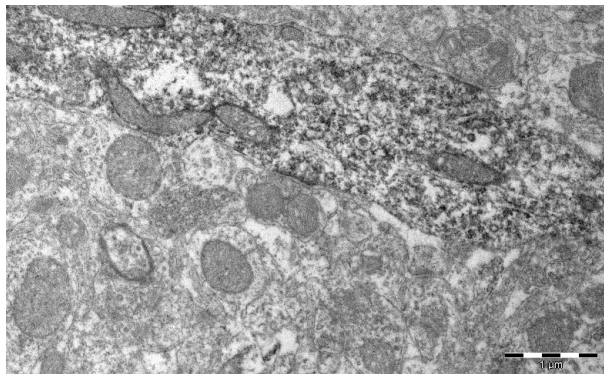

Figure 2.3: DAB labeled interneuron morphology cells visualized in a TEM micrograph. Figure, courtesy of Jørgen Sugar.

TEM is in general a 2D approach. Section thickness may be up to $0.5\mu m$, and nanometer resolutions are obtainable [35]. 3D rendering may be done by ultramicrotoming multiple sequential sections and reconstructing the image stack; serial section TEM (ssTEM). ssTEM may be used for reconstructing volumes of neuropil at the nanometer level, and can be used to study ultrastructural changes [64]. But it is very time-consuming and has numerous common artifacts.

Electron Tomography uses thicker sections ($200-1000nm$) and images the section several hundres of times. By this approach a z-resolution of $5nm$ can be obtained by software reconstruction; the resolution is then limited by the tilt interval [11]. The posibility of reducing the required number of tilts while conserving the z-resolution has been investigated [6].
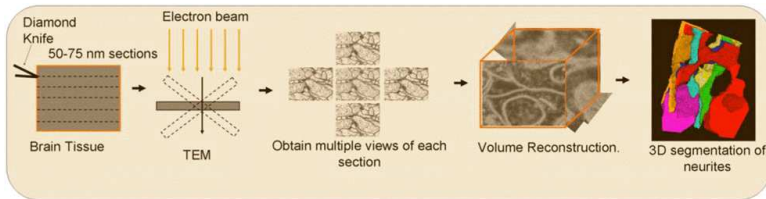
Figure 2.4: The principle used for 3D reconstruction of TEM sections by multiple imaging of single section. Figure from [6].

Instead of investigating serial thin sections with a high energy electron beam in TEM, one may prepare bulk surfaces and image the face with SEM. This overcomes many of the limitations of the labor-intensive ssTEM approach. It may also overcome the $z-limitation$ imposed by imaging a volume with TEM (slice thickness $50-75nm$) when tracing processes $< 50nm$ thick [3, 6]. The use of low electron energies (typically $1-3kV$) limits the depth of the signal to the upper tens of nanometers of the sample. The benefits of using low beam energies was proposed even before the commercialiation of the instrument [20].

Automatic Tape-collecting Lathe Ultramicrotome

The Automated Tape-collecting Ultramicrotome (ATLUM) collects ultramicrotomed slices in a conveyor belt fashion by an adhesive tape. This removes the error prone procedure of manual collection (e.g. folding, wrapping and loss of sections). It also allows thinner sections ($25-30nm$ [6]).
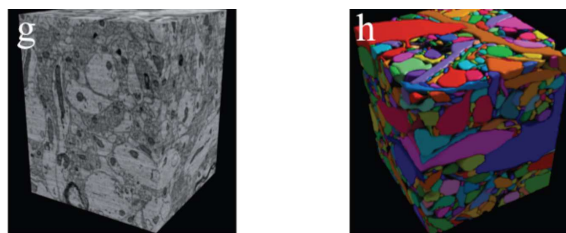

Figure 2.5: (g): reconstructed volume obtained through SEM. (h): segmented volume. Figure from [82].

The tape renders the sections relatively thick, resulting in the sections having to be imaged with SEM [10, 71]. This approach may be used to reconstruct large volumes with high resolution (comparable to TEM [77]). A volume of $40.960\mu m^3$ with a resolution of $2nm$ have been obtained using this technique [72]. Sectioning and mounting for resulting data reliability has been a concern for ssTEM and ATLUM [10].

SBF/SEM

In Serial Block Face SEM (SBF/SEM), an ultramicrotome is placed within the SEM vacuum chamber. An alternating process by first obtaining a SEM micrograph and thereafter sectioning the block by a diamond knife, is used to create a nearly aligned stack of images. This may achieve a $z - resolution$ of $25 - 30nm$ [6, 23, 41]. A z-resolution of $50nm$
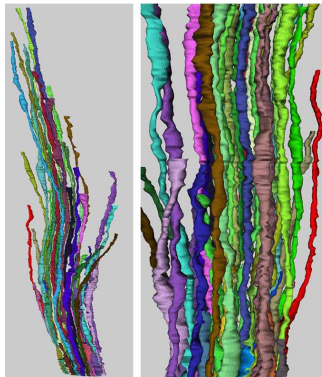
Figure 2.6: 500 secions imaged through SBFSEM used in reconstrucing axons. Figure from [27].

with a resolution sufficient to track the thinnest axons has been obtained [102]. Limitations of the technique include hardening of the resign by the electorn beam, that the volume is limited by the size of the diamond knife, one is not able to re-examine sections, that post-embedding immunolabeling is impossible, and artifacts arising from the physical cutting by the knife [71, 72]. The volume limitation of this technique is $6 \times 10^6 \mu m$.

FIB/SEM

The Focused Ion Beam/Scanning Electron Microscope (FIB/SEM) approach uses a focused ion beam for the sequential milling of sections and imaging the exposed block face. With this approach a $z-resolution$ of $5nm$ is obtainable [6, 33]. Using positively charged Ga^+ ions decreases agglomerated charging by the SEM, but the focused ion beam and verical sputtering of material introduces new aritfacts. The resolution is comparable to TEM, and isotroptic voxels of brain tissue for the 3D reconstructions is possible [35]. Limitations of the technique is similar to SBF/SEM, but the material removal is more sensitive (hardening of the resign is of no concern [34]), and the volumes are smaller (generally limitied to $10.000\mu m^3$ [35]).

Figure 2.7: A: the principle of the DualBeam instrument, the vertical line being the FIB the other the electron beam. B: a perspective SEM ciew of a processed volume. C: a high resolution SEM of the exposed surface. Figure from [102].

Using FIB/SEM may yield a very high resolution, but the volume under investigation is limited (surface area $0.5mm^2$), and the milling is time consuming [41]. Therefore, methods to map the regions of interest (ROIs) before initiating an experiment has been developed. This includes e.g. correlative approaches with Confocal Laser Scanning Microscopy ([92]), and *in vivo* 2 Photon Laser Scanning Microscopy ([35]). In these approaches the regions are selected with the first technique, and thereafter reconstructed with FIB/SEM. An optional approach for preliminary mapping might be using Energy Dispersive X-ray Spectroscopy (EDX).

EDX

The main limitation of volume EM today is the pixel density and scan time during SEM collection, and ways to create preliminary maps to locate ROIs is therefore of importance [41]. EDX and elemental mapping is a valuable asset as it frees the investigator from the operator bias as to where elements are located[32]. By specific elemental labeling, selected entities can be found by their characteristic X-rays. EDX has been used in Neuroscience e.g. for the investigation of iron-melanin interaction in parkinsonian brains ([51]), titanium nanoparticle agglomeration ([5]) and physiological agining due to Vitamin E deficiency[13]. These studies show that trace elements are found by use of their characterisitc wavelengths in brain tissue.

FIB/SEM has been used for elemental 3D reconstruction in a sample (anode microstructure quantification and reconstruction [46]), 3D elemental characterzation of the ceramic $CaMg(TiO_x)$ has also been done, a sample which -like biological samples- is insulating. A correlative approach may use SE images to correct for artifacts, and EDX can find defects 'buried' within the bulk [76]. In general, for site-spesific studies of microstructure, knowledge about where to locate the ROI in a sample can be very valuable [3].
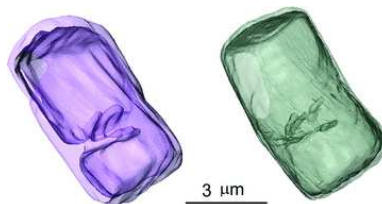
Figure 2.8: A: 3D reconstruction based on EDX images. B: 3D reconstruction based on SEM micrographs. Figure from [57].

3D rendering and elemental imaging of cellular features at the nanometre scale has also been demonstrated [57]. But such a resolution has to be obtained by a correlative approach, as the increased penetration depth of the X-ray signal in the interaction volume simulataneously decreases the resolution to a micrometer scale [32, 57, 65].

Chapter 3

Theory

This section presents the physics of the Scanning Electron Microscope (SEM), how it inluences the obtained signals, and the processing of them. The Foused Ion Beam (FIB) Microscope is then presented with the similarities and differences. The section ends with a presentation of EDX signals and staining of brain tissue. The combination of FIB and SEM in a Dualbeam instrument is presented in the materials and methods section.

3.1   SEM

The Scanning Electron Microscope (SEM) consists of an electron column commonly equipped with two or more electromagnetic lenses. The lenses are used to focuses the electron beam to a probe point on the specimen surface(**Fig. 3.1**). The lenses focus the beam with the force:

$$\mathbf{F} = q\mathbf{v} \times \mathbf{B} \tag{3.1}$$

The electron probe is scanned over the surface in a raster scan pattern. On each pixel, the electron beam pauses a set time (dwell time) to collect the signal. The signals are used to generate a micrograph. The magnification is the ratio of the length of the raster scan to the
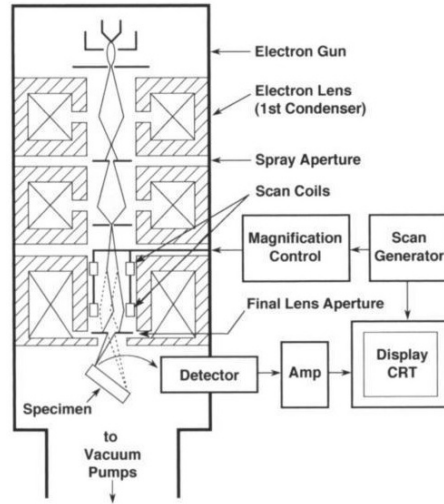
length on the viewing screen.

Figure 3.1: a schematic illustrating the electron column with important components of the instrument. Figure from [38]

Interaction volume

When the electron beam impacts the sample surface, signals are generated in the *interaction volume* (**Fig. 3.3a**). The most commonly used SEM signals are secondary electrons (SEs), backscattered electrons (BSEs) and X-rays. Different signals originate from different parts of the interaction volume revelaing different information of the sample.

The dimensions of the interaction volume can estimated by the equation:

$$R(\mu m) = \frac{0.0276A}{Z^{0.89}\rho}E_0^{1.67} \tag{3.2}$$

Where A is the atomic weight ($g/mole$), Z is the atomic number, ρ is the density (g/cm^3) and E_0 the beam energy (keV) [38]. The equation shows the importance of how e.g. material composition and beam energy influences the interaction volume. Increasing the acceleration voltage increses the dimension. The dimensions can also be estimated through Monte Carlo Simulations. The results of the estimations can be used for determining

e.g. the section thickness in ssTEM, SBF/SEM or FIB/SEM without losing information [40, 43, 47, 81].
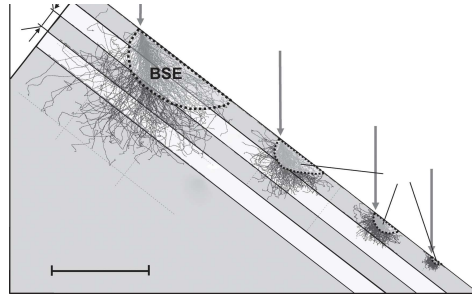

Figure 3.2: The figure shows a Monte Carlo simulation of the BSE signal depth as a function of acceleration voltage. Figure from [47].

The electron *beam energy* is defined by the acceleration voltage and the current density. This energy will determine the amount of signal produced. A charged particle of charge q accelerated by a voltage difference ΔV, will gain the speed:

$$v = \sqrt{\frac{2q\Delta V}{m}} \tag{3.3}$$

This speed will determine the penetration depth of the charged particle. Also seen in the equation is how increasing the current and the acceleration volume influences the focus of the electron probe.

For the generation of a signal, enough energy must be acquired in the interations with the incoming beam for the electrons to overcome the workfunction of the vacuum chamber [29]. The signal may reflect inherent properties of the sample e.g. composition. Higher atomic number elements will produce more BSE signal, called the atomic number contrast. This composition will appear brighter in the SEM micrograph [54]. The atomic/compositional contrast vairies as Z^2 [38].

As the electrons penetrate the sample, different scattering mechanisms lead to energy being lost and the ejection of secondary electrons (SE). λ (**Fig. 3.4a**) is the mean free path of the SE, which will depend on the material investigated. (Metals: $\lambda = 1nm$, insulators:
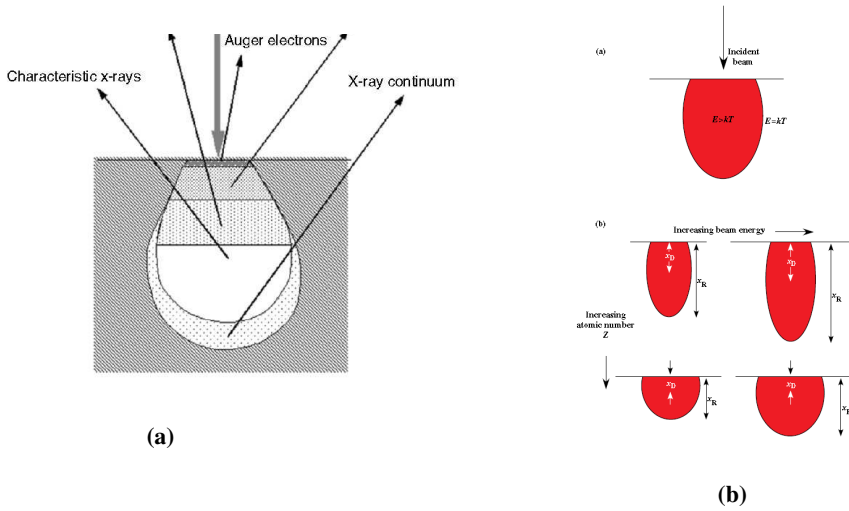
Figure 3.3: (a): Schematic of the interaction volume illustrating the distinct shape and relative positions of different signals. Figure from [99]. (b): The beam energy in combination with the sample determines the depth of the signal. Figure from [19].

$\lambda = 10nm$ [38]). Since the secondary electrons are confined to the top nm of the sample surface, this leads to highly resolved micrographs. But the resolution is decreased due to the generation of SE_2. Using a lower acceleration voltage reduces the interaction volume and increases the secondary electron yield (**Fig. 3.4b**).
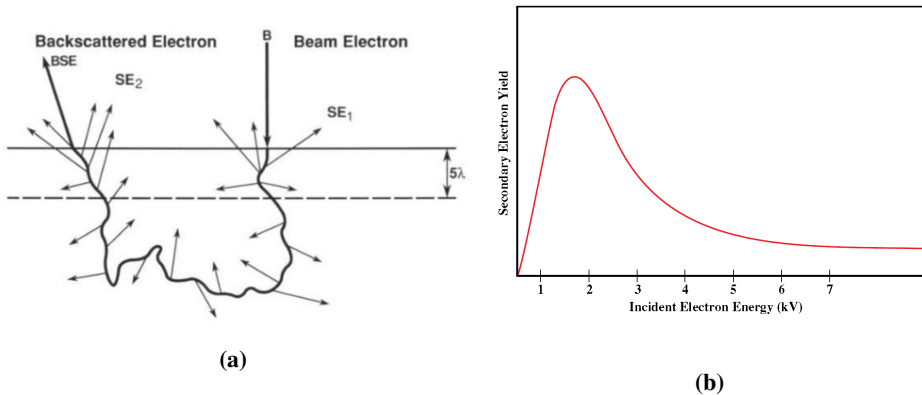
Figure 3.4: a: a primary electron from the beam propagates through a sample generating SE_1 and SE_2 before exiting as a BSE. Figure from [38]. b: how the secondary electron yield vaies as a function of acceleration voltage. Figure from [29].

Resolution

The concept of resolution is important as this may be used to define the information content of each micrograph, the required spatial separation to distinguish two objects[99]. When obtaining a signal from a point source in optical microscopy, the *Abbe equation* defines the spatial distribution of the intensity from that point:

$$\delta = 0.61 \frac{\lambda}{\mu sin\alpha} \tag{3.4}$$

In **Eq. 3.4** δ is the width of the primary peak, λ is the wavelength of the light used, μ is the refractive index of the medium between the lens and the focal point and α is the aperture (half angle) of the lens (**Fig. 3.5a**). Extrapolating to diffraction limited electron microscopy ([19]), the lens, vacuum and wavelength expressed in terms of acceleration voltage yield the a similar expression. The spatial intensity distribution is then defined by:

$$\delta_{diffraction} = \frac{0.75}{\alpha\sqrt{V}(1 + 10^{-6}V)} \tag{3.5}$$

The obtainable resolution of the instrument is then defined by the parameters of the electron beam and lenses used which yield the probe size, and further on the pixel size used (length separating the pixel dwell points). To be able to resolve two pixels, the signal from the two points must fulfill the Rayleigh criterion. This implies the angular displacement of the maximum intensity of one pixel is at the minimum of the next (**Fig. 3.5b**).

The resolution is determined by interactions at the beam impact point [73]. Increasing the acceleration voltage and decreasing the current decreases the probe size, but increases the interaction volume; decreasing the voltage decreases the dimensions but also increases the probe size and decreases the signal. At $30kV$ a probe size below $1nm$ can be obtained, at $1kV$ a size of a few nm and limiting the BSE signal to the upper tens of nm [44, 74].

For electron microscopy, in addition to diffraction, the abbe condition is influenced by spherical and chromatic aberrations from the lenses. Diffraction and chromatic aberration have the strongest influence, and have an inverse dependence on the angular aperture ($\delta_s =$

$C_s\alpha^3$), such that an optimum exists. Thus the width may often be expressed as: $\delta^2_{total} = \delta^2_d + \delta^2_d$ [19]. This defines the maximum resolution of the electron microscope.

(a)

(b)
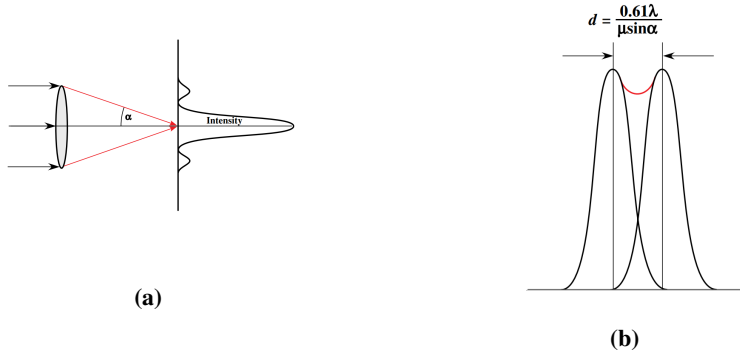
Figure 3.5: (a): The width of the intensity of the signal obtained from a primary point. (b): An illustration of the extent to which the width of the signal from two sources must differ for the pixels to be resolved. Figures from [19].

Specimen tilt and depth of field

When investigating a tilted specimen, the tilt angle leads to the dimension of the interaction volume increasing in the 'downwind direction' [38]. The cone/pear shape of the volume is maintained, but the angle introduces asymmetry in the investigated parts. The principle is shown in **Fig. 3.6**. The effect is also seen in **Fig. 3.2**.

Figure 3.6: The principle for the decrease in penetration depth as a function of sample tilt, the cone symolizing the interaction volume. The same asymmetry is seen in **Fig. 3.2**. Figure from [38].

Tilting of a plane specimen surface also results in an effect known as 'foreshorting'. Fore-

shorting implies that different areas are magnified differently as caused by their position. For a plane surface, the length from the sample to the electron lens (working distance) is equal irrelevant of the position in the ra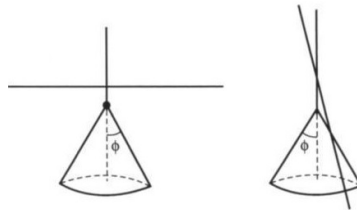ster scan. By tilting the plane surface, the 'top view' length of the specimen is no longer equal to the preceedig situation; the magnification perpendicular to the tilt axis will be lower relative the magnification parallel to the tilt axis. The principle is shown in **Fig. 3.7a** [38].

Depth of field is the height of features relative to a specimen surface in which the features are in optimum focus. If the electron beam is focused on a plane surface, all the features on the surface will be in focus. With increasing distance above and below this surface, the electron beam will diverge. This results in under- and overfocus of the beam at the respective locations.

At a certain distance the beam will have broadened -and thus the focus altered- to such an extent that the feature may appear diffuse. One may estimate the depth of field by using a geometric approximation shown in **Fig. 3.7b**. This leads to the equation:

$$\tan \alpha = r/(D/2) \tag{3.6}$$

$$D = 2r/\tan \alpha \tag{3.7}$$

where α is the beam divergence/convergence angle, D is the depth of field, and r is the radius of the semi-cone [38].
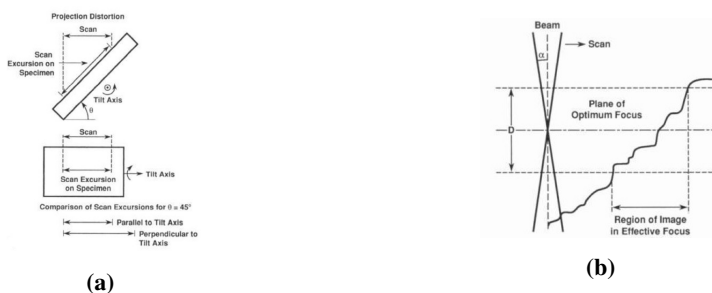

(a)

(b)

Figure 3.7: (a) The principle of foreshorting; regions of a plane surface will have a different magnification as caused by the difference in distance to the lens for selected areas; (b): a schematic of the depth of field, the distance above and below a plane of optimum focus where the features in the micrograph will be of the highest sharpness. Figures from [38].

The convergence angle has a strong effect on the resolution. Large convergence angles yield increased resolution, but at a tradeoff with a greatly reduced depth of field. This means features outside the optimum focus quickly become blurred; those within are rendered sharper [86].

If all the features are within the DOF, the foreshorting and tilt angle still leads to a correction having to be made in the $y - direction$ (perpendicular to the tilt axis **Fig. 3.7a**). By a trigonometric consideration, if the sample is tilted with an angle α, the resulting micrograph has to be elongated in the dimension perpendicular to the scan direction with a factor of $sin(\alpha)$ (**Sec. 4.3.1**).

Fourier Transform

The quality of SEM micrograph may be measured through its sharpness. This may be conducted through a Fourier Transform of the SEM signal. The SEM signal contains information about both the primary electron beam and the geometric features of the sample, but a SEM micrograph cannot separate dem. A Fourier Transorm of the image is applicable for such a separation, and be used to quantify them [75].

By transforming the spatial signal to its corresponding frequency, one may use where the integral converges as a measure of the image sharpness. Large scale geometric features are transformed to low frequencies, and finer details to higher frequencies. Thus higher frequencies implies finer features, a larger integral, a higher micrograph sharpness, and therefore a higher resolution.

The Fourier transform and its inverse is given in **Eq. 3.9** [63].

$$\hat{f}(\omega) = \frac{1}{\sqrt{2\pi}} \int\limits_{-\infty}^{\infty} f(x)e^{-i\omega x}dx \tag{3.8}$$

$$f(x) = \frac{1}{\sqrt{2\pi}} \int\limits_{-\infty}^{\infty} \hat{f}(\omega)e^{i\omega x}d\omega \tag{3.9}$$

It is possible to extend Fourier analysis from converting functions to converting discrete points from a dataset; such discrete Fourier transform (DFT) deals with sampled values (complex polymomal interpolarization). The Fast Fourier Transform (FFT) is an efficient implementation of the DFT. DFT is the most widely used discrete transform in digital signal processing [62].

The Fourier transform can be extended to two variables, e.g. x and y. The magnitude distribution of the Fourier transform may be used as a measurement scale, and is given [75]:

$$F(k,l) = \sum_{i=0}^{N-1} \sum_{i=0}^{N-1} f(i,j) e^{-i2\pi\left(\frac{k_i}{N} + \frac{k_j}{N}\right)} \tag{3.10}$$

$$f(a,b) = \frac{1}{N^2} \sum_{k=0}^{N-1} \sum_{k=0}^{N-1} F(k,l) e^{i2\pi\left(\frac{k_a}{N} + \frac{k_b}{N}\right)} \tag{3.11}$$

The magnitude of the transform reveals the geometric structures, the phase determines where in the image the frequency component originated. After having Fourier transformed an image both the phase and the magnitude must be conserved for the image to be identical in the image domain.

Image software processing (e.g. MATLAB [91]) may be used for the calculations. The transform may also be used to check the focus and astigmatism of the probe [75].
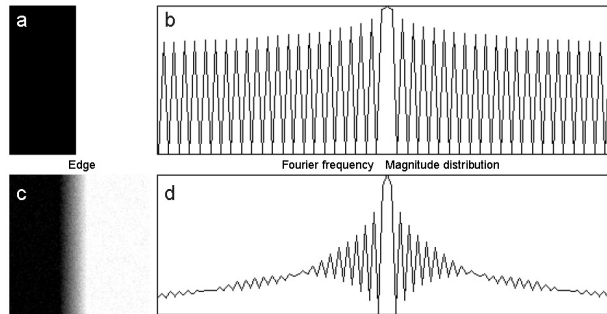

Figure 3.8: A simulated image of a sharp 1-dimensional edge (black/white) and its Fourier transform. The rapid shift gives a large amount of high frequencies relative a more diffuse change (underneath) [75]. The clear cut edge generates more high frequensies in the approximation.

3.2 FIB

The Foucused Ion Beam (FIB) microscope uses a beam of positively charged ions of high atomic mass (commonly Ga^+) and the interactions occuring at the sample surface -despite important differences- in a simiar manner as the SEM. Like the SEM, the FIB also operates by raster scanning the focused beam across the surface of the sample [67].

A common choice of ion source, is a liquid-metal Ga^+ ion source, as caused by its low melting temperature, the weight being adequate for the milling of heavier elements, its low volatility, low vapor pressure, and that the ions are easily distinguishable [105]. The liquid Ga^+ reservoir is in contact and wets a sharp tungsten tip, and a high excitation field $(> 10^8)$ is used to pull out the ions to a cone with radius $5 - 10nm$. Ions are emitted by field ionization and post-ionization, and accelerated down the FIB column [67].
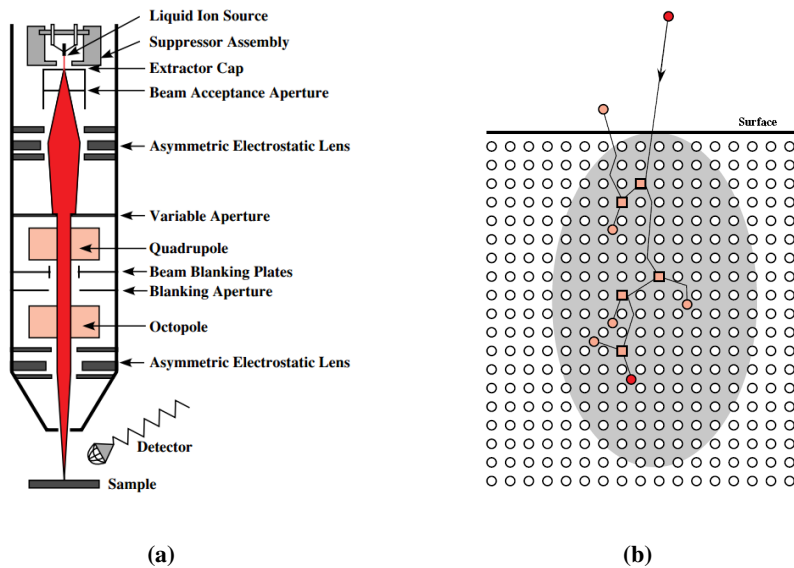

Figure 3.9: (a): the FIB column with the important components. (b): the sptial distribution of the damage of the impinging ions. Figures from [19].

As the ions are of high atomic mass (relative electrons), electrostatic lenses are used to focus the beam with the force: $F = qE$. A Scanning Ion Micrograph (SIM) may be

generated analogous to a SEM. The charged ions generates higher contrast, but also has a much more damaging effect on the sample surface.

Ion interactions

Elastic interactions results in momentum transfer from the energetic ions to the atoms of the sample. This may result in the atoms being ejected in a sputtering process. The elastic collitions may result in secondary electrons, phonons, plasmons and X-rays. The collision cascade may also lead to ions being implanted [103].

According to a Newtonian model, an energetic ion will transfer the maximum kinetic energy:

$$\frac{E}{E_0} = \frac{4m_1 m_2}{(m_1 + m_2)^2} \tag{3.12}$$

To displace an atom a commonly accepted value is $25eV$; an ion striking the surface with $25kV$ may therefore displace 1000 atoms in a cascade [19]. Thus, the cascade will cause damage not limited to the probe point (**Fig. 3.9b**). The sputtering effect is therefore most often utilized in cutting and shaping samples rather than imaging them.

The overall quality of the FIB milling is material dependent, e.g. cross sections of FIB prepared TEM sections shows a broadening at the base, which widens with atomic number [89]. Little is known of FIB induced damage to polymer and soft materials other than qualitative evaluations. FIB/SEM interactions may change the chemical composition and bonding in soft materials, e.g. electron beam irradiation may increase the amount of aromatic carbon bonding in acrylamide [88].

Ion beam accuracy

The accuracy of the ion mill is important to control, as inconsitensies in the ion mill degrades the cutting/shaping. If the process is repeated e.g. to cut sequentially inwards in a volume, the deteriorations often propagate through the protocol.

The ion beam has a current profile with a focused core and a Gaussian current density distribution; the profile has long tails which decreases with distance [18, 61]. This beam profile limits the accuracy of the mill, and despite a number of advantages of low voltage focused ion beams, it is difficult to obtain submicron beams with conventional optics [61].

GIS

The Gas Injection System (GIS) may be used to deposit metal on the sample surface. The deposition may be used e.g. to decrease charging or topography on a sample surface, or soldering for e.g. a 'lift-out' procedure where a thin sample may be soldered to a collection probe and directly removed [89].

The principle is shown in **Fig. 3.10**. A precursor gas is introduced by a gas injection needle near $(100-200nm)$ the surface and adheres by van der Waals forces. Then the ion beam is used to decompose the precursor (*in situ* chemical vapor deposition) [15, 67, 105]. Volatile byproducts leave the surface and gets removed by the vacuum. The ion flux relative the precursor density determines the amount of sample sputtering relative metal deposition. The metal deposited is amorphous.

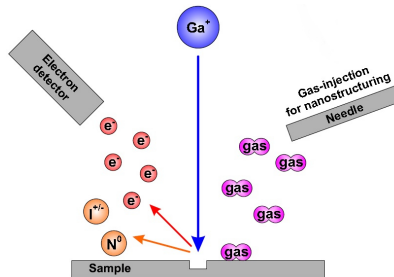**Figure 3.10:** A schematic showing the priciple of the gas injection system. A precursor gas is injected close to the surface and adheres to the sample. It is then dissociated by the ion beam, the precursor is removed and the metal is deposited.

3.3 EDX

The electron beam can be used to excite X-rays from the sample. X-rays are generated in the lower part of the interaction volume (**Fig. 3.3a**). The result from the excitation is an X-ray Spectrum. The photons may contribute to the continiuum background (Bremsstrahlung), or be spesific for the element from which it originated as characteristic X-rays.

The earliest theoretical model of the braking radiation in the X-ray spectra (Kulenkampff and Kramers):

$$EN(E)dE = CZ(T - E)dE \tag{3.13}$$

where E is the energy of the X-ray photon produced, $N(E)dE$ the number of photons produced per incident electron having an energy between E and $E + dE$, C is a constant, Z the target atomic number and T is the electron kinetic energy [24]. This equation - despite its derivation including several simplifications- shows the dependency of the X-ray count rate on the electron beam energy, and the importance of the atomic number.
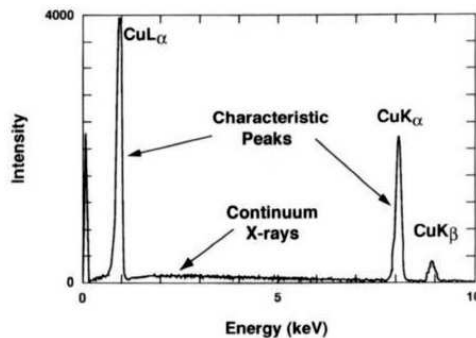

Figure 3.11: A schematic of an X-ray spectrum with the braking radiation and the characteristic X-rays indicated. Figure from [38].

Braking radiation (Bremsstrahlung)

The X-ray continuum results from deceleration in the positive field of the nucleus of the atoms in the sample. The electrons in the positive field may loose the energy ΔE. This loss in energy is emitted as a photon with an energy $\Delta E = h\nu$, where h is Planck's constant and ν the frequency of the electromagnetic radiation. Since the deceleration events are random, the electrons may loose energy ranging through the whole energy spectrum, from 0 to the incident energy E_0. This creates a continuum of the braking effect the positive fields have on the incoming electrons, hence the name [38].
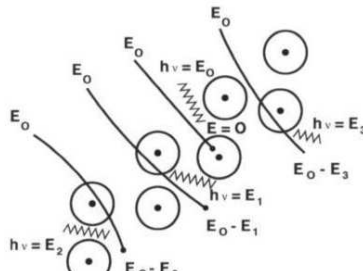
Figure 3.12: A schematic showing the origin of the braking radiation. The random deceleration of the incoming electrons in the Colombic field of the atoms in the sample cause the excitation of an entire X-ray spectrum. Figure from [38].

Characterisitc X-rays

An excited atom will deexcite through a limited series of allowed steps. Excess energy is released by ejecting an electron with a spesific kinetic energy (an Auger electron), or releasing X-ray wavelengths [38]. Even though the X-ray spectrum contain all of the wavelengths, certain wavelengths (corresponding to characteristic energy shell differences of the elements present) rise far above the background radiation in the number of counts. These profiles in the wavespectrum are characteteristic for elements in the sample, and may be used to identity the element of origin [54]. Characteristic X-rays stems from the excitation of an inner shell electron exiting the atom, as shown in **Fig. 3.13a**.

EDX analysis may be used in constructing *dot maps*. Such maps are constructed by label-

Figure 3.13: (a): The excitation/de-excitation process generating an Auger electron or a character-istic X-ray. Figure from [19]. (b): The energy band separations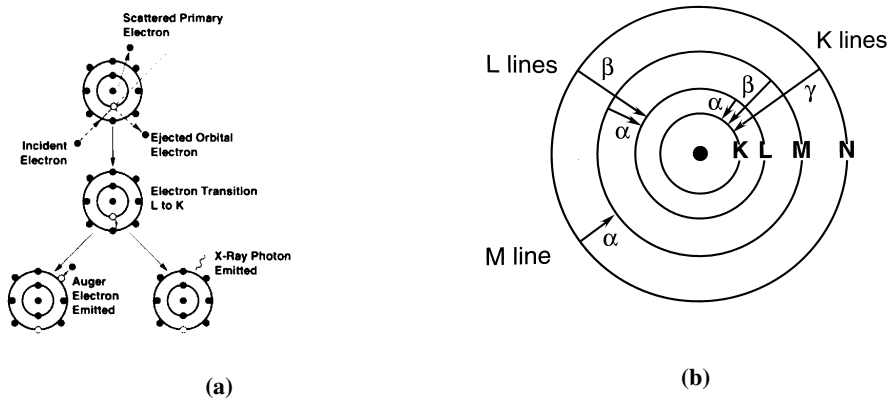 are characteristic for each element, and therefore also the X-ray energies resulting from the de-excitation of the respective element. Figure from [54].

ing specific peak wavelengths before the raster, and if a characteristic X-ray is collected a bright dot appears in the micrograph. Pseudocoloring of the different elements can be used to create elemental maps of the surface investigated. By superimposing the elemen-tal map on a SE image of the surface, the elemental distribution of the specimen may be determined [54]. The number of counst per pixel required for a stistically significant map is regarded as 8, thus leading to 130.000 cunts for a 128×128 image [32].

Despite the possibility to conduct EDX on bulk specimen, irregular surfaces restrict quan-titative analyses. The large interaction volume restricts the resolution to around $4 - 8\mu m$ [32, 54]. The dimensions of this volume may be calculated through **Eq. 3.2**, substituting E_0 with ΔE with respect to the critical excitation energy [79]. The dot maps may be used to construct 3D elemental distributions of samples under investigation [46, 103].

3.4   Staining and sample fixation of brain tissue

Electron microscopy needs to be conducted in a vacuum due to the mean free path of electrons being highly sensitive the the presence of gas molecules. But since biological tissue is composed of high amounts of water (which boils at vacuum), special sample preparation has to be conducted for the samples to be investgated. The samples need to be both dehydrated and fixed, but in a way that best conserves the structure of the material [101]. Stabilizing thin sections with crosslinking fixatives is the common approach for EM investigations [104].

Another aspect of sample preparation is avoidance of the artifact of charging. Biological tissue is insulating, such that investgated surfaces of the tissue would quickly charge if steps are not taken to decrease this artifact. A charged surface investigated by SEM will lead to the electron probe not being able to adequately follow the predefined raster. For the investigations of surface topography of a fixed biological sample, a metal coating is sufficient for the avoidance of charging [29]. But for investigating internal structures, the samples has to be stained. This may be done by conductive metal staining, but this again leads to every investigation of biological tissue by electron microscopy is indirect. Every step taken to increase the conductivity, degrades the structures under investigation. And the ultrastructure of brain tissue is very sensitive to the use of fixation chemicals.

The following procedures relate to the use of fixative chemicals developed for TEM. A comparison og conventional drying of the samples for SEM or plastic embedding as for TEM has shown that for topographical investigations the samples should be dried, whereas when investigating cell ultrastructure plastic embedding proves superior [96]. The procedure was later extended for the fixatives to be used in *en block* sample preparations. This means staining of tissue in bulk, which is further sensitive to the diffusion rate of the chemicals involved [101].

The most common chemical fixative is the use of aldehydes [53]. Aldehydes fix and preserves fine structural details in tissue by inducing crosslinks between proteins; having directly crosslinked proteins, other biological tissue becomes indirectly fixed, enclosed in
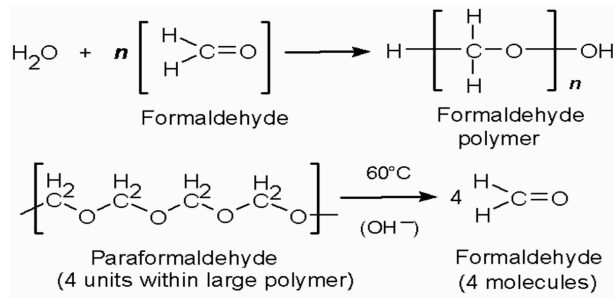
Figure 3.14: Top: formaldehyde dissoved in water forms methylene hydrate and polymerizes. Bottom: higher order polymers requiring energetic depolymerization. Figure from [53].

the fixed protein structure. Glutaraldehyde is usually the aldehyde of choice for fixation, but formaldehyde for en block staining is also used [68]. Formaldehyde has a lower modelcular weight, and may therefore be used for an increased speed and penetration depth of the fixative. But, the lower molecular weight also decreases the number of crosslinks induced by the molecule. Formaldehyde is a gas, and paraformaldehyde is higher polymers of formaldehyde (stable, white powder), and needs to be depolymerized to be used as a fixative [53]. The combination of glutaraldehyde, paraformaldehyde and phosphate buffer is commonly used for fxation of brain tissue [4, 33, 34, 35, 42, 70, 72, 84, 92, 93, 102].

The use of Osmium tetroxide (OsO_4) was used before the introduction of aldehyde staining, but is now used mostly for post-staining protocols, and is a necessity for further dehydration and plastic embedding. The use of Osmium increases the BSE signal due to its relatively high atomic number [68]. A combination of Osium tetroxide and Potassium ferrocianide ($K_4Fe(CN)_6$) may also be used for postfixation and staining. Potassium ferrocianide increases the reactivity of Osmium tetroxide and enhances the reactivity of Osmium.

The procedures discussed were developed for TEM. For investigations of samples in SEM (therefore FIB/SEM), the samples need to be able to sustain sectioning required for the exposure of selected surfaces. This may be done through embedding the tissue in an epoxy resign. Epoxies are thermosetting polymersic resings, and the epoxide chemical group crosslink at increased temperatures in the presence of a hardener. For sample preparation
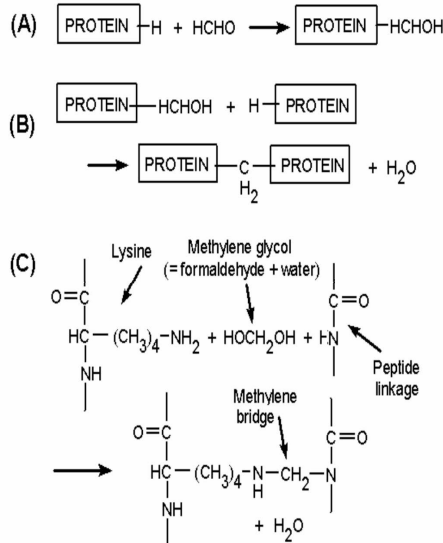
Figure 3.15: The protein crosslinking mechanism by the induced methylene bridge, often between the nitrogen atom from the lysine side chain and the nitrogen of a peptide linkage. Figure from [53].

procedures, water is exchanged with a solvent (ethanol or acetone), and the solvent is later substituted with epoxy. The sample is then cured at elevated temperatures, and remains stable for years.

To increase the contrast of the staining, heavy metal salts are often used; the salt most commonly used is uranyl acetate (salt of uranium). Staining with using uranyl acetate may lead to crystallization, and is often a consequence of prior chemical treatment of the tissue. In particular, if long osmium treatment have been conducted, uranyl acetate staining is reduced, and the saturated solution may lead to the agglomeration of uranyl acetate. The appearance of elongate characteristic crystals of uranyl acetate (**Fig. 3.16**) should lead to the uranyl acetate staining step being considered [25]. Such crystals make sectioning difficult. Uranyl is photo reductive and will precipitate is not carried out in the dark. Uranyl acetate staining can be done pre- or post-embedding, and is a positive stain leading to the labeled entities having an increased electron density of the structures
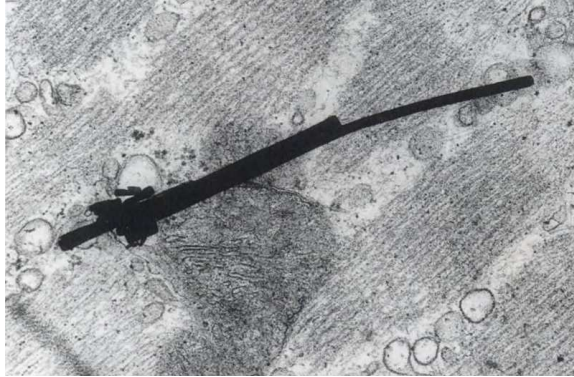
increasing the contrast.

Figure 3.16: A needle like Uranium crystal formed during the staining of muscle tissue for TEM. Figure from [25].

For brain tisse to be investigated, the brain of the animal need to be fixed by perfusion. Cardiac perfusion utilizes the heart and circulatory system of the animal to pump the fixative into the brain. To increase the penetrative speed of the fixative and conserve the ultrastructure of the brain as close to the original as possible, the purest formaldehyde is utilized by depolymerizing paraformaldehyde by heat treatment.

A common way of labeling biological entities is the use of the avidin biotin immunohistochemical approach. Avidin has very strong affinity for biotin, and avidin has multiple binding sites for biotin and is commonly used in an avidin-biotin-peroxidase complex. If brain tissue has been labeled with biotinylated dextran amine (BDA), the complex will presist only in the positions where biotin is present. Furthermore, these reagions can be visalized by reactions with 3,3-diaminobenzidine (DAB). DAB reacts with peroxidase and generates an osmophilic precipitate (DABppt), which again reduces OsO_4 to the electron-dense osmium black, easily distinguishable in SEM micrographs. The final reaction can be seen in

$$DAB + H_2O_2 + peroxidase \rightarrow DABppt + 2H_2O \qquad (3.14)$$

Gold intensification

The DAB reaction product may be intensified by double labeling, by use of a silver developer and gold toning [84]. Horeseradish peroxidase (HRP) is not inherently electron dense, but the reaction primary end product is *argyrophilic* meaning that it catalyzes the reduction of dissolved silver to submicron metallic silver grains [54]. The deposited grain are autocatalytic, and the silver grains may grow to a microscopic level, and increase the visibility of the DAB stained entities [29]. Thus, a silver developer (containing $AgNO_3$) may be used for deposition of silver on the DAB stained end product [106].

(a)

(b)
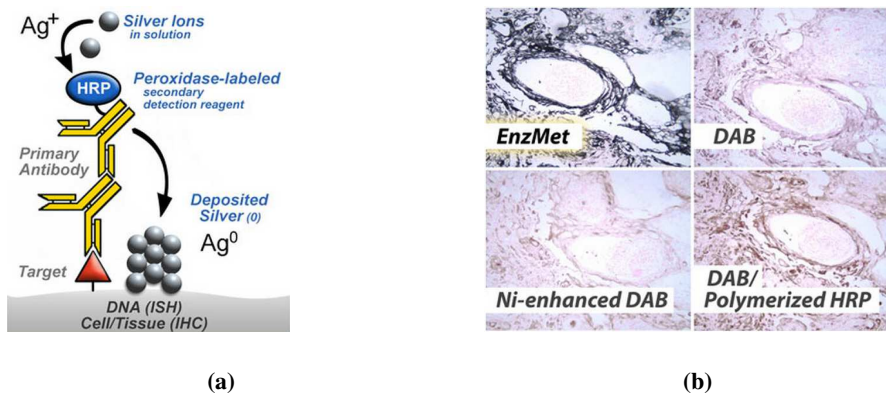
Figure 3.17: (a): the reducing environment caused by the DAB reaction product catalyzes the deposition of silver. (b): a comparison of the silver enhacement with conventional staining. Figures from [1].

A subsequent gold toning procedure substitutes gold with the precipitated silver. Gold is more chemically inert than silver. There exists different protocols, and an option to decrease the false-negative results is by converting the precipitated deposited silver from amorphous to granual [29]. Gold toning provides higher benefits in EM investigations than silver enhancement, as it further increases contrast and greatly increases the BSE signal [36].

---

[1]http://www.nanoprobes.com/products/EnzMet-SISH-enzyme-\
metallography-for-ISH-and-IHC.html

Chapter 4

Materials and Methods

This section introduces the instrument, samples and procedures used in the investigations conducted for this Thesis. All brain tissue samples were prepared by Ph.D candidate Jøregen Sugar. The structure is as follows: an introduction to the Dualbeam FIB/SEM instrument, its setup and applications; a presentation of the samples and their preparation protocols; the software used in the dataprocessing; then the experiments are presented. The section finalizes with common artifacts normally encountered when using the FIB/SEM.

4.1 FIB/SEM Dualbeam instrument

In this Thesis a $FEI\ Helios\ NanoLab^{TM}\ DualBeam^{TM}\ FIB$ was used. The instrument has two optical columns, a vertical electron column and an ion column separated by $52°$ (shown schematically in **Fig. 5.27**) [29]. The instrument is equipped with detectors for Secondary electrons (SE), Bacscattered Electrons (BSE) and energy Dispersive X-rays (EDX), and different operation modes which are best suited for different magnifications/applications. This has been ivestigated previously by the candidate [91]. The two optical columns makes it possible to use the FIB 'nano-knife' to expose bulk areas

of the sample and investigate the exposed surface with SEM [47, 95]. Volumes may be investigated in a protocol called 'Slice and View'. In such a process, the sample remains stationary in the x, y dimensions, and only shifts in the z dimension (**fig. 4.11**).

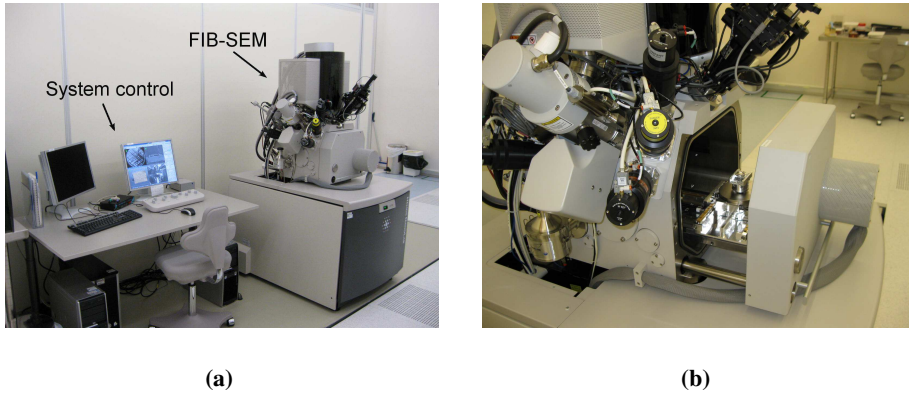(a)   (b)

Figure 4.1: Images of the Dualbeam instrument at NTNU Nanolab used in the investigations. (a):an image showing the system control and the instrument with the vertical electron column and the ion column separated by $52°$. (b): the vacuum chamber has been opened to insert a sample. Figures, courtesy of Ken Roger Ervik.

To reduce human intervention, automation software for the Slice and View procedure has been developed (e.g. FEI Slice and View G2). This increases section thickness consistency, and allows the procedure to be run unsupervised [14, 95]. For further decrease of irregular slice thickness, the ion beam may be used to collect a driftcorrection image between the slices . This Scanning Ion Micrograph (SIM) allows the comparison of the stage position between the ion millings, while the stage position is unaltered. This allows corrections to be done through comparisons with a reference fiducial mark (**Fig. 4.9**).

Imaging done through a 'Slice and View' may make the charging artifact less severe (**Fig. 4.21**). This is because the two charged paricles have opposite charge. Accumulated charge may influence both probe points and cause distortions in the data [95]. During the Slice and View, the working distance of the electron beam shifts. This leads to the focus having to be readjusted at certain intervals. The FIB and SEM parameters will dictate the time required for the process and the quality of the obtained images [65].

Instrument setup

The SEM sample stub (**Sec 4.1**) is fastened to the chuck in the vacuum chamber before pumping the chamber. Using the Everthart Thornley Detector the sample is located, rotated and aliged with the preprepared section cut for the area to investigate. The working distance (distance from the final lens aperture to the sample, **Fig. 3.1**) is set to $4.1mm$ (instrument standard). Then the sample stage height is adjusted to the eucentric height, being the height where the probe point on the sample is unaltered despite tilting the stage [86]. Then the coincidence point of the two beams is checked, that both beam aim at the same point. An ion 'Beam shift' is used for adjustments. The accuracy of the coincidence point should be within $5\mu m$ [86].

(a)   (b)
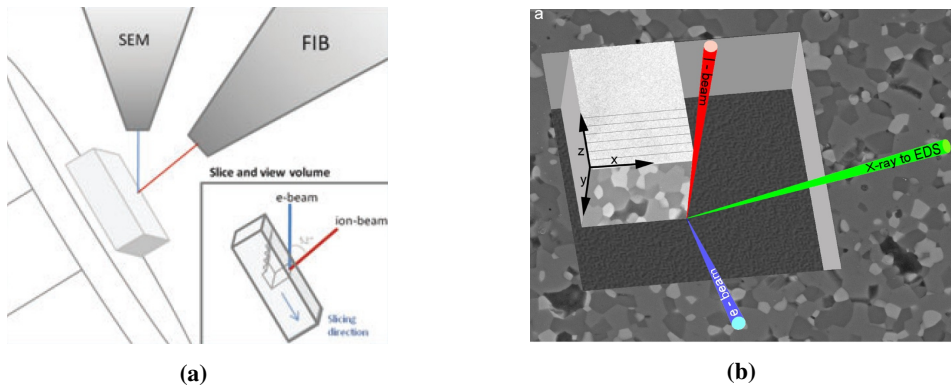
Figure 4.2: The figures shows potental applications with the FIB/SEM instrument. (a): a schematic illustrating the Dualbeam setup for use in a Slice and View. The alternating use of the ion and electron beam while the stage is stationary. Figure from [49]. (b): a schematic of an EDX investigation of a sample in the FIB vacuum chamber. What is seen is the relative orientations of the ion and electron beam, in addition to the direction of the EDX detector. This direction has to be taken into account if X-rays are to be collected. Figure from [76].

Sample Preparation FIB

The samples were fastened on an aluminium SEM sample stub by conductive carbon tabs and copper tape [70]. Epoxy glue may also be used. Then the stub was sputter coated with $40nm$ Au ([4, 35, 70, 92]) in a Sputter coater for SEM sample Preparation, Cressington

208 HR B. This reduces surface charge accumulation [14, 33, 35, 47, 92]. The metal coating also leads to a an efficient decrease in localized heating, which may be a cause for inaccurate ion milling [52, 88]. Carbon or Platinum coating is also applicable [14, 16, 28].

4.1.1 SEM Imaging

BSE collection by the TLD or 'in-lens' detector is a common choice in FIB/SEM investigations, and the use of $1 - 4kV$ voltage provdes an x-y resolution of $1.5 - 3nm$ [28]. A BSE signal at $3kV$ originates from about $15nm$, and the SE singnal from $\leq 1nm$. During previous investigations performed by the candidate, the imaging parameters providing the highest image sharpness at given magnifications were investigated [91]. For magnifications below $35.0000X$, the Through-the-Lens detector in the Field Free mode provided the highest degree of sharpness. In addition, for the same operation mode it was shown that despite the effect of Foreshorting (**Sec. 3.1**), the lens Depth of Field yielded the whole image in focus.

The imaging parameters used for collecting high quality SEM images of the brain tissue at magnifications of $8000X - 10.000X$ were; acceleration voltage: $2kV$, current: $0.17nA$, resolution: 2048×1768 and dwell time $100\mu s$ [34]. The detector collected SEs. Low voltage and current yields highly resolved images [35, 70]. Despite the time requirement for the collection of each SEM (the SEM aquisition speed being a practical limitation [102]), these parameters ensures adequate signal from a small interaction volume, resulting in high resolution micrographs as desribed in **Sec. 3.1**.

4.2 Samples

Five types of samples were investigated in this Thesis. For the trench milling, an ultramicrotomed empty Epon block was used. This ensured that the results could be generalized to brain tissue investigations. For the Slice and View to reconstruct brain tissue, specialized sections were prepared and embedded in Epon epoxy. Two embedding protocols were investigated, thin sections and re-embedded sections (**Fig. 5.8**). The EDX model used a basis of an empty Epon epoxy block. For the EDX investigations of brain tissue, a sample section was stained with DAB and double labeled though a silver/gold intensification process.

Tissue extraction and block preparation

To investigate biologcal tissue in the FIB/SEM the tissue must be dehydrated, stained and fixed [101]. A mouse model was used, the brain to be examined was extracted from the mouse following chemical fixation by cardiac perfusion with Phosphate Buffer Saline (PBS) and paraformaldehyde. (For details regarding the perfusion of rodents, see [39].) The brain was then sectioned and selected regions were washed with PBS and water. The antibody-DAB staining procedures for the tissue used in these experiments were all done in a cold room or on ice, over a period of 11 days; through cryoprotective agents (DMSO in PBS), primary- and secondary antibodies and Tris-HCl buffer.

The sections were then stained with Potassium ferrocyanide and Osmium tertroxide for $2h$, washed in PBS and dehydrated in a graded alcohol series [92]. Thereafter the sections were stained with Uranyl acetate in alcohol for $2h$ at $60°$, after which the tissue was infiltrated with Epon epoxy using solutions with Propylene oxide [4, 34, 35, 97]. The DAB labeling results in an interneuron morphology as visualized in **Fig. 2.3**.

The tissue was left in Epon over night. The final hardening was done by placing the the tissue in a $60°$ oven for 3 days. Further processing included removing the separating agents, cutting the tissue containing the region of interest (ROI) into smaller geometries.

This concludes the thin sample preparation, the re-embedded samples were mounted on an empty Epon blocks. The blocks were further trimmed with an ultramicrotome, resulting in adequate dimensions for the FIB [33].

EDX model

The model designed to investigate EDX for searching applications was created on an empty Epon epoxy block. The block had been ultramicrotomed to appropriate FIB dimensions, resulting in the block having clear cut perpendicular faces. The protocol stated in **Sec. 4.1** was followed for FIB preparation. Copper tape was used, and $40nm$ of Cr was sputter coated instead of Gold (significantly different characteristic X-ray wavelength [60]).
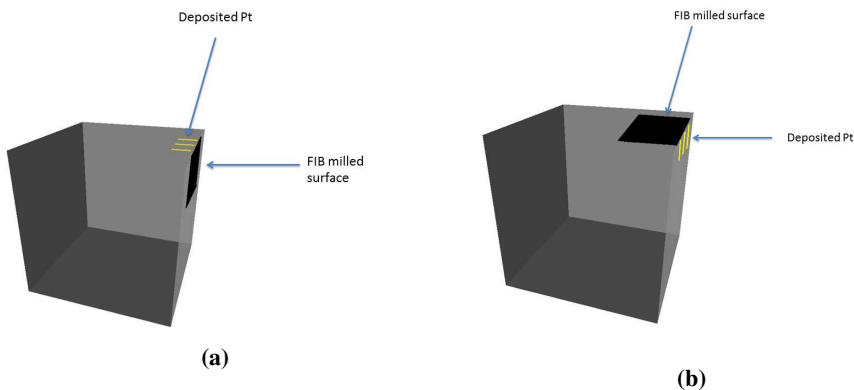

Figure 4.3: Figures illustration the relative orientations used when preparing the EDX model. (a) the block orientation required for the deposition of Pt by the GIS and FIB milling; (b) the sample reoriented to place the deposited Pt on the wall for the geometry to be investigated in the experiments (**Fig. 5.23**).

As a model for finding gold ($Z = 79$), platinum ($Z = 78$) was used due to very similar excitation and characteristic wavelengths [60]. Three layers of Pt was deposited through the GIS system (**Sec. 3.2**), with surface areas of $40\mu \times 5\mu m$, and thicknesses of $0.5\mu m$, $1\mu m$ and $2\mu m$. The layers were deposited with the ion currents $0.26nA$, $0.44nA$ and $0.9nA$, respectively. After deposited the three layers, the residue volume separating the

Pt layers and the edge of the block was milled ensuring a clean surface composed of only Epon epoxy(**Fig. 4.3a**).

After the Pt layer deposition, the block was removed from the SEM sample stub, reoriented, and adhered to a new SEM sample stub by the same protocol. The new orientation placed the deposited three Pt layers on the vertical wall of the block and the clean FIB milled surface on top (**Fig. 4.3b**). This made it possible to investigate how far the EDX results could be traced through empty Epon epoxy. A new layer of $40nm$ Cr was deposited to decrease charging.
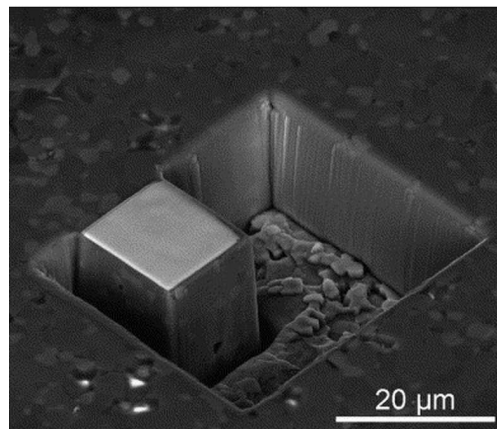
Figure 4.4: The geometry required for a FIB-EDX tomography experiment. This to ensure the adequate dimensions for the accurate FIB milling (redeposition) and efficient EDX detection. By placing the ROI at a sidewall (**Fig. 4.3b**) the same requirements are met. Figure from [76].

Gold intensified DAB stained tissue

The preparation protocol for the doubly labeled brain section is similar to the one stated in **Sec. 4.2** for the DAB labeling. After the DAB labeling protocol, the labeling was intensified with a silver solution, and further enhanced though gold substitution. But the staining was not contrast enhanced with uranyl acetate, and the hardening was reduced from 3 days to 1 day at $60°$.

4.3 Software processing

4.3.1 FIJI

Stack processing

For the processing of the stacks of images obtained through the Slice and View procedure, the open source program Fiji (Fiji.sc) was applied. This section gives the protocols followed when processing the raw data obtained from the Slice and View for the 3D reconstruction. A raw data example collected through a Slice and View is shown in **Fig. 4.5**.
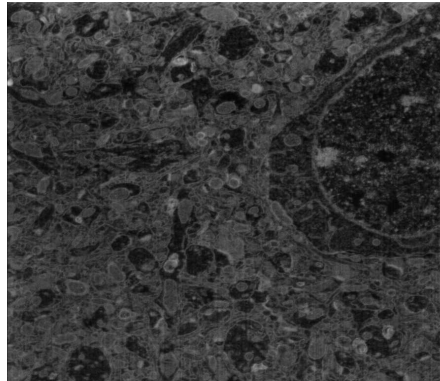
Figure 4.5: The figure shows a raw micrograph taken with the optimized SEM parameters (**Sec. 4.1.1**).

For image stacks to be used in 3D reconstructions, the sequential images were then aligned using the plugin 'StackReg'. As the stage remains stationary through the process and only shifts in the $z-direction$, alignment based on 'translation' was used. The residue surface area not conserved through the stack was thereafter cropped. The sequence of FFT processing and alignment must be considered, as it can be both beneficial and detrimental for the alignment. FFT processing can be used to subdue artifacts (e.g. not too prevalent curtains), but could also lead to misalignment.

If excessive curtaining (**Sec. 4.5**) or drift (**Sec. 4.5**) was present, the StackReg tool did not align the slices correct. Selected slices were then manually shifted (Image>Transform>Translate) to more accurately align in the sequence. Aligning the stack with different reference slices was also done. With these additional steps, the StackReg was used with success.

For realistic 3D rendering, the images must be corrected for the SEM angle. This is done by elongating the shortened dimension. The image is corrected for the tilt view of the SEM by elongating the $y - dimension$ by a factor of

$$sin(52) = 1.27 \qquad (4.1)$$

by a bicubic interpolarization. The trignometric foundation of the correction is shown in **Fig. 4.6**, the result in **Fig. 4.7a**.
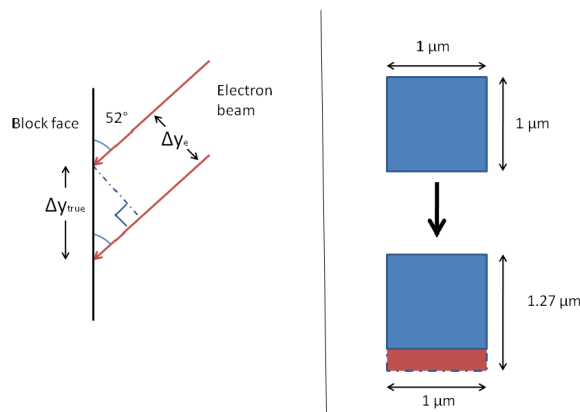
Figure 4.6: This figure illustrates how the geometry of the micrograph must be corrected for the SEM angle. Schematic, courtesy of Ken Roger Ervik.

Then the image is inverted for it to resemble a TEM and make tracing contours more convenient ([34]), shown in **Fig. 4.7b**. Further, the micrograph is process through a Fast Fourier Transform (FFT) Bandpass filter, filtering pixels frequencies up to 1 pixel and down to 100 pixels. The choice of saturating the pixels afterwards was chosen to increase the similarity of the images in the stack. The filter used also simulataneously suppressed vertical stripes (reduces curtaining), and horizontal stripes (sometimes resulting from the

$y-direction$ elongation). Finally the images were 5% contrast enhanced to further ease the tracing. The result is shown in **Fig. 4.7c**.

| (a) | (b) | (c) |

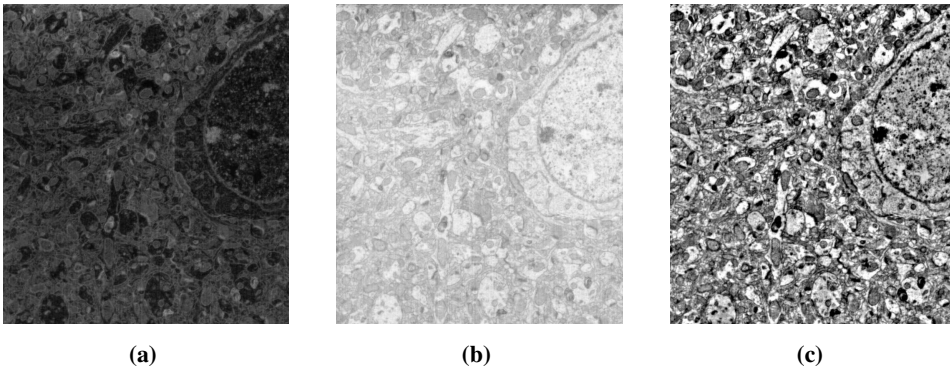**Figure 4.7:** The image processing is illustrated by the enhancement of **Fig. 4.5**. (a) bicubic interpolated raw data; (b) elongated image inverted; (c) micrograph processed through a FFT bandpass filter and contrast enhanced.

EDX image processing

FIJI was also used for processing EDX elemental maps. All the EDX images were inverted and contrast enhanced. For the superimposed preliminary EDX mapping experiment **Sec. 5.3.2**, some additional steps were taken. For clarity, the brightness of the SE micrograph was decreased. The elemental map was processed through contrast enhancement and reduced for the color channels of the two images to be merged. The superimposed pseudo-colored image shows the presence and distribution of the constituting elements [83].

4.3.2   Avizo Fire

After the FIJI processing, the image stack was imported into Avizo Fire 7.1^{TM}. First the voxel size is input, which is the x, y, z dimensions corrected for the number of pixels. Then the stack was filtered through a median filter. This was followed by the segmentation process. On **Fig. 4.8**, a cross section of an interneuron is labeled through the 'Magic Wand' tool. With this tool, one selects a pixel and sets thresholds threshold values and the

software tracks the propagating contour within the thresholds. In the figure the thresholds are set and the contours of the interneuron is tracked and labeled with red.
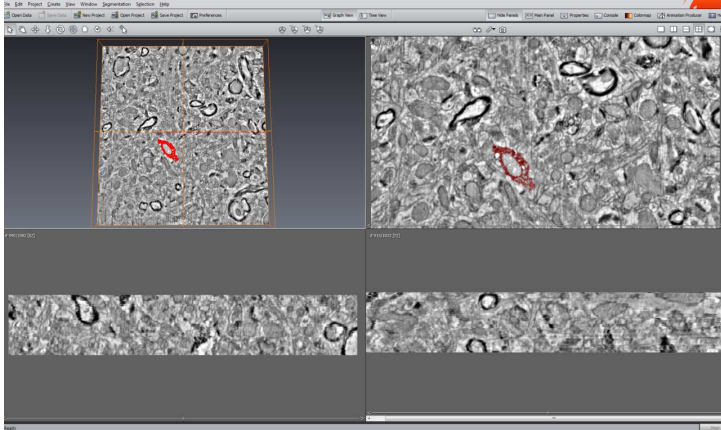

Figure 4.8: An example illustrating the labeling of a selected entity in a single slice. An interneuron crossection is here labeled red and tracked with the Magic Wand tool in avizo Fire 7.1.

This can be done for each slice, or the selected contour can be automatically traced through the volume. But due to artifacts and irregularities through the stack, this process often led to wrong labeling and was therefore not used for the interneurons. The interneurons labeled in the figures are labeled sequentially on each slice. The generalized tracing ability of the software was tested for the semi-automatic tracing of axons. After having performed the labeling, a surface view can be created. A smoothening step was included. To increase the accuracy of the labeling of e.g. axons running perpendicular to the plane of sectioning, the labeling can be done on the plane best suited.

4.3.3 MATLAB

An analysis of the micrograph sharpness was conducted thorugh MATLAB. In earlier investigations by the candidate ([91]) a MATLAB code was written which measures the micrograph sharpness based on a Fourier Transform of the image (**Sec. 3.1**). The code subdivides an image to a matrix of cells, all of which are Fourier Transformed and uses

the converging integral as a measure of the degree of clear cut boundaries. The quantified results from each cell are averaged as a generalized expression of the image sharpness.

4.4 Experiments

4.4.1 General procedure before imaging and $S\&V$ experiments

For high quality data in the Slice and View experiments, proper preparation needs to be doen in advance of the experiment. The samples were therefore inserted into the vacuum chamber at least $12h$ before the experiments to reduce image drift [16].

For the co-localization of the SEM and the FIB probe point, FIB parameters of $30kV$ and $26pA$ was used for both the focusing of the ion beam, and to ensure an accurate co-localization of the two probes. With the probe points colocalized, a rough milling of the sample was performed to expose possible ROIs. Rough milling was performed with ion currents of $6.5nA$ and $9nA$.

Above the ROI, conductive and protective layers of platinum and conductive carbon ($1\mu m$ of each [14, 47, 57, 68]) were deposited through the GIS. (Carbon can also be used to enhance the contrast of biological specimen in SEM images [94].) For the metal deposition, an ion current of $0.44nA$ was used resulting in a current density of around $3pA/\mu m^2$.

Besides the volume selected for the Slice and View, trenches of width $6\mu m$ and $5\mu m$ depth were milled to avoid redeposition of milled material [3, 16, 34]. These dimensions are set for the milling of silicon, resulting in extended milling of embedded brain tissue. Then final polishing steps of the surface with a low ion current $0.44nA$ were conducted to avoid curtaining [57]. The volume to be milled and resulting surface area to be investigated was chosen such that the ion mill always sputtered an excess amount of material to diminishing edge effects [34].

In the experiments conducted, a driftcorrection SIM was taken to decrease this artifact. This is the 'X' seen in the perspective SEM shown in **Fig. 4.9**. Even though the stage is

relaively stationary, small shifts in the (x, z) directions may be required (directions as in **Fig. 4.11**). The SIM correction is used for this.
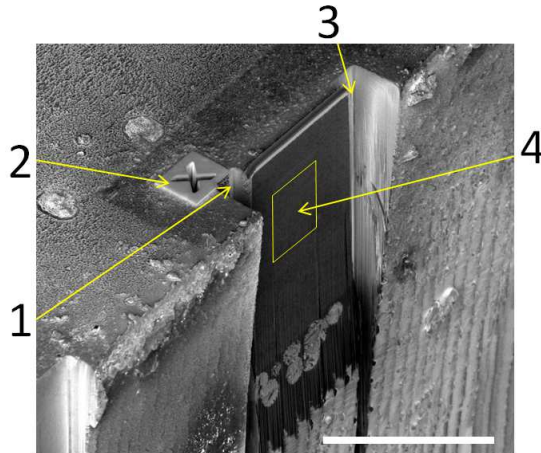

Figure 4.9: A labeled SEM micrograph taken after a Slice and View. (1) and (3): trenches to reduce redeposition; (2) the 'X' is the driftcorrection mark, and (4) the ROI of the Slice and View, also seen is the hydrogen deposition which gives the region a brighter hue. Scale bar: $30 \mu m$.

4.4.2 Trench Milling

For investigating how the accuracy of the ion mill varied as a function of the ion current used, regions of empty Epon empoxy was used. To evaluate the accuracy, trenches were milled using different ion currents. The ion beam was first focused using a current of $26pA$. The acceleration voltage used was $30kV$ as this is the voltage used in the instrument alignment.

For milling the trenches, a rough cut ($9nA$) of the sample was conducted to expose a surface area of sufficient size [47]. Then layers of $1\mu m$ conductive carbon and $1\mu m$ of Pt was deposited on top for charge reduction and sample protection. After the deposition, trenches were milled using the 'Line mill' tool of the FIB. This was chosen to ensure that the ion beam was focused as precisely as possible.

The ion currents investigated were: $26pA$, $46pA$, $90pA$, $.26nA$, $0.44nA$, $0.9nA$, $2.7nA$, $6.5nA$, $9nA$ and $20nA$. Having performed the trench milling, SEM images were collected using the TLD in the Field free mode and with a resolution of 2048×1768 and dwell time of $100\mu s$ with stage orientations of $0°$ and $52°$. The different ion trenches were milled in close proximity to ease their comparison.
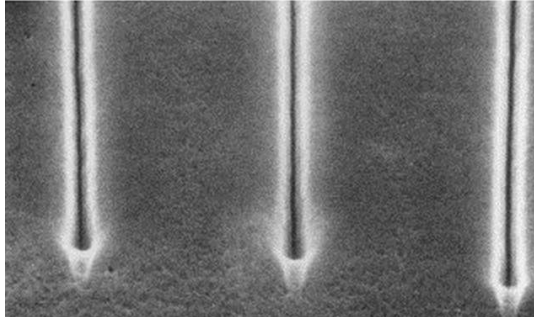

Figure 4.10: Example FIB milled lines, figure from [37]. For the trench milling experiments, after having milled a similar array, a cross-section was exposed and polished to ensure as accurate measurements as possible.

4.4.3 $S\&V$ **of brain tissue**

The $FEI\ Slice\ and\ View\ G2$ software was used for automatic Slice and View [14]. The FIB milling depth was $5\mu m$, and surface chosen such as to ensure at least 120 slices of the desired thickness [34]. The SEM imaging parameters noted in **Sec. 4.4.1** was implemented, and FIB milling parameters during the Slice and View experiments were $30kV$ and $0.9nA$.

A SIM for drift-correction was used during the Slice and View experiments. A fiducial mark of platinum with height $0.6\mu m$ was deposited with the GIS using a deposition current of $0.26pA$, and the mark was milled with a current of $0.9nA$. FIB driftcorrection parameters of 1024×884 pixels and a dwell time of $3\mu s$ caused negligible deterorating sputtering while maintaining the drift correction.
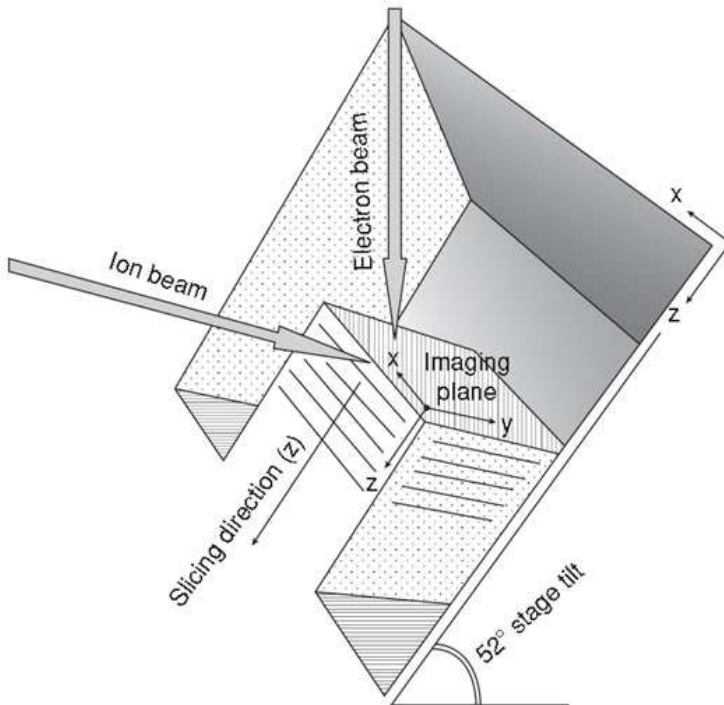
Figure 4.11: A schematic showing the principle of the Slice and View. The ion beam is used to mill a slice, before the electron beam scans the exposed surface. The stage is then shifted in the z-direction, and the processed is repeated. Figure from [47].

Axon tracing

For the axon tracing experiments, different slice thicknesses were tested to see the influence on the micrograph quality. Increased section thickness was investigated as this increases the volume investigated per experiment. For testing the accuracy of the alignment and sectioned volume, a modified protocol from [27] was used to compare the axon tracing capability of the FIB/SEM with the SBF/SEM approach. A schematic of the setup is seen in **Fig. 4.12**.

The tracing was semi-automatic, and the axons were traced through the use of the 'Magic Wand' tool in $Avizo^{TM}\ Fire$ 7.1. The axons present were reconstructed by the operator
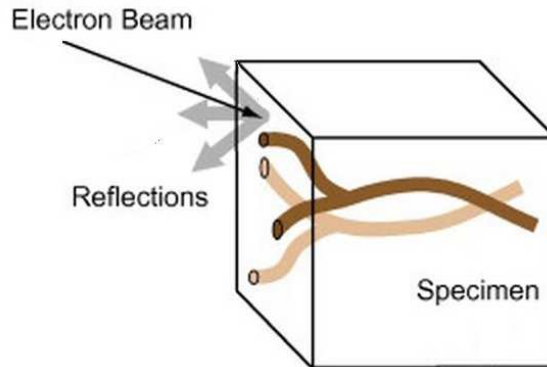
Figure 4.12: A schematic of the principle of tracing axons. If the slicing (z) direction is aligned
according to the propagating axon, then a Slice and View can segment and reconstruct
the axon according to its cross-sections. Figure (modified) from [27].

marking one axon cross-section in one of the slices, and adjusting the threshold for tracing
the propagating contour through the volume once.

4.4.4   EDX for preliminary mapping

The use of the EDX detector and the potential for element tracing was investigated. Ad-
equate signal and low dead time was to be obtained. Increasing the electron beam energy
increases the CPS; the dead time was always held below 20% when collecting the maps.
A CPS of 2000 is considered typical ([32]), and the parameters chosen yielded a CPS in
its viciniy. During the experiments, a voltage of $30kV$ and a current of $2.7nA$ was found
to ensured this and was therefore used.

Characterisitc X-rays

The EDX detector was tested to find adequate EDX parameters in the investigations. The
parameters were tested to find good count rates ensuring a resonable collection time, while

also making sure that the dead time was held low. The spectrums were collected until the signal stabilized. Knowing the elements present could be used to check the 'Expert ID' included in the $EDAX^{TM}$ software.

EDX model experiments

For the preliminary mapping experiments, the sample was located and the stage tilted such that EDX signals could be collected from the side walls (**Fig. 4.13**). When collecting perspective views of the model, micrographs were collected both with the microscope in EDX mode and with the optimized Field Free parameters.
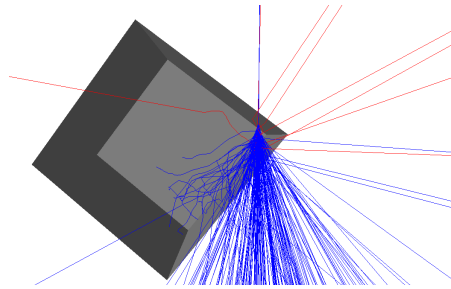

Figure 4.13: A Monte Carlo simulation showing the principle of the EDX model experiments (**Sec. 5.3.2**). With Pt layers deposited on the sidewall of the block, the sample was oriented such that the electron interaction volume (**Sec. 3.1**) excited the characteristic wavelengths of the Pt layers on the wall.

For the collection of the elemental maps used in the tracing estimations, an EDX spectrum of the elements to be located was first collected. The sample orientations are defined in **Fig. 5.23**. This was done by positioning the sample and tilting such that the Pt layers were 'In View' of the SEM detectors, in orientation I. Then the EDX spectrum were collected. The raster resolution, dwell time and collection time were collected ensuring the spectrum had stabilized (> 5000 counts). Having defined the elements to be collected, elemental maps were collected both from orientation I and III. EDX maps were also collected at orientation II sample tilt, to see the tracing potential from the 'Top View'.

The estimation protocol used for the tracing potential is illustrated in **fig. 4.14**. The gradi-

ent of the elemental dot map was used to measure d_1, the rest is given through **Eq. 4.3**. The
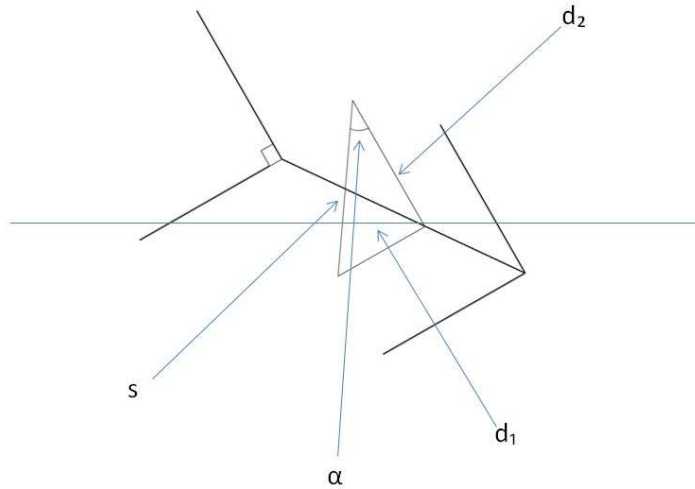
Figure 4.14: A schematic illustrating the geometry, angle and catheti used in **Eq. 4.3** and **4.3**. The blue horizontal line represents the microscope plane when the EDX elemental map is collected.

intrument and geometry sets $\alpha = 38°$, and the tracing potential was therefore estimated:

$$d_2 = d_1/sin\alpha \tag{4.2}$$

$$s = \sqrt{d_2^2 + (tan\alpha \cdot d_2)^2} \tag{4.3}$$

Double labeled sample experiments

The sample received was coated with $40nm\ Cr$ to avoid charging, and prepared is in **Sec. 4.1**. It was further investigated with the parameters noted in the paragraph above.

A manual cut with a scalpel was also conducted to expose different parts of the sample, as FIB preparation of large dimensions are very time-consuming. Havng exposed the areas, rough cuts were made (high current) with the FIB to ensure an even surface. From this

surface EDX maps were collected with the parameters stated in the paragraph above.
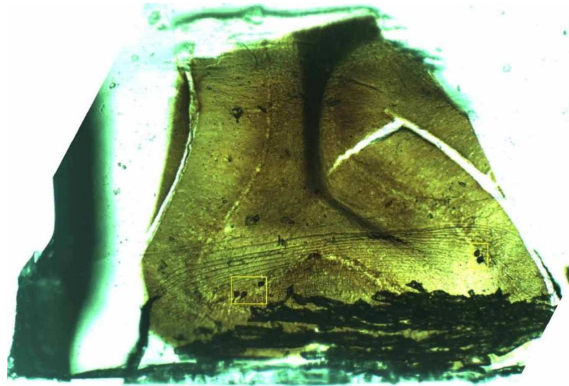
Figure 4.15: The Epon epoxy embedded, DAB stained and gold intensified sample investigated. Figure, courtesy of Jørgen Sugar.

4.5 Artifacts

When using the FIB/SEM, numerous artifacts need to be taken into account when trying to optimize the micrograph. For site spesific studies, previous knowledge of the ROI (optical microsopy or X-ray microtomagrphy) is of high value [3], due to the required sample geometry (**Fig. 4.19**), and milling time for new area exposure. Artifats may develop through the scan; e.g. the use of a low acceleration voltage may induce hydrocarbon deposition and a higher diameter of the electron probe (reduce resolution [80]), while the use of a high voltage may induce chemical crosslinking in the sample and a larger depth of the interaction volume deteriorating the image sharpness.

Hydrocarbon deposition

Despite the vacuum in the SEM chamber, hydrocarbons are still present is small amounts. The electron interactions occuring at the sample surface may lead to the desposition of this residue hydrocarbons. The deposition rate is dependent on the parameters of the SEM, and the deposition rate is higest at low voltages. This is because low energy SE has an energy that matches the dissiciation peak of surface adsorbed hydrocarbon precursor molecules, surface adsorbed precursors are present in the high vacuum environment [87]. And at low energies, the SE yield is higest (**Fig. 3.4b**).

<div align="center">(a)   (b)</div>
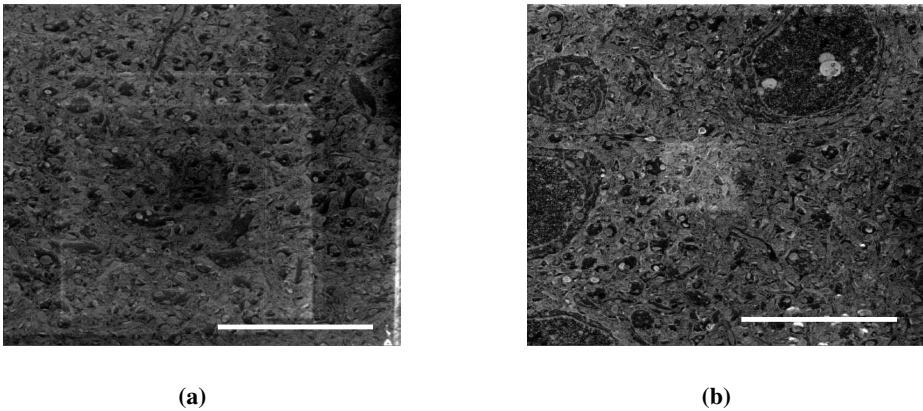
Figure 4.16: Two examples of hydrocarbon deposition. The different hues of the squares results from different time spent focusing the SEM with the respective fields of view. Scale bars: $(a, b) = (10\mu m)$.

The hydrocarbon deposition occurs quickly during the Slice and View protocol with the parameters used for the optimum images. But since material is sequentially removed between the micrographs, so is the deposited hydrocarbon. In the montage shown **Fig. 4.17** the hydrocarbon deposition is evident resulting from a pause in the Slice and View for the refocusing of the SEM.

Figure 4.17: A montage of 5 micrographs showing the hydrocarbon deposition when refocusing the SEM. The focus is increased in the 2 image, and the brighter square (higher SE yield) is removed through the following sequence.

Drift

Drift with respect to automated FIB/SEM investigation is the unintended movement of the stage during the process. Measures to reduce drift used in this Thesis include the use of a SIM driftcorrection between each slice in the Slice and View process (**Fig. 4.9**), the insertion of the sampl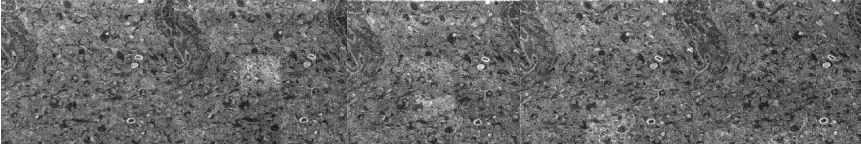e in the vacuum chamber $12h$ before the experiment for thermal changes to dissipate ([33]), and the use of Cu tape (more beneficial than carbon tape which contains volative adhesives and is elastic and porous). Cu tape also has better conductivity than carbon tape.

Despite this, drift is hard to avoid. The image stack example in **Fig. 4.18** consists of 100 slices and have been aligned using the StackReg plugin in FIJI. The resulting drift measured is: $(\Delta x, \Delta y) = (0.73\mu m, 1.07\mu m)$.
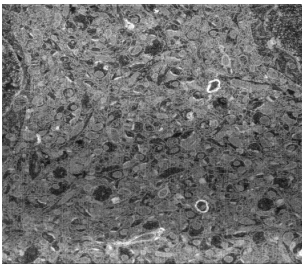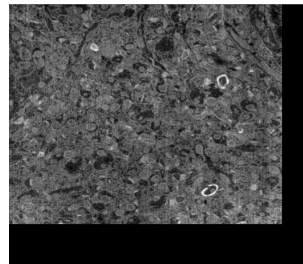
(a)   (b)

Figure 4.18: An example of the resulting drift despite countermeasures when the protocol was run unsupervised. the slices are separated by $2\mu m$. (a): slice number 1, (b): slice number 100.

Curtaining

Curtaining is the appearance of verical lines in the SEM micrograph. This is caused by uneven milling of the surface, and is often a result of an uneven sample topography [3]. Uneven topography predisposes different amounts of milling of the sample as caused by position, and cannot be taken into account by the controlling software. Therefore it is important that the sample surface is even. Topography is decreased by depositing a metal layer on top of the sample. This decreases the topography, but does not remove the problem. The optimum sample geomtry is indicated in **Fig. 4.19**.
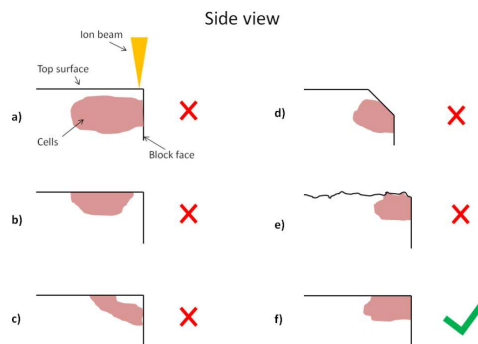
Figure 4.19: The sample geometry is very important in investigating the samples in FIB. Two sample preparation protocols were investigated in this thesis. Schematic, courtesy of Ken Roger Ervik.

The curtaining shown in **Fig. 4.20** developed after the surface and volume had been prepared and polished for a Slice and View. It was introduced by a software controlled low current Rought cut which normally did not introduce curtaining.

Charging

Charging of an insulating sample under investigation is a problem for FIB/SEM analysis. Investigating a charged sample will lead to a deflection of the beam in question [15, 98]. This may be seen as e.g. inaccurate milling with FIB, or degraded resolution or horizontal
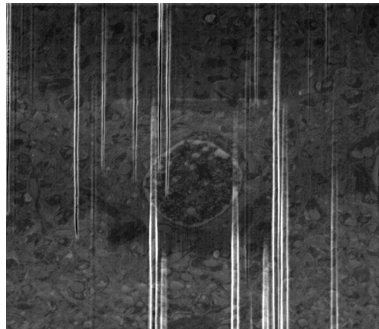
Figure 4.20: Appearing curtaining as caused by the use of an automated software Rough Cut despite using a polish ion current density.

lines with SEM. Various methods are applicable to reduce charging of insulating specimen, the use of low voltage and specimen metal coating are common [55]. By adhering the insulating specimen by a conductive measure to the sample stub and coating the specimen with a metal, the charging most often is sufficiently reduced. The alternating use of the FIB and SEM will also lead to a reduced charging, as the two particles are of opposite charge. But this predisposes that the time of SEM and ion milling is similar [3].
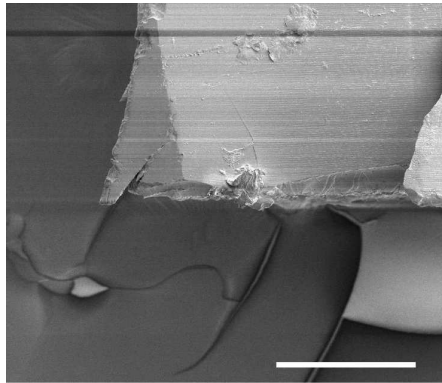
Figure 4.21: The horisontal lines and bright spots indicates accumulated charge due to the sample being inherently non-condutive [55]. Scale bar: $200\mu m$.

Chapter 5

Results

5.1 Trench milling

The FIB accuracy is of very high importance for the FIB/SEM protocol. The milling rates varies with the ion beam current, and when milling nanoscale dimensions, small ion beam currents are preferred [107]. Therefore, investigations of how the parameters of the ion beam influenced the accuracy of the ion milling were conducted, to see the extent of the effects on the embedded brain tissue. The expermental design was to investigate the accuracy of milled trenches (**Fig. 5.1**).

Using the ion beam with a chosen voltage and current influences the accuracy of the ion milling. The discussion of the focus of the ion beam is analogous to the electron beam. In general, the more ions and higher the beam energy, the higher effective sputtering rate. But at the same time, the lower the accuracy of the milled material. The effective sputter rate and FIB induced damage increases with increasing beam energy [18]. Therefore the importance of the polishing steps with a low ion current to ensure the highest accuracy of the regions sputtered. But, the less ions impacting the material, the less material sputtered, and thus the more time is required for the sputtering of selected regions.

Figure 5.1: (a): the selection of a line to sputter with the ion beam; (b): the experimental variable was how the diameter of the trenches varied as a function of the current used.

Having set the dimensions of the trenches to be milled (x, y, z), the current determines the time required for the protocol. The 'line mill' of the instrument was used to en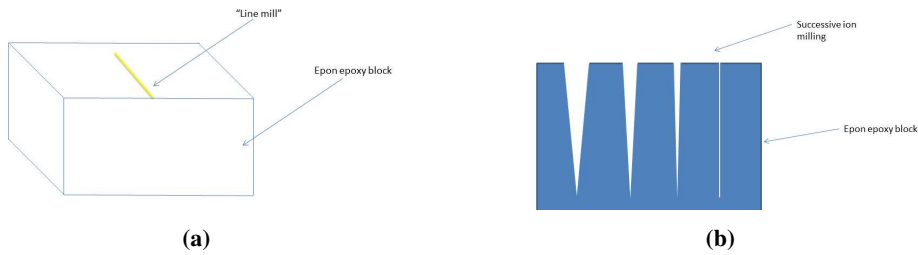sure that the trenches were milled as precisely as possible. This implies that sequential pixels are milled (**Fig. 5.1a**). The experimental variable measured was the diameter of the resulting trenches. Further details are noted in **Sec. 5.1**. The rationale for the investigation was to optimize the milling accuracy with respect to time while conserving adequate accuracy. The trenches were milled in close proximity to ease their comparison. An investstigation of how the magnification (thus pixel resolution) influenced the accuracy was also investigated, but this effect proved negligable with respect to the trench diameter (data not shown).

To ensure decreased charging and topography, layers of Pt and conductive carbon were deposited on the Epon block. The diameter of the trenches did deviate when comparing the 'top view' relative the $52°$ angle view. This is seen when comparing **Fig. 5.4a** and **5.5c** where the trench diameter increases when milling Epon epoxy relative deposited metal. But this difference decreases with increasing current, as the area sputtered in general increases. In **Fig. 5.3** the maximum and minimum diameter from the top view is also indicated, which indicates that the shift when excessive area is sputtered also happens around $0.9nA$.

Decreasing the acceleration voltage (lower beam energy) has also been reported to notably increase the accuracy of the ion mill ([88]). However, the ion beam has to be aligned for the voltage used, creating a correspondance between the position chosen in the software
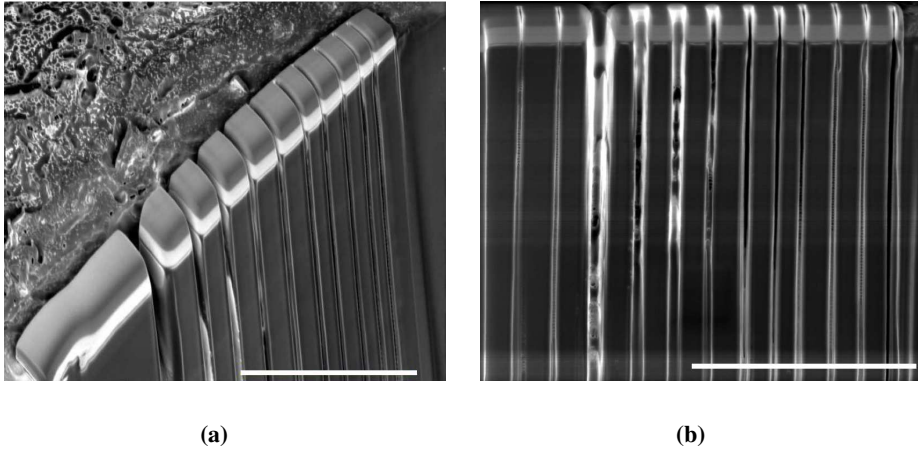
Figure 5.2: (a): A persepctive view of the milled trenches; (b): similar trenches imaged perpendicularly. Scale bars: (a,b): $10\mu m$

and on the sample to be milled. The instrument used is these investigations is aligned for $30kV$, such that a decrease in this led to an erroneously ion beam aim, seen in **Fig. 5.4b**, where the ion aim trench to be milled was set on the metal. Also seen in the same figure is the increased degraded area around the milled trench, which also indicates that the sputtering energy was poorly focused.

As seen in **Fig. 5.3**, the accuracy of the mill with a current of $0.9nA$ was relatively high, and the consistency unsurpassed. This led to $0.9nA$ being the current used for the Slice and View experiments. The measurement at a depth of $20\mu m$ was chosen as re-embedding the sample in empty Epon epoxy after labeling leads to ROIs in general being above a depth of $20\mu m$ in the block. (A ROI location of $< 30\mu m$ has also been stated as a 'secret to success' concerning even FIB milling [33].) Using a magnification of $8.000X$ implies a height of the ROI of $12\mu m$. And with this magnification the interneurons may be resolved. The use of $10.000X$ -which further improves the sharpness of the image- reduces the height to $11\mu m$. Thus, ensuring accurate miling to $20\mu m$ may decrease the development of excessive curtaining in the ROIs investigated.
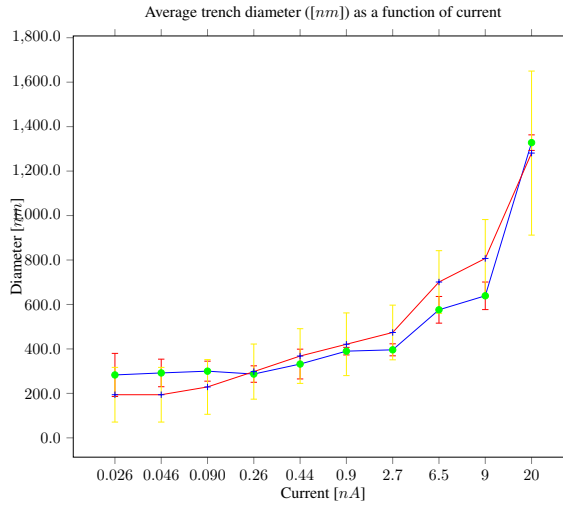
Figure 5.3: In this figure the blue line shows how the trench diameter varied as a function of the ion current used when milling Epon epoxy, averaged over the three depths. The red line are the average values of the measurements of the diameter from the 'Top view' (**Fig. 5.4a**). The maximum diameter of the area degraded by sputtering and the minimum diameter of the trench which evidently propagated through the block was averaged.

(a)

(b)
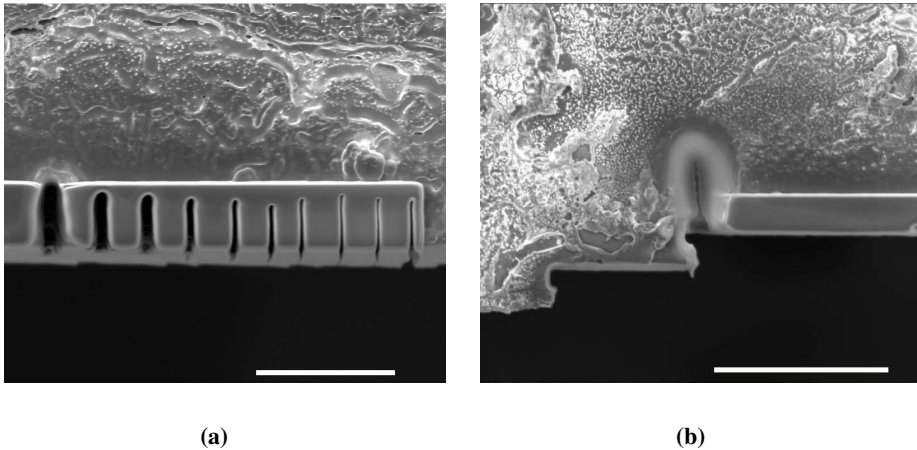
Figure 5.4: (a): The figure shows the top view of the ion trenches. As is also seen in the tilted images, the trench diameter increases when brain tissue is milled; (b): The figure shows a SEM micrograph post an ion mill where the line to be milled was placed within the deposited platinum. A rotation of the stage also revealed that the depth of the mill as inaccurate, signified by the degraded surrounding area. Scale bars: (a): $5\mu m$, (b): $10 mum$.

(a)

(b)

(c)
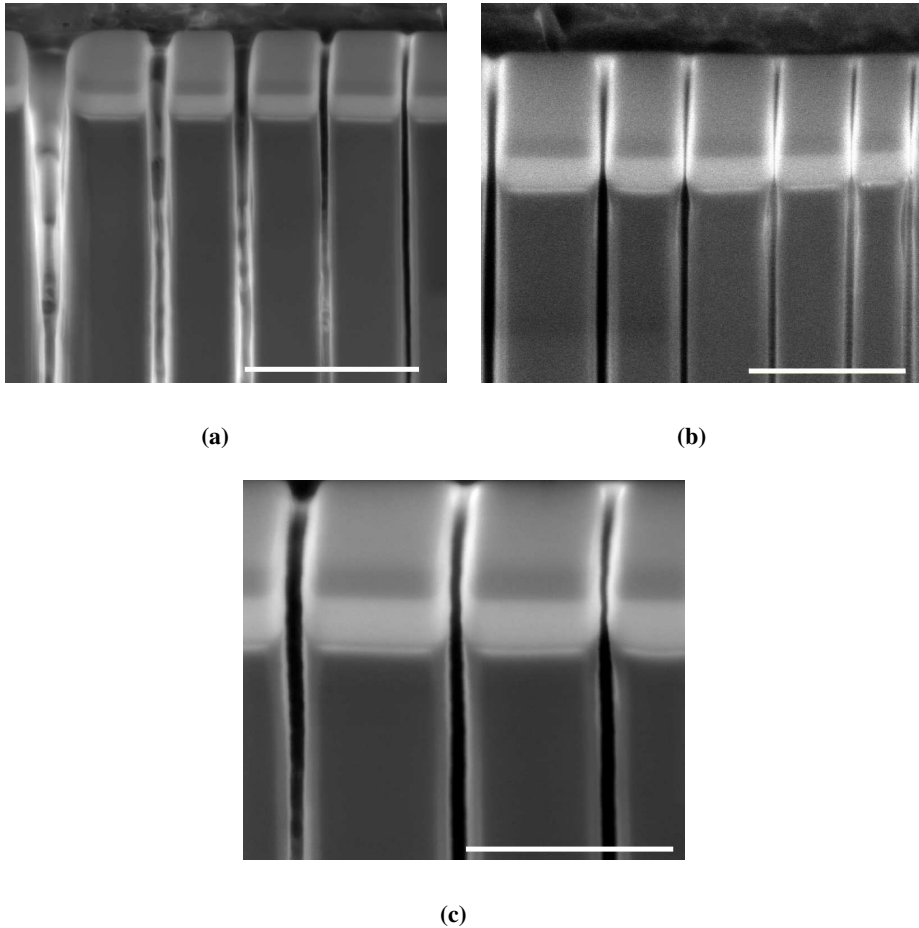
Figure 5.5: A comparison of the trench diameters with respect to the material milled. (a): trenches milled with the 5 highest currents. (b): trenches milled with the 6 lowest currents, the $0.9nA$ trench is imaged in both (a) and (b); (c): a close up of $0.9nA$, 0.46 and $0.24nA$ where the difference between the diameter of the metal mill vs Epon epoxy was clear. The scale bars: (a): $5\mu m$, (b): $3\mu m$ and (c): $3\mu m$.

5.2   Brain tissue investigations

The results from the ion beam accuracy investigations were conducted to optimize the accuracy for performing the most efficient processing of Epon embedded brain tissue. The results from the accuracy investigations led to the Slice and View current and voltage used being $0.9nA$ and $30kV$.

Research questions investgated utilizing the brain samples were the potential for 3D reconstruction of entities within the tissue, and specifically a labeled subtype of interneurons (Stellate Layer II interneurons). The sections opens with some examples of the morphology observed during the investigations. Two embedding protocols were investigated for their effect on the results of the FIB/SEM processing protocol. As the volume is limited in a FIB/SEM Slice and View, different slice thicknesses were investigated for their effect on the severity of the curtaining artifact. 3D reconstruction of densly stained axons were investigated for the potential of semi-automatic tracing of a protocol usually requiring a high degree of expertice.

The samples investigated in this thesis were prepared by Ph.D candidate Jørgen Sugar at St. Olav's University Hospital.

Brain tissue morphology

For the selection of the ROI for the Slice and View, one first conducts a Rough cut of the FIB block. After the rough cut, a polishing step is conducted if required. The neuropil seen on the newly exposed SEM surface requires that the operator knows the required SEM magnification and distinguishing features of the entities of interest before initiating a Slice and View. The morphology of the DAB stained tissue was evident when using a magnification of $8.000X$, such that this magnification was used for most of the investigations. The use of as low magnification as possible allows for a search over larger surface areas.

In **Fig. 5.6**, the morphology of the DAB labeled interneurons is seen. The labeling was

performed by Ph.D candidate Jørgen Sugar. This was used as a reference for the later interneuron reconstruction **Sec. 5.2.2**.

(a)   **(b)**
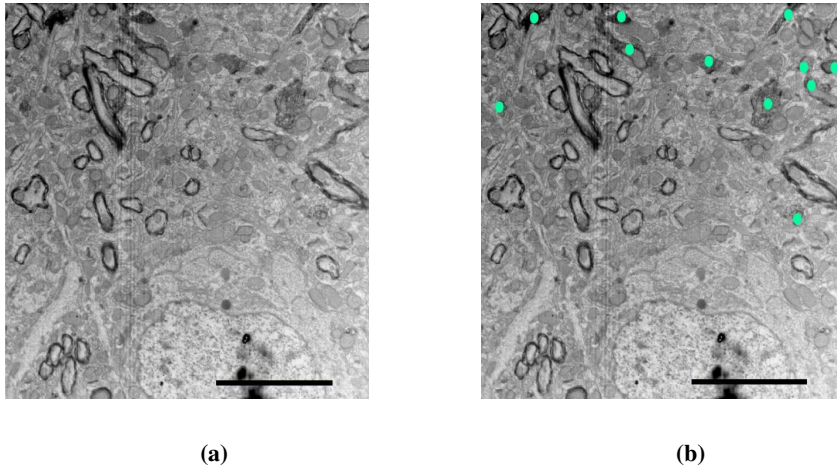
Figure 5.6: The identification of the DAB morphology used for the labeling of the images in the Slice and View stack. The images have been inverted and y-elongated. (a) original SEM micrograph (b) the same image with interneurons labeled turquoise, labeling done by Jørgen Sugar. Scale bars: $(a, b) = (5\mu m)$.

(a)   **(b)**
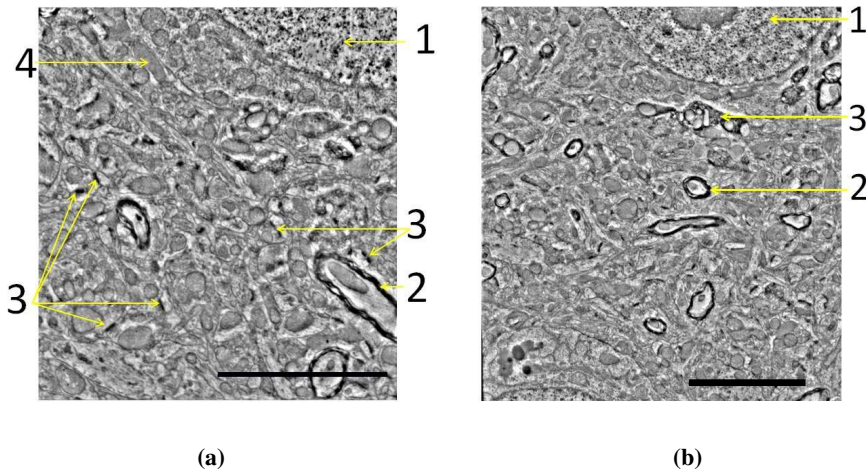
Figure 5.7: This figure identifies examples of some of the entities resolved at this magnifcation with the optimize SEM parameters. The numbers identify; (a): 1 :nucleus, 2 : axon, 3 :synapses, 4 : mitochondria; and (b): 1 :nucleus, 2 : axon, 3 :interneuron. Scale bars: $(5\mu m)$.

With the optimized SEM parameters, numerous other entities are distinguishable, some of which are identified in **Fig. 5.7**. The results show that with these parameters even synapses can be identified. Synapse reconstruction with similar SEM parameters have been performed; FIB/SEM 3D reconstruction can be used to categorize the synapses as asymmetric and symmetric [4, 22, 56].

5.2.1 Brain tissue embedding protocol

Special preparation protocols are necessary when brain tissue is to be investigated with electron microscopy (**Sec. 3.4**). The brain tissue has to be embedded in a resign, in these investigations Epon epoxy was used. When the preparation is complete, the brain tissue is embedded between two layers of epoxy as seen in **Fig. 5.8a**. For FIB investigations, the geometry of the samples to be investigated is very important **Fig. 4.19**. An optional preparation protocol is to re-embedd the tissue on a new block of Epon epoxy. This allows the use of an ultramicrotome for the removal of the top layer of Epon epoxy, leaving the brain tissue directly exposed. This protocol is more beneficial for the investigations with FIB, but is more time-consuming with respect to the sample preparation. Therefore, the two protocols were compared, a *thin section* and a *re-embedded section* as shown in **Fig. 5.8**. The quality of the protocols were evaluated with the developing curtaining and effect of precipitated uranyl crystals (**Sec. 3.4**). Curtaining may develop due to difference in

(a)   (b)
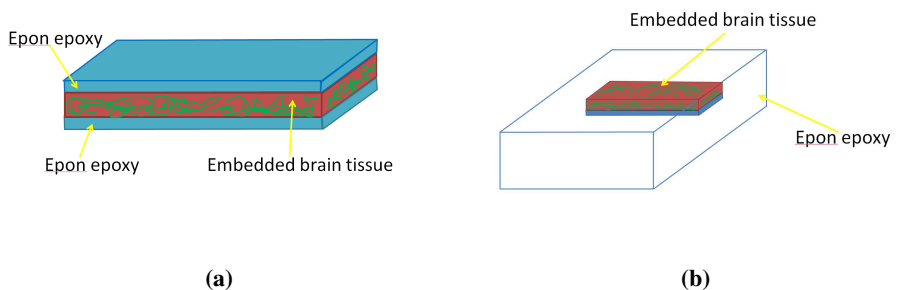
Figure 5.8: The preparation protocol for the investigation of brain tissue with electron microscopy requires that the tissue is embedded in plastic **Sec. 3.4**. (a): the thin section and (b): the re-embedded section.

sputtering rate (often caused by specimen topography [89]), but it may also be caused by inherent material differences in the sample [3]. The difference in position of the brain tissue in regards to the top of the sample is seen in figure **Fig. 5.9**. It was found that re-embedding the tissue proved superior in regards to the quality of the obtained Slice and View stacks. This was caused by e.g. when using the ion beam to locate the ROI, crystals could unexpectedly appear above the ROI during the pre-processing. Using thin section also required that the ion beam had to mill deeper into the sample, which also influences the curtaining.

In contrast, a re-embedded ultramicrotomed sample positioned the tissue as close to the ion beam impact point as possible and removes any boundary effects between different compositions (decreases possible preferential milling [67, 89]). It also decreases the required milling depth for ROI exposure, and removes possible crystalization above ROI's. Previous work by the candidate has shown that using pressure through the sample prepara-

| (a) | (b) |
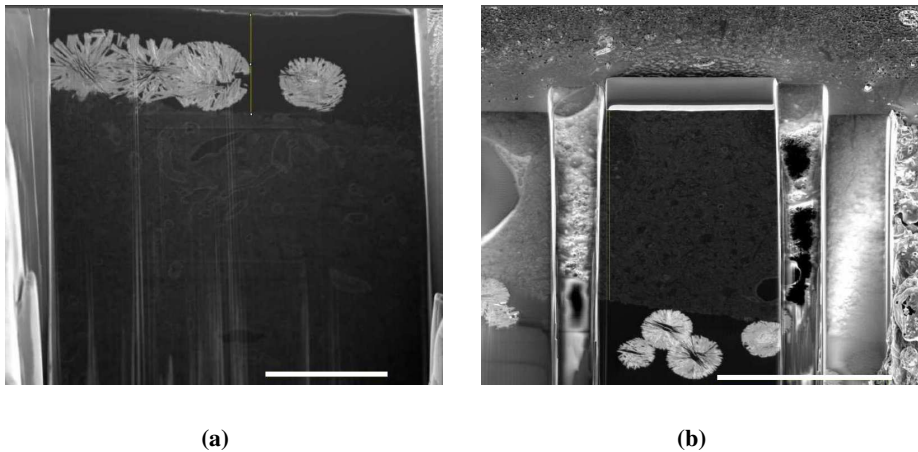
Figure 5.9: (a): Crystalliation at the top of the ROI which may have caused curtaining. The yellow line in the image is $8\mu m$. The microhgraph is taken after the $S\&V$, and the ROI can be seen in the center square where the hydrocarbon deposition is clear. Figure from [91]. (b): A re-embedded sample trimmed with an ultramicrotome. The yellow line measures a depth of $22nm$. The region is prepared for a Slice and View. Scale bars: (a):$10\mu m$, (b): $20\mu m$.

tion protocol reduces the voids in the sample, which may cause problems during the Slice ad View protocol (e.g. for EDX3D reconstruction [76]).

5.2.2 3D modeling of brain tissue

The use of the FIB/SEM and the Slice and View protocol introduces the possibility of creating nearly aligned serial images that can be used in the generation of 3D models of tissue investigated. This is made more convenient by the use of accessory software, introduced in **Sec. 4.3**. The investigation of the optimization of SEM parameters was done in previous work by the candidate ([42]), and the FIB parameters found in **Sec. 5.1** was used in the Slice and View protocols. The results presented in this section investigated how the slice thickness influenced the quality of the micrgraphs, the potential for semi-automatic tracing, and 3D reconstruction of a selected subset of cells.

Slice thinkness during Slice and View

Despite it numerous advantages, one of the disadvatages of conducting a Slice and View for 3D reconstruction is the limited volume that can be investigated per experiment. The required resolution in the x, y plane sets the bounds for the magnification and thus dimension. The required resolution in the $z - dimension$ may not be bounded by the same requirements. Thus if detailed data about the volume between the slices is of less importance, the slice thickness may be increased to allow the investigation of larger volumes. Therefore, FIB parameters found to be applicable for a slice thickness of $20nm$ was used, as this slice thickness has been used to reconstruct brain tissue [4, 56]. Different slice thickness was investigated to see how this influenced the curtaining. The thicknesses investigated were $60nm$, $40nm$ and $20nm$, all of the re-embedded tissue. The results were also compared to a $20nm$ Slice and View of a thin sample, a montage of which may be seen in **Fig. 5.14**.

A slice thickness of $60nm$ led to severe curtaining on selected images through the stack. But, the curtains -though severe- did not propagate through the stack. This is in general a common problem for Slice and View, and the cause for the important polishing of the ROI before initiating the protocol. A 'passing curtain' can be seen in **Fig. 5.15**. The $40nm$ slice thickness yielded similar quality as the $20nm$ stack, and can therefore to a

similar degree be chosen if the required $z - dimensional$ resolution is $80nm$ (a voxel size half as small as the entity to follow [77]). But this benefits from what is followed to be parallel with the slicing direction. The stack with a thickness of $60nm$ was still used to trace axons. Some additional steps in FIJI were required for some of the slices before the StackReg plugin (**Sec. 4.3.1**). The approach was applicable with this thickness, and since the required resolution in the $z - direction$ is debated ([71]), this might be an approach for the investigation of larger volumes. But the $z - resolution$ being as such, other SEM parameters might be better suited with respect to a decreased resolution for a more effective data collection. But this again has to be weighted against what is desired, for maximum efficiency there are instruments developed primarily for speed (e.g. Multi-beam SEM with 61 electron beams and 61 detectors [71]).

Axon tracing

The annotation of volume EM data for 3D reconstruction often predisposes a high level of expertise of the researcher, and ways to diminish this requirement is very valuable [41]. The results from the slice thickness investigations were used in automatic 3D rendering experiments. The reason for such an investingations is the time required for the data post-processing protocol for 3D rendering, especially if the optimum SEM parameters are used.

The micrographs were processed with FIJI and Avizo Fire as described in **sec. 4.3**. The image processing steps done in advance of the 3D reconstruction (**Fig. 5.13**) makes the volume rendering both more accurace and convenient. The increased similarity of the images (FFT bandpass filtering) consituting the stack also makes the thresholds set for one slice applicable for the remainder, which is important for automatic tracing.

The experiment was conducted in comparison with the application of SBF/SEM for semi-automatic axon tracing [27]. Reducing human intervention for the axon reconstruction is of high interest due to the enormous complexity of the circuitry in the brain. Therefore, using FIB/SEM in a similar respect for data collection was compared to the SBF/SEM approach. The accuracy and time-consumption of the protocols was investigated. The

optimized SEM parameters were utilized, and stacks with thickness' of $20nm$, $40nm$ and $60nm$ of re-embedded samples. The results are shown in **Fig. 5.11a**, **5.11c** and **5.11e**. Further details are noted in **Sec. 4.4.3**. The slice thickness of $60nm$ did impose some additional difficulties in aligning the slices. This is evident in the reduced dimension in the example slice in **Fig. 5.11e**. The stack was cropped to avoid the curtains while conserving the axons. This was not required for the $40nm$ slice thickness. This protocol can probably be generalized for similarly densely stained tissue.

Regarding the accuracy of the semi-automated reconstructions, comparing the constructed figures to the ones composed through the protocol using the SBF/SEM (**Fig. 2.6**), the accuracy of the tracing with FIB/SEM seem to generate similarily accurate models. But this is something that has to be evaluated by trained experts.

Sharpness measurements

The SEM focus deteriorates through the Slice and View protocol when the instrument is run unsupervised. The resolution results of the axons tracing experiments were measured through MATLAB as described further in **Sec. 4.3.3**. The resolution can be measured through the micrograph sharpness. For the three experiments with the thickness' $20nm$, $40nm$ and $60nm$, the sharpness' are presented in **Tab. 5.1** and **5.2**. The number of slices in the respective stacks were: 100, 100 and 86.

The results show that axon tracing with the FIB/SEM was possible with a raw data resolution of $50nm$. The results also show that data post-processing can both increase or decrease the measured resolution, but these results are highly biased by the example slice measured. The FFT bandpass processing makes the contrasts in the volume more similar and easily traceable.
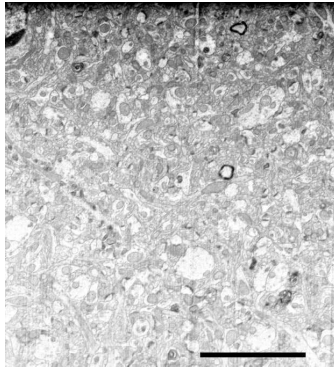
(a)

(b)
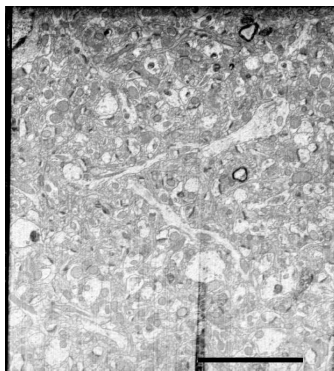
(c)

Figure 5.10: Slice number 18, 22 and 26 extracted from the same Slice and View with slice thickness of $60nm$, thus separated by four slices ($240nm$). The images have been inverted and y-elongated. Seen in the images is a 'passing curtain', as seen by the large darker area towards the center. Scale bars: $(a, b, c) = (5\mu m)$.

(a)

(b)

(c)

(d)

(e)

(f)
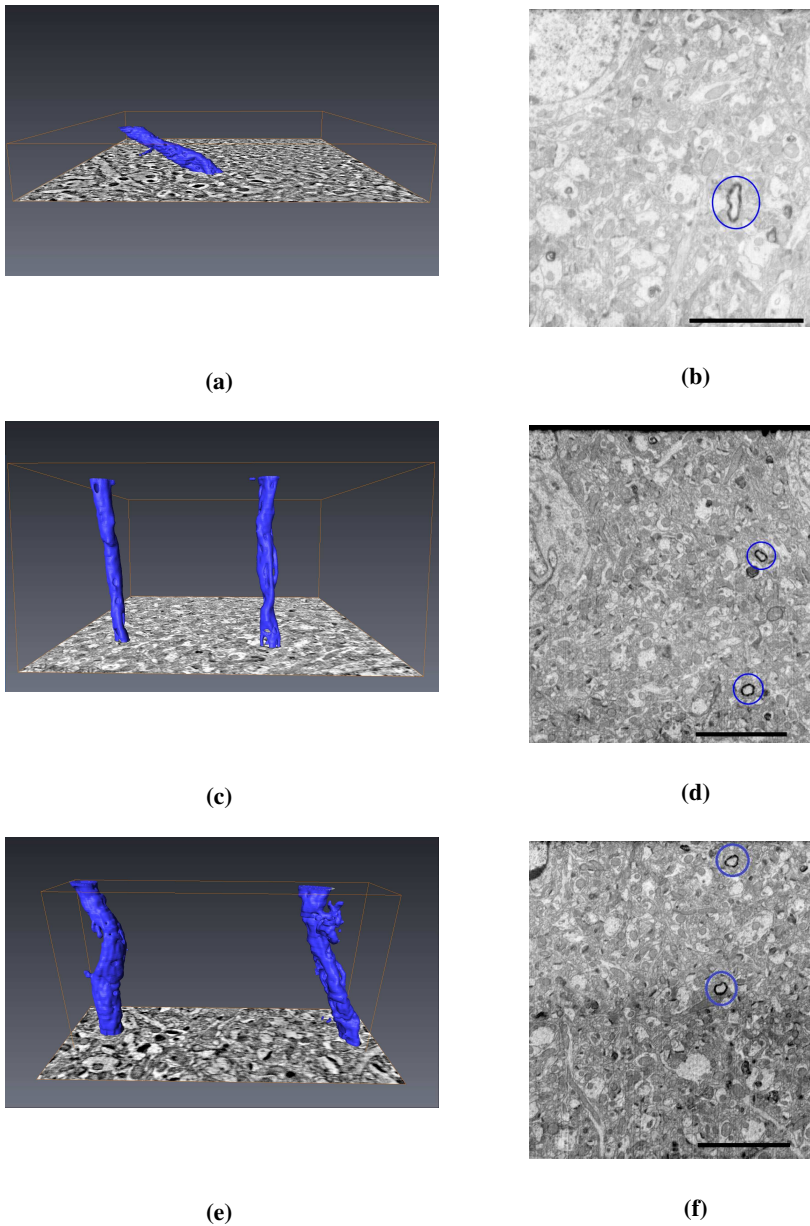
Figure 5.11: Shown in each line is the semi-automatic reconstruction of axons with the initial slice on the bottom. The model is constructed with aligned imaged stacked on top of each other. Besides the model is an example slice used for its construction. The axons reconstructed are circled with blue lines. Scale bars: $(b, d, f) = (5\mu m)$. (a): slice thickness $20nm$, 100 slices, z-dimesion: $2\mu m$. (b): slice thickness $40nm$, number of slices: 100, z-dimension: $4\mu m$. (c): slice thickness $60nm$, number of slices: 86. Z-dimension: $5160nm$.

Slice thickness	Average Sharpness, #1	Average Sharpness, #86	Ratio
$20nm$	29.4	34.5	85.2%
$40nm$	35.5	41.6	85.3%
$60nm$	41.7	52.0	80.1%

Table 5.1: How the sharpness ($[nm^{-1}]$) varied through the stacks of differing slice thickness' and lengths.

Slice thickness	Average Sharpness, #1	Average Sharpness, #86	Ratio
$20nm$	26.1	28.7	90.9%
$40nm$	41.9	44.6	93.9%
$60nm$	37.1	36.8	100.8%

Table 5.2: Sharpness meaurements ($[nm^{-1}]$) of the processed image stacks used for the reconstruction.

Neuron reconstruction

The serially aligned FIB/SEM Slice and View micrographs of the embedded brain tissue can be used to reconstruct selected organelles, if the micrograph quality is sufficient. The optimized SEM and FIB parameters found earlier were therefore used to collect as high quality data as possible.

From the image stacks obtained, the resolution/level of detail was used to reconstruct the inner organelles of the neurons. Slice number 34 in the stack used for the model creation is shown in **Fig. 5.12b**, and a model showing a protruding dendrite from a cell body is shown in **Fig. 5.12a**. The results show that the data quality is sufficient for the reconstruction of the entity desired.

Interneuron reconstruction

In the brain tissue samples, a selected subset of cells had been specifically labeled using the DAB protocol **Sec. 4.2**. Experiments were conducted to investigate the accuracy with which the selected cells could be identified and reconstructed from the collected FIB stacks.

(a)

(b)
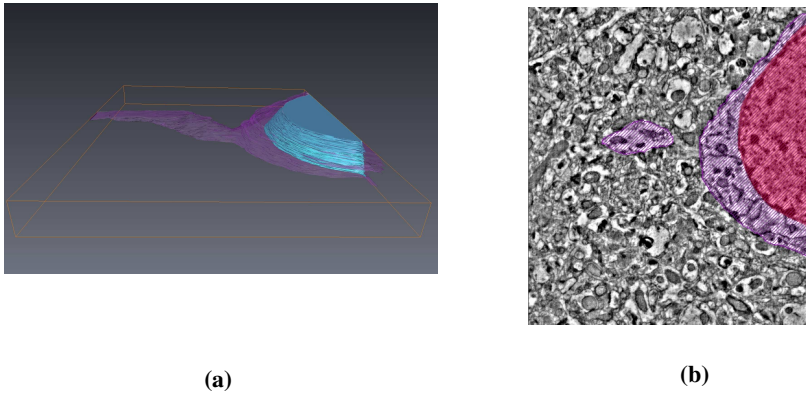
Figure 5.12: (a): A 3D reconstruction showing the protruding dendrite from the cell body. The cell (purpule) has been rendered transparent to allow the visualization of the inner nuclus (turquoise). The orange cuboid is the dimensions of the stack used for the model construction. (b): Slice number 34 used in the creation of the model in **Fig. 5.12a**. The cell body and the dendrite is labeled purpule, the nucleus is labeled red.

(a)

(b)
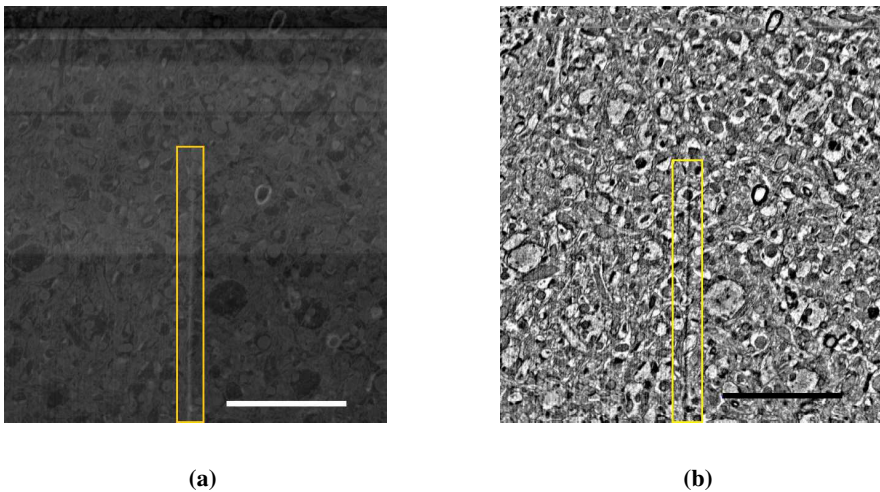
Figure 5.13: (a): raw data, (b): processed micrograph. The image processing may profoundly increase the tracing potential of the raw data. But processing flawed data can only improve the result to a certain extent; the curtaining (yellow rectangle) from (a) is till present in (b). The curtaining problem of connection of contrast is seen in (b). The example is extracted form the $60nm$ slice thickness stack of **Fig. 5.11e**. Scale bar: $(a, b) = (5\mu m)$.

The DAB staining protocol caused the characteristic morphology of the interneurons is shown in a TEM micrograph in **Fig. 2.3** and SEM in **Fig. 5.6**. The original is seen on the left, and the same micrograph with representative interneurons labeled on the right. This morphology and the increased brightness were used to trace the interneurons through the stacks in the 3D reconstruction. After collecting the stack of 120 sequential micrographs a subset of images was selected, 9 of which are shown in **Fig. 5.14**. The stack was inverted, aligned using the Stackreg plugin in Fiji, and further processed by a Fast Fourier Transform Bandpass Filter as further described in **Sec. 4.3.1**.

Then the stack was further processed in $Avizo\ Fire$ 7.1, filtering the images through a median smoothening filter, before reconstructing the volume as shown in **Fig. 5.15a**. The axons and interneurons were labeled in each slice by using the 'Magic Wand' and 'Blow tool', respectively. This led to the reconstructions shown in **Fig. 5.15b** and **Fig. 5.15c**.
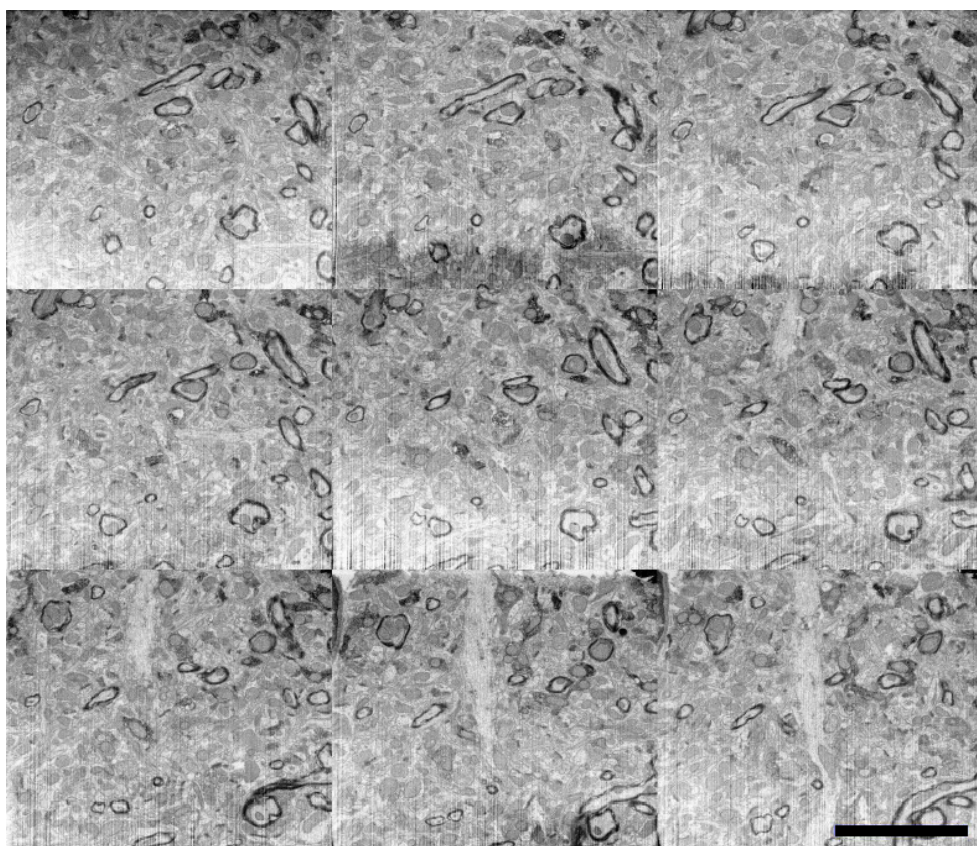
Figure 5.14: 9 micrographs each separatied by 10 slices from the image stack used in the creation of the 3D model shown in **Fig. 5.2**. The slice thickness in this Slice and View was $20nm$, leading to each image being separated by $200nm$. The images have been inverted. Scale bar bottom right: $5\mu m$.

(a)

(b)

(c)
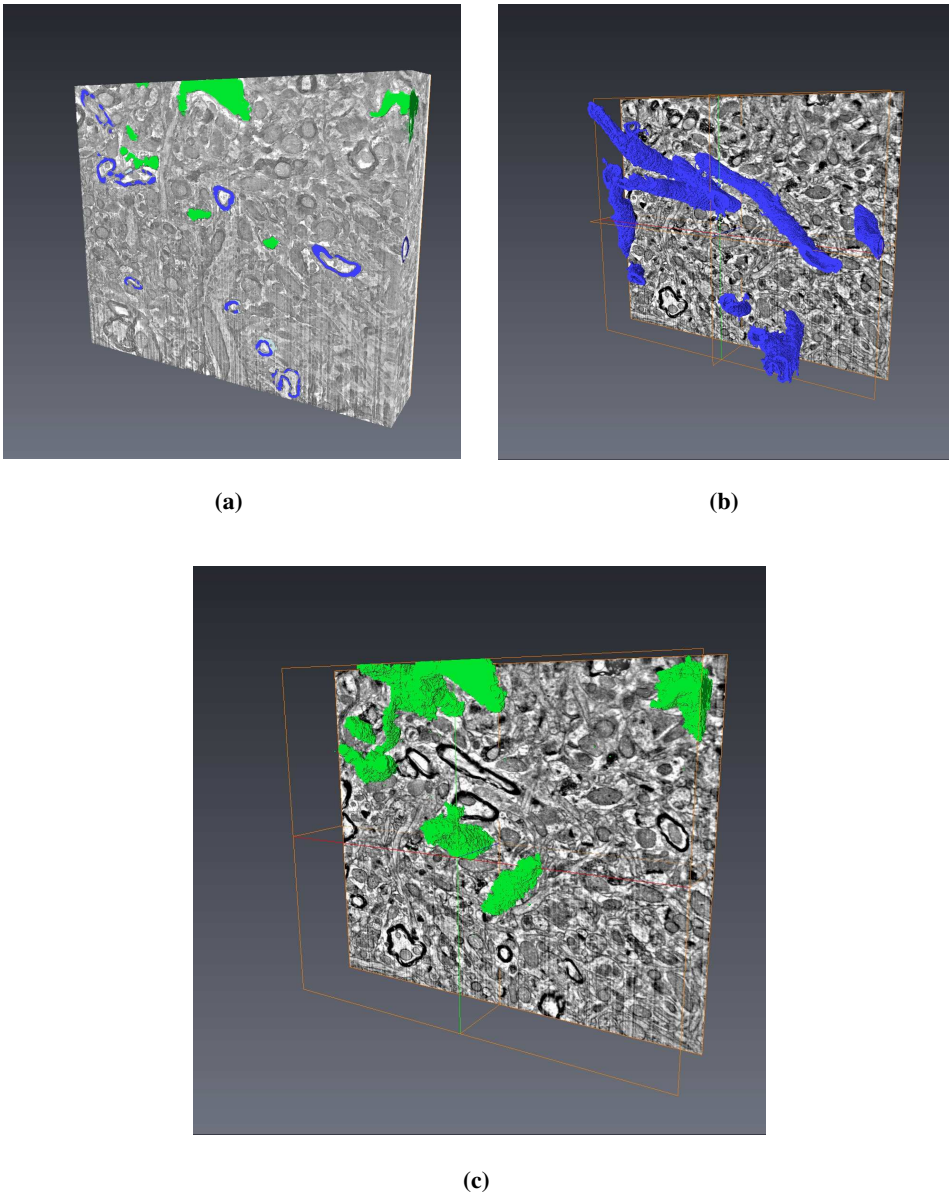
Figure 5.15: (a): The entire stack of micrographs reconstructed using Avizo Fire 7.1, the entities labeled blue are axons, green are interneurons. (b): reconstructed axons isolated from the stack. (c): reconstruted interneurons.

5.3 EDX

Principle of EDX search

The electron beam can also be used to excite X-rays from the sample. Since X-rays originate from a relatively lower part of the interaction volume (**Fig. 3.3a**), the excitation of characteristic X-rays from within a sample volume may shed light on what cannot be seen with SEs or BSEs. Further details are noted in **Sec. 3.3**.

The idea for searching with EDX is shown in **Fig. 5.16**. By segregating the surface of the FIB block into a matrix and collecting EDX intensity scans of each cell, an analysis of the intensity scans may find the cells with volumes of interest.
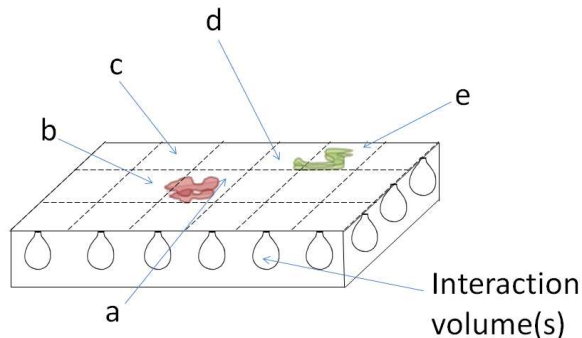
Figure 5.16: A schematic of the idea for the tracing with EDX. The block is segregated into a matrix, the letters a-e indicate different cells, and the coloured entites beneath the surface has an increased density of a traceable element. If EDX scans (with interaction volumes suited the depth of interest) had been performed of all the cells, a comparison of the intensities could reveal which of them are interesting to investigate further.

Assuming that each EDX field of view covers each matrix cell, and if the red entity contains a high density of a certain traceable element, an EDX scan of region a will contain a higher intensity (number of counts) of that element then any other cell (**Fig. 3.11**); a scan of region b will show the elements presence. The same would be true for the green object, which would signify region e of highest intensity. Therefore, an intensity scan could be

used to decrease the area of interest where the operator would have to search. The information revealed with the FIB/SEM Slice and View is very complete for the volume of the investigaion conducted, but the volume is limited (**Fig. 5.17**).
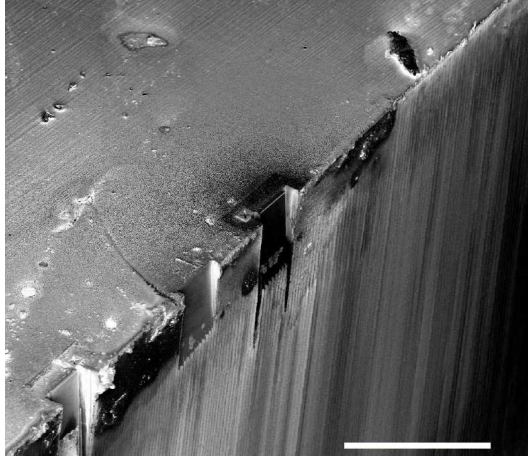
Figure 5.17: If the volume is not homogeneous for the entity of interest for the Slice and View, the searcing with the FIB/SEM can be very time-consuming. Shown in the figure is a very small part of a sample under investigation, and marks form Slice and View protocols conducted (reference 'X'). Scale bar: $100\mu m$.

Thus if the element symbolized by red was due to labeling of an entity of interest (either directly of indirectly), region a is the cell to investigate further. Having selected the cell, an EDX dot map (indicating the spatial location of the excited x-ray peak of interest) of the cell could be collected to further narrow down the area. From the dot map, the SEM magnification could be increased which decreases the surface area under investigation, and when a certain threshold was met, one could start to FIB mill the block and investigate the exposed surface.

Practical application

The DAB staining protocol used in the sample preparation in this Thesis (**Sec. 4.2**) can be intensified with a silver intensification and gold substitution. By such an intensification, an

EDX search for gold might be used to narrow down the regions. The location (dependent on the density) might be shown with a sample tilt of $0°$, but locating the gold after a FIB Rough cut may also be of value.

The use of the electron beam to excite X-rays permit non-destructive investigation of internal structures of samples, and X-ray microtomography permits quantitative measurements of the data, e.g. elemental spatial distribution [30]. This is because the X-ray signal originates from deeper within the interaction volume (**Fig. 3.1**). Thus exciting X-rays from within the volume may shed light on what it contains if entities of interest are labeled with traceable elements.

EDX was investigated for preliminary mapping purposes. This includes an investigation of locating elements as caused by their characterisitc X-rays, investigations of how the acceleration voltage (beam energy) influence the resolution of the measurements, the generation of a model specimen, measurements of the tracing capabilities of deposited layers on the model, and the use of gold/silver intensification of embedded brain tissue.

Characteristic X-rays

Knowing the elements present in a sample, allowed for the investigation of the excitation of known characterisitc X-rays. By using a gold sputtered Epon epoxy sample, the excitation of characterisitc X-rays of gold, carbon and oxygen was tested. The results are shown in **Fig. 5.18**. As is seen in the figure, the characteristic X-ray of the three elements quickly rise far above the background braking radiation (**Sec. 3.3**). The peaks identified in **Fig 5.18** were used further for the selective wavelength collection in the dot maps.

Elemental dot maps

The EDX spectrum in **Fig. 5.18** was used for the collection of an elemental dot maps of the surface. Dot maps are made by using a collected spectrum to select certain peak wavelengths and label them according to the element it represents (**Sec. 3.3**). By performing an
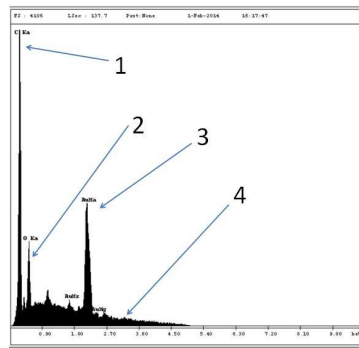
Figure 5.18: The EDX spectrum with the characteristic peaks identifying the elements present. The numbers represent: $1 : C$, $2 : O$, $3 : Au$ and 4 identify the braking radiation.

additional EDX scan, the spatial location of the element can be determined. The collected maps showed as expected a homogeneous dispersion of the elements (**Fig. 5.19**). The voltage used was $5kV$, this only excites these elements, depite the presence of Osmium and Uranium in the block.
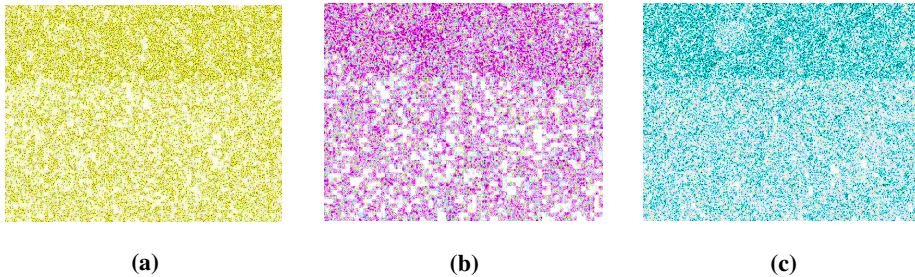
Figure 5.19: Three elemental maps used to verify the known elements by EDX. All images have been inverted and contrast enhanced. The respective maps identify: (a):gold, (b): oxygen, and (c): carbon. The sharp line indicates the boundary where the SEM scan was aborted.

Ga implantation was also investigated after a Slice an View by EDX. Gallium ions may be implated when milling each slice, and also when using the GIS for metal deposition. An EDX spectrum and elemental maps were collected of an area after a Slice and View. Following the collection of an EDX spectrum, the wavelengths of Pt and Ga were selected and the elemental maps are seen in **Fig. 5.20**. The results show that Gallium ions were implanted during these investigations, and possibly with increased frequency due to

increasing current (the Slice and View current was $0.9nA$, the trench milling was $6.45nA$). But this is also related to the topography, the Pt driftcorrection layer was deposited using $0.26pA$.

(a)

(b)

(c)
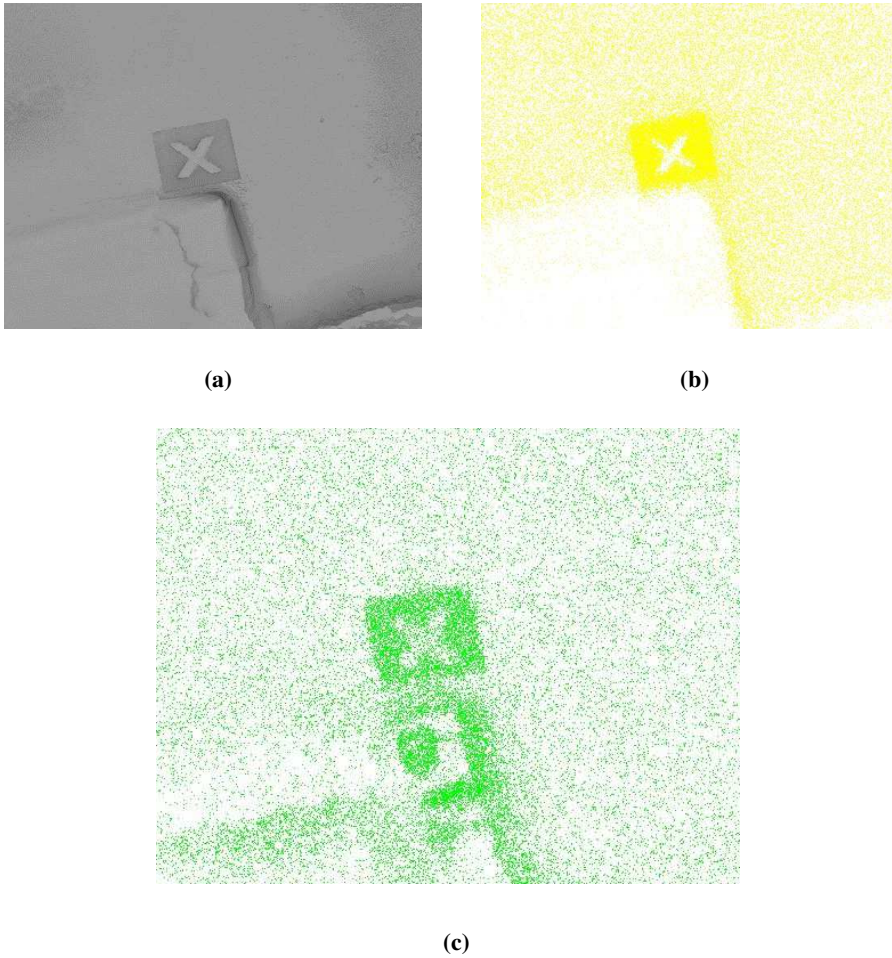
Figure 5.20: (a): SE micrograph of the area post a $S\&V$; (b): Pt elemental map, high Pt density in the deposited driftcorrection layer; (c): Ga elemental map, high ion implantation (**Sec 3.2**) density where the GIS precursor dissociation occurs, and where the $S\&V$ trenches were made. All images are inverted and contrast enhanced.

5.3.1 Model specimen

Investigations were performed using EDX and Pt deposition on a model specimen for preliminary mapping of regions of interest. Since elemental maps can be collected and specimen composition implicated([32]), the applicability of using EDX to locate the ROI may be valuable. The search for relevant ROIs using the FIB/SEM in electron opaque plastic embedded blocks may be extremely time consuming if the density of entities of interest is sparse [57]. Therefore, a model was created by depositing layers of Pt and investigating the block by EDX. The model and further details of its preparation is seen in **Fig. 4.3** and desribed in **Sec. 4.2**.

Model preparation

For the deposition of metal on the sample, the GIS system was used (**Sec. 3.2**). The gas Injection neddle of the system requires the sample to be oriented such that the ion beam strikes the sample vertically. This deposits the metal 'on top' of the sample. The model with the three layers of deposited Pt is seen in **Fig. 5.21a**. With this sample orientation voltage/resolution measurements were conducted as noted in **Sec. 5.3.1**.

When the layers had been deposited, the sample was reoriented for the tracing experiments. The sample orientation is seen in **Fig. 5.21b**. The dimensions of the Pt layers and and ion beam currents used resulted in the following ion current densities for the layers: $1.3pA/\mu m^2$, $2.2pA/\mu m^2$ and $4.5pA/\mu m^2$. The deposition result seen in **Fig. 5.21a** shows a predominant sputtering when using a FIB current of $0.9nA$ ($4.5pA/\mu m^2$), despite the 'rule of thumb' when depositing Pt in with FIB is $5 - 10pA/\mu m^2$ [3]. This may be because of the highly asymmetric shape of the area of metal-deposition.

Elemental maps, varying voltage

To test the influence of the accleration voltage on the quality of the elemental maps, dot maps were collected at varying voltages. The voltages tested were: $5kV$, $10kV$ and $15kV$.

<p align="center">(a)   (b)</p>
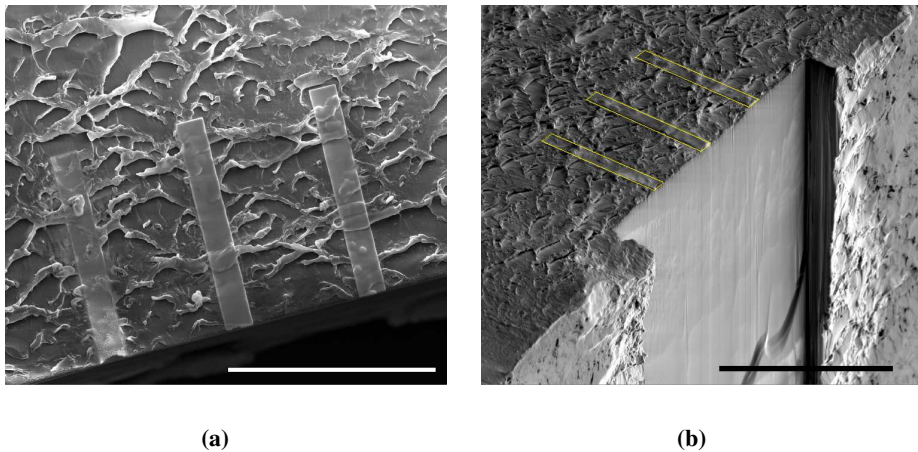
Figure 5.21: (a): the deposited layers of Pt on top of the Epon block; (b): the reoriented model in **Fig. 4.3b**, placed such that the tilt creates an interaction volume able to trace an EDX signal. Yellow lines are drawn to increase the visibility. Scale bars: $(a, b) = (40 \mu m, 50 \mu m)$

The result of the experiments are is seen in **Fig. 5.22**.

From the results, an increase in resolution with increasing acceleration voltage can be seen. This may be coupled to the interaction volume (**Sec. 3.1**), as an increase in the voltage leads to an increase in the depth of the volume. If the electrons does not strike the element 'on top', the probablity form them to backscatter from within the bulk and excite characteristic X-rays on the way back diminish.

(a)

(b)

(c)
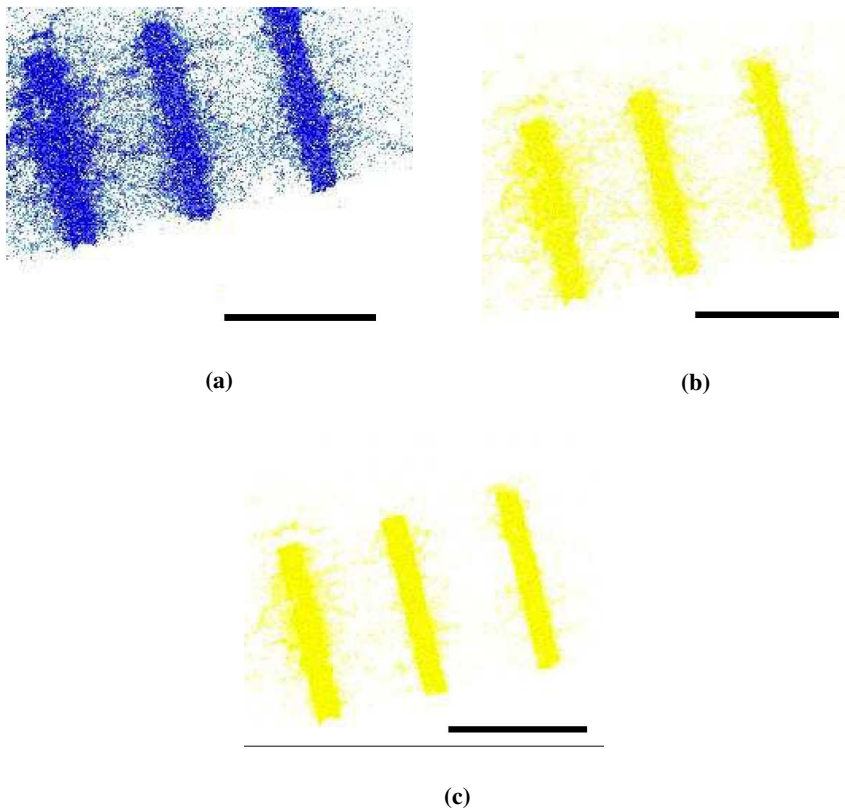
Figure 5.22: The three layers imaged with varying voltage with EDX: (a): $5kV$, (b): $10kV$, (c): $15kV$. All images have been inverted and contrast enhanced. Scale bars: $(a, b, c) = (30\mu m)$.

5.3.2   Elemental tracing using EDX

For the tracing experiments, the generated model was used and EDX tracing experiments were performed with the sample orientations I,II and III as seen in **Fig. 5.23**. Orientation I was used both to collect an EDX spectrum which could be used to define the elements to be traced, and later to see that the selected peak wavelengths gave the expected result. Details of the protocol used for the tracing estimations is noted in **Sec. 4.4.4**.
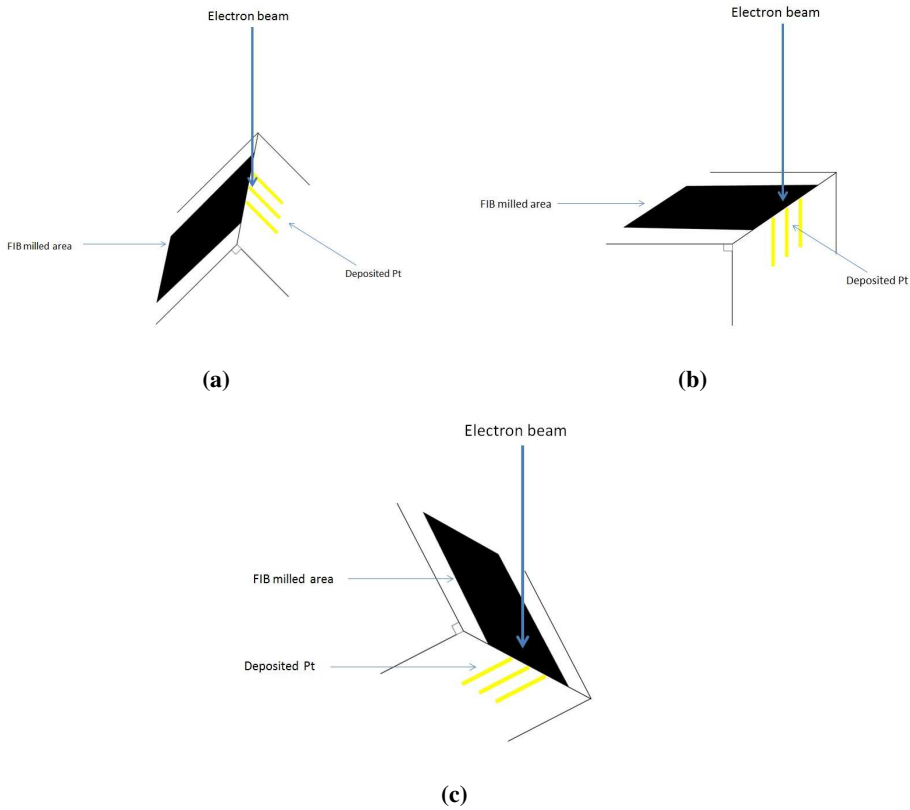
Figure 5.23: The three orientations used for the investigations of the EDX tracing-potential. The orientations in (a, b, c) are called (I, II, III), respectively.

Voltage dependent tracing of elements

Further experiments of the acceleration voltages used for tracing the elements were performed, this time tracing the elements through Epon. The sample orientation used for these investigations was III (**Fig. 5.23**). The area used in the investigations can be seen in a SE micrograph in **Fig. 5.24a**. On the sides of the FIB milled surfaces, gold had been deposited for earlier experiments using the same block. The experiment was also a test investigate the similarity of the Pt and Au wavelengths, and therefore for using Pt to model Au.

From the results seen in **Fig. 5.24**, the highest voltage $(30kV)$ should be used to trace Pt

for both the maximum signal and length. For the comparison of tracing gold and tracing platinum, the result seen in **Fig. 5.25** shows that the wavelengths are so similar that gold is 'mistaken' for platinum and vice versa. Therfore, the use of Pt to model Au for EDX investigations was verified, and the importance of not sputtering the sample block with Au (charge reduction) when searching for Pt is highlighted. As noted in **Sec. 4.2** Cr was used for the charge reduction on the EDX model.

(a)

(b)

(c)

(d)
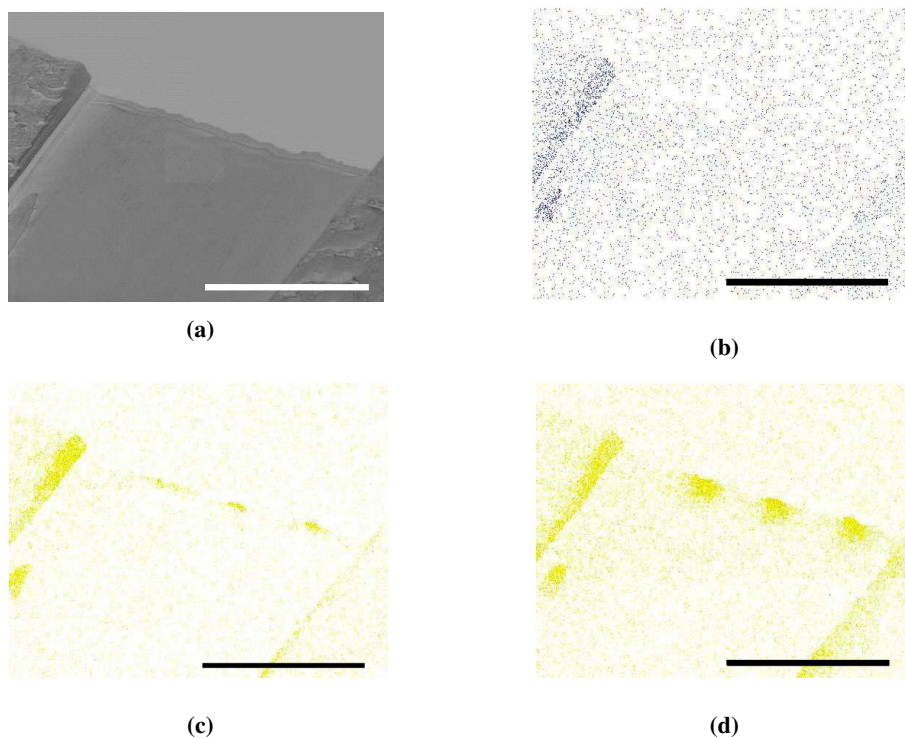
Figure 5.24: (a): A SE SEM of the area used for the investigations. The sample orientation used was III (**Fig. 5.23**). EDX images are taken with the voltages: (b):$5kV$, (c):$15kV$ and (d):$30kV$. All images have been inverted and contrast enhanced. Scale bars: $(a, b, c, d) = (50\mu m)$.

(a) **(b)**
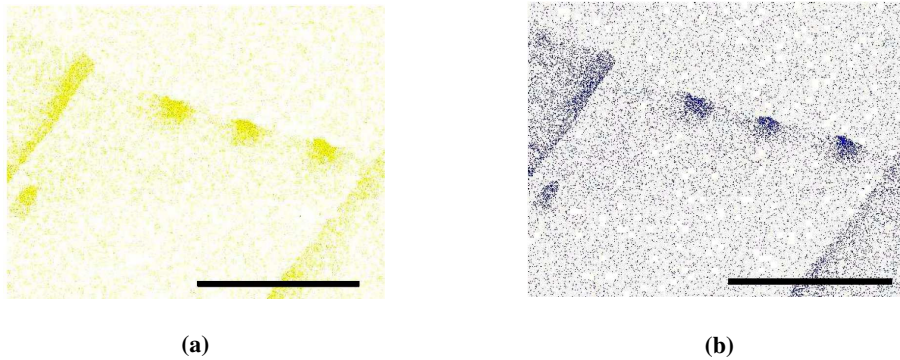
Figure 5.25: The elemental maps when tracing gold and platinum show a high degree of similarity. The orientation used was III (**Fig. 5.23**).(a): Pt tracing and (b): Au tracing. Scale bars: $(a, b) = (50 \mu m)$.

Superimposed elemental maps

A preliminary map would be of highest value if the spatial elemental distribution could be located and the regions narrowed down using orientation II in **Fig. 5.23**. This would allow the operator to immediately be able to locate the regions of interest with minor post-processing of the data. Also, superimposing the distribution an a SE mirograph would allow an orientation of the stage accoriding to the element of interest. Therefore, investiations were conducted to see the clarity of the distribution from the 'top view', $0°$ tilt.

The SE micrograph, the corresponding EDX elemental map and the superimposed image is seen in **Fig. 5.26**. From the processed superimposed image, the potential for stage-orientation and FIB milling in accordance to elemental distribution can be seen. This is because topographic features can be seen in both the superimposed image, and in the instrument 'Live view'.

Length estimation of elemental tracing

The final EDX model tracing experiments were performed to see how far the Pt EDX signal could be traced. This was conducted with the stage orientation III in **Fig. 5.23**.

(a)

(b)

(c)
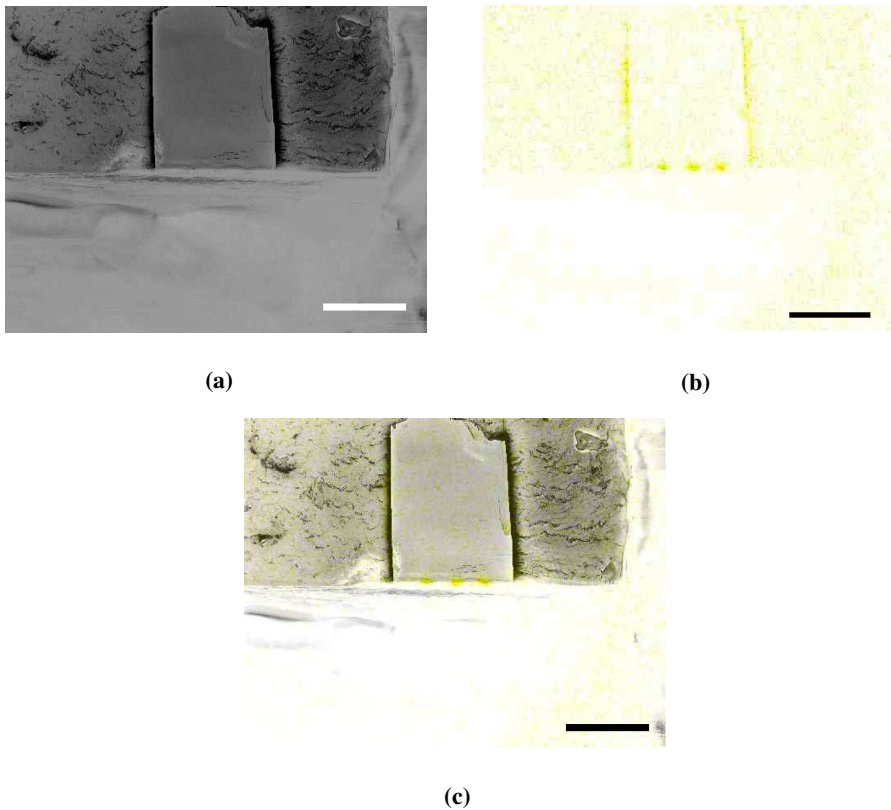
Figure 5.26: The sample orientation used was II (**Fig. 5.23**). (a): SE SEM showing the area investigated; (b): the corresponding area showing where the increased density of Pt is located; (c): a processed superimposed image. Scale bars: $(a, b, c) = (50 \mu m)$.

With this orientation, the electron beam interaction volume excites the Pt characteristic wavelengths with a strength (also) as a funciton of the distance through Epon. Further details of the tracing estimations are noted in **Sec. 4.4.4**. The results show that with the parameters found through the investigations, the gradient caused by the Pt could easily be traced a length of $17 \mu m$. The estimation was done by use of visual inspection of the gradient of the color representing the metal and **Eq 4.3**. This shows the potential of using EDX to trace selected entities in bulk through embedding resign.

(a)

(b)

(c)
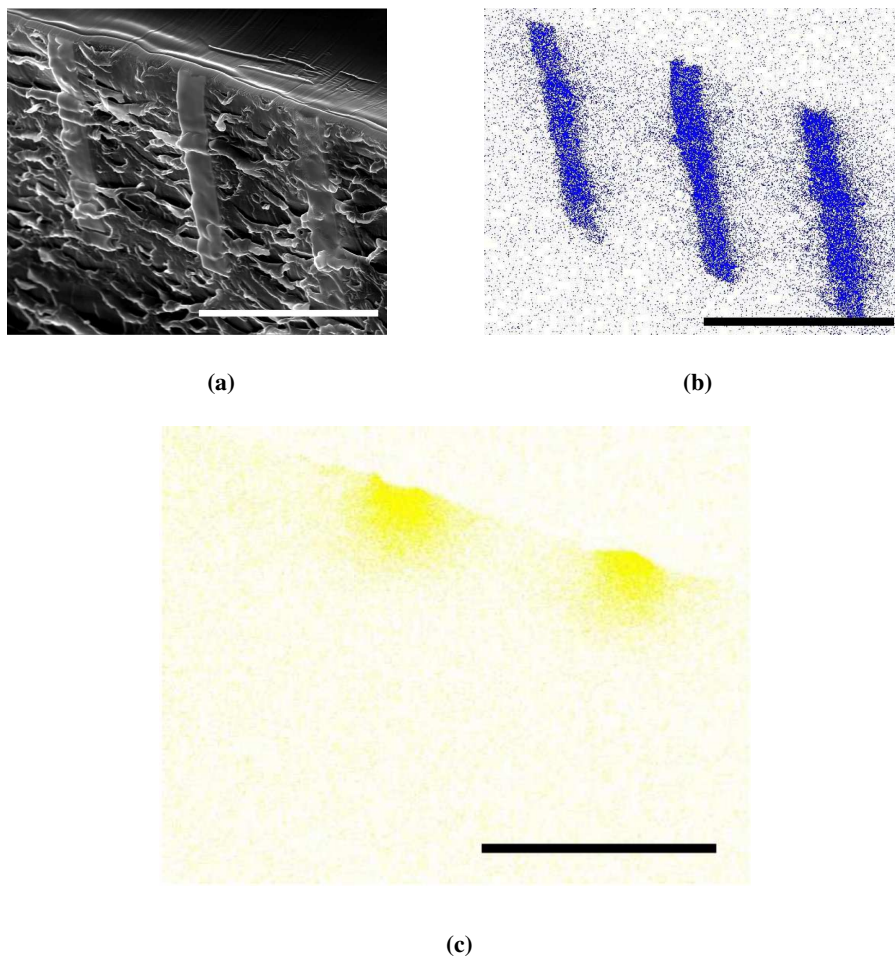
Figure 5.27: The sample orientations used are noted in the parantheses. (a): the three deposited Pt layers, (I). (b): Elemental map of Pt labeled blue, the image has been inverted and contrast enhanced (I). (c): the result used to see how far the EDX signal could be traced through empty Epon, (III). Scale bars: $(a, b, c) = (30\mu m, 30\mu m, 20\mu m)$.

5.3.3 EDX of samples labeled with DAB and gold

To test the tracing principle, a doubly labeled sample was prepared. This sample had been both DAB stained and gold intensified (**Sec. 4.2**). This was tested to investigate if EDX could be used to locate the doubly labeled entities. As the labeled cells have an increased amount of gold present on the surface, a gold gradient might be used to implicate their location.

A light microscope micrograph is shown in **Fig. 5.28a**, which shows the cells to be found. Three cells are enclosed in the left rectangle. But concerning the results, the EDX elemental map of the top surface showed no indication of intensity differences **Fig. 5.29c**.

(a)

(b)
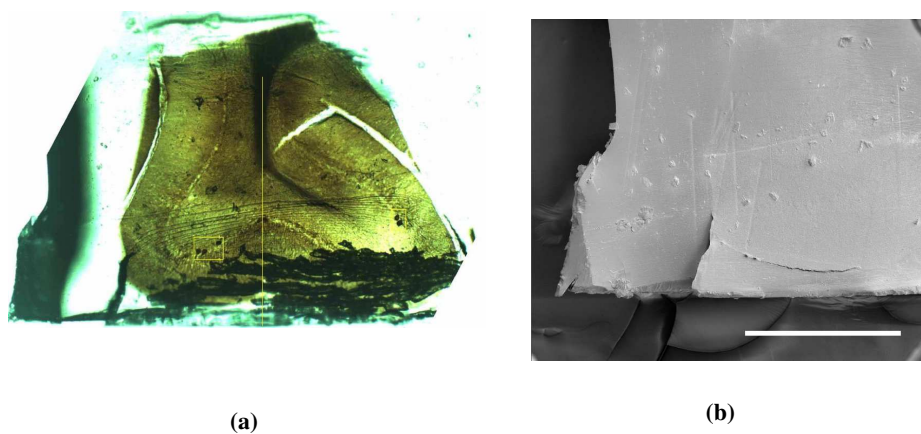
Figure 5.28: (a): a light micrograph of the sample stained with DAB and gold. The yellow line indicates the manual scalpel cut made in a later investigation. (b): a SEM with the same orientation, a feature resulting from the ultramicrotome cut can be seen in the bottom left corner of both images. Scale bar: $500 \mu m$.

For investigating other parts of the sample, a manual cut with a scalpel was conducted. This was done relative the ultramicrotome feature seen in the images above, the direction of the cross-section cut is seen in **Fig. 5.28a**. A new layer of $40 nm$ of Cr was deposited.

From the newly exposed surface, a region was further FIB milled to make the surface flat. The new cross-section with the FIB prepared region is indicated in **Fig. 5.29a**, and a SE

of the surface (with EDX parameters) is seen in **Fig. 5.29b**. The resulting elemental map collected is seen in (**Fig. 5.29d**). The results show that the distribution was homogeneous also in this part of the sample.

(a)

(b)

(c)

(d)
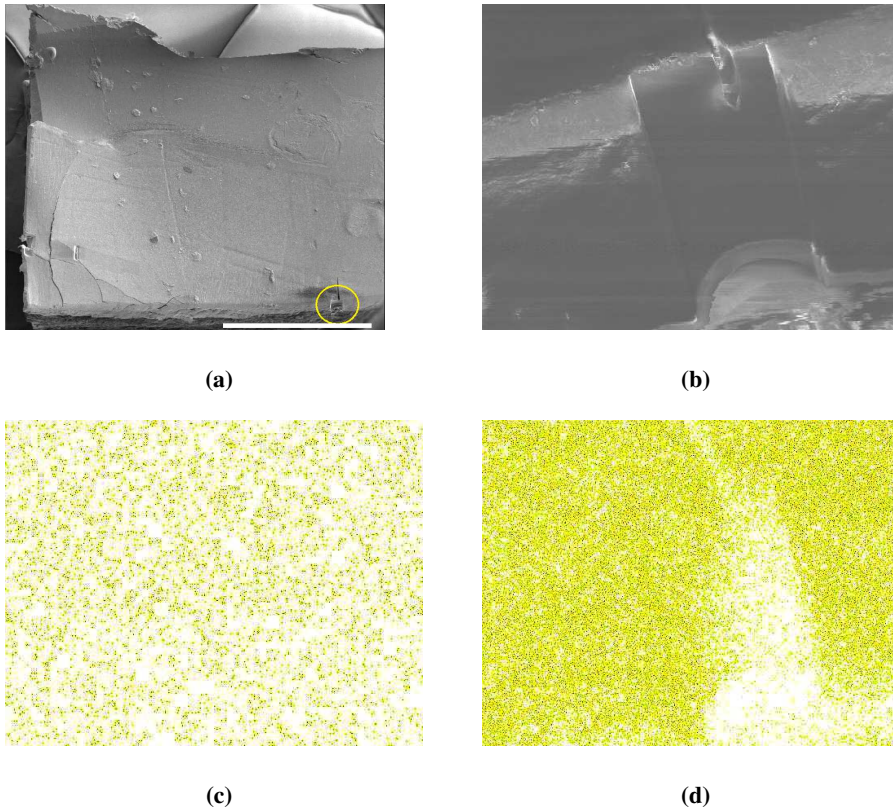
Figure 5.29: (a): the sample was cut with a scalpel to expose a new large surface to further investigate, the location selected is indicated. (b): a SE image of the region FIB milled after the scalpel cut. (c): the gold elemental distribution in the sample top surface (**Fig. 5.28a**). (d): the gold elemental distribution of the FIB milled area in (**Fig. 5.29b**). (c) and (d) have been inverted and contrast enhanced.

Chapter 6

Discussion

Trench milling

The purpose of conducting the trench milling experiments was to investigate how the ion current influenced the milling accuracy. Decreasing the ion current leads to the sputtering of a selected volume taking more time. Also of interest was how the diameter varied with distance, as a decrease in accuracy with distance may lead to developing of curtaining.

From the results the diameter of the trench shows a clear dependence on the ion current used. The suspected decrease in accuracy with current indicated in **Fig. 5.1b** was shown in the results. And interestingly the diameter of the trenches showed that there was a threshold for which a futher decrease in ion current did not improve the milling noteworthy. This current was $0.9nA$. The graph in **Fig. 5.3** indicates that the use of a current of $0.9nA$ and an acceleration voltage of $30kV$ provides a good accuracy. Importantly, this current also led to the trench diameter being very consistent. The trench diameter did increase when the ion beam started milling the Epon epoxy relative the metal. This may be coupled to scattering effects of the ions (**Fig. 5.5c**). As see in **Fig. 3.9b** with increasing depth, the scattering of ions increases. In addition the altered crystal structure of the sample might possibly have influenced the trench thickness. Despite the metal on the top being

amorphous (randomized GIS deposition), the strength of the sample is harder than Epon epoxy. Another aspect is the electrical properties of Epon epoxy. This might lead to charge effects with implanted ions. This will influence the ion probe size, and therefore the trench diameter.

Decreasing the acceleration voltage has been used to increase accuracy of ion milling, measured by sidewall damage [88]. But sidewall damage was not of concern in this investigation. Steps were taken to avoid edge effects (milling trenches, always milling surfaces larger than the ROI). And reducing the acceleration voltage (decreasing the beam energy) would again lead to time having to be increased for milling a volume, as this decreases the beam energy. Decreasing the voltage also influences the porbe size and makes it bigger. One would therefore have to decrease the current further for the porbe size to be sufficiently small. And, since the use of lower voltages requires that the ion column is aligned accordingly, this was not investigated further. It was seen that decreasing the voltage led to neither accurate nor consistent milling, as judged by the trench result **Fig. 5.4b**. The expected decrease in accuracy is also described in **Sec. 3.2**.

Further Progress

If the ion beam accuracy is to be investigated further, a decrease in acceleration voltage might be investigated. This may decrease the efficiency of the protocol, but may also be used to adjust the milling time to a similar scale as the SEM collection time for less conductive samples.

Brain tissue investigations

In the brain tissue investigations, different aspects of the the Slice and View protocol and resuts processing was investigated. Two embedding protocols were investigated, different slice thicknesses were tested (larger volumes each Slice and View), and the data collected from the protocols were used in analysis and reconstruction of the volumes. Judging from the image stacks collected and the 3D models constructed, the protocols used in their

collection and creation work very well. The data processing also avoided the problem of brightness gradients (top to bottom, decreasing signal with depth [14]) even though this was observed during some of the experiments.

Despite additional time required for re-embedding the samples, the candidate would argue that this is conducted. This lead to the quality of the micrograph improving significantly. This is related to the geometry of the sample (**Fig. 4.19**), and is further supported by the trench milling experiments (varying trench diameter, difference in material composition). Using thin samples requires ion milling to a larger depth to uncover the ROI. Re-embedding the samples avoided most of the problems and led to high quality data.

Furthermore, use of thin sections also created the problem where crystals could form above the ROI (**Fig. 5.9a**). The difference in structure will influence the energy required for the ion beam for the mill. This might have caused the development of curtaining beneath the crystals. By re-embedding the tissue, the boundary was removed by the ultramicrotoming as was any problematic crytallization. So the extra processing steps are of high values for the FIB/SEM investigation.

Even though image drift was not a large problem for the experiments conducted, even less drift might have been achieved by -in addition to the 12h prevacuuming, let the sample obtain both thermal and mechanical euilibrium in the position to conduct the Slice and View. This can be done by finalizing the adjustments and parameters and leave the instrument for $1h$ [16].

For the slice thickness investigations, the quality of the micrographs were judged by the curtaining. It was found that the curtaining did not propagate when using a thickness of $60nm$ (**Fig. 5.15**). This is a common problem for Slice and View. This might be related to the accuracy through mill. Having selected an area (volume) for ion milling, the accuracy of the mill increases towards the end. Thus, when the volume to be milled is large, this might lead to the two issues 'canceling each other'. For a polished surface on a re-embedded sample, curtaining was not normally a problem. It was also found that using a slice thickness of $40nm$, the curtaining were as absent as when using $20nm$. Thus, these ion beam parameters are applicable for a thickness of $40nm$, if larger volumes (with

decreased z-resolution) is to be investigated.

The use of DAB staining did make the labeled interneurons easily identifiable. But, the tissue was difficult to reconstruct, such that optional ways to label the tissue might be investigated. By using a silver/gold double labeling protocol the increased contrast might be usable for the contrast tracing. Another important point is that the silver/gold intensification process may be repeated. Labeling with siver, enhancing with gold, then repeating the process, as the agrophylic capabilities of the HRP is conserved (**Sec. 3.4**). This would potentially create an even stronger (and thicker) contrast/boundary. This might be beneficial in the 3D reconstructions, as this would create easily traceable outer boundaries.

In regards to use the FIB/SEM for 3D reconstructions of brain tissue using high magnifications, the DAB staining might not be the optimum choice, at least not for protocols followed in this Thesis. This is caused by the disruption of the ultrastructure of the entities that are labeled [35]. Even though easily identifiable, the candidate experienced the contours being very hard to track. This made it impossible to use more convenient tools for the reconstruction, e.g. the 'Magic Wand', and manual tracing of each slice became the only option. This removes the potential for semi-automatic tracing used in the axon tracing experiments, if not a good template maching procedure is developed.

The staining with Osmium, Uranium and the DAB protocol might have been the reason for the avoidance of the charging artifact. The SEM parameters uses a very high dwell time, which can easily charge insulating specimen. Since the gold intensified tissue was not stained with Uranyl acetate and had a different composition, this might have lead the agglomeration of excess negatve charge (**Fig. 4.21**). The high conductivity of the interneuron tissue might have removed the charging, despite the parameters implying that the rule of thumb to avoid charging is that the imaging time and milling time are approximately similar [3]. In these investigation they were separated by more than an order of magnitude.

Concerning the SFB/SEM vs FIB/SEM comparison ([27]), the researchers used a resolution of $(x, y, z) = (26nm, 26nm, 50nm)$, and used computerized reconstructions of axons of stacks of 100 and 700 slices. Their approach first used a denoising step of the slices -of 20min/slice- and thereafter computed structure tensors which took $10min$ for

the whole stack. With the protocol followed in this Thesis, the examples given in **Fig. 5.11a, 5.11c, 5.11e** were processed through FIJI and Avizo Fire. Having processed the stack and imported it into Avizo Fire, the 'Magic Wand' tool was used, and the threshold corrected once for each selected axon. The whole process for creating the models was done in a couple of minutes. But even though the FIJI processing was done equally quick on a laptop computer, the Avizo Fire model generation was done on a supercomputer. [27] was published in 2009.

The required resolution for the tracing of the thinnest axons in the model experiment was set to $50nm$ [27, 102]. The measured reciprocal units in both the processed and unprocessed tables **Tab. 5.1** and **5.2**, implies that this approach may have similar applicability as the SBF/SEM protocol. Even though SBF/SEM might be better suited for moderately sized volumes and FIB/SEM for very highly resolved small volumes ([10]), the slice thickness and the ion beam current can be investigated for the collection of adequately highly resolved stacks of images. The results of the preliminary experiments provided a sufficient resolution for 100 sequential slices, leading to the FIB/SEM approach may be used for mapping larger distance axons. The thickness used in the comparing article was $50nm$, the semi-automated FIB/SEM approach traced axons with a slice thickness of $60nm$.

Further Progress

As can be seen from the axon tracing experiments, the use of a slice thickness' of $40nm$ and $60nm$ both showed applicability in regards to automatic axon tracing. What might also be proposed when comparing **Fig. 5.11c** with **Fig. 5.11e** with the respective dimensions stated, is the role the difference in resolution when obtaining the images may play. The $40nm$ images were obtained with a resolution of 1024×884, the $60nm$ stack with 2048×1768. The model with $40nm$ does appear more fragmented. Another option is differences in the SEM focus or drifting leading to the contrasts being disrupted to such an extent that the contrast enhancement does not 'close the gap' when adjusting the thresholds. This can also be investigated, as the decrease in resolution with the optimized SEM parameters effectively reduces the time of the experiment with 50%. Finding the resolu-

tion required for resolving the entities to be traced is something the candidate proposes should be investigated in advance of conducting further experiments. (Another secret to success has been stated to keep the imagin below 2 min [33].) The optimized SEM parameters does yield very highly resolved images, but is a 'bottleneck' in the experimental protocol.

The semi-automatic tracing predisposes that the contours are similar. This is increased by processing the stack with the same FFT bandpass parameters. Furthermore, for an increased tracing accuracy 'stronger' FFT parameters could be used to filter away more frequencies. If general morphology were to be traced, one could investigate the FFT parameters that accurately maintained the details of interest, while filtering away noise and interferring entities in the micrographs. In semi-automatic tracing, the developing of curtaining is very important. This is because curtains can 'connect contrasts', as evident when looking at the example in **Fig. 4.20**. When tracing an object through a volume, if a curtain intersects the object to be labeled in a single slice constituting the volume, this may cause the labeling of everything else the same curtain intersects.

The strong contrast of the densely labeled axons made it easy to select the axon to be traced. Furthermore, if the research object was axon tracing, one option could be to use tissue not labeled through the DAB protocol, and only labeling with Osmium and Uranium. This could also have made the axon tracing results more accurate. The axons were selected as they were 'isolated' form the remained of the densely labeled entities. Another option could be to test the automatic tracing protocol for tracing selectively labeled entities by the DAB staining and silver/gold enhancement, and not staining the axons with Osmium and Uranium. By using multiple double labeling of an entity of high density, this might contribute to the volume both being sufficiently conductive, and that the boundaries would be sufficiently thick such that the boundaries could be traced.

EDX

The EDX investigations were conducted to see if this can be used as a way of preliminary mapping the FIB block to be investgated. The idea can be condensed to if the entities to be investigated are selectively labeled with traceable elements, a preliminary EDX map of the tissue might narrow down the area to investigate.

The voltage dependency was investigated and it was found that the highest voltage was the voltage that provided the highest resolution. But with that voltage, a larger amount of characteristic elements are excited. Such that one has to weigh the depth of the interaction volume and resolution, against exciting possible noise of heavier elements. Another note to take into account is that the tracing length will depend on the charcterteristic wavelength excited. FIB-EDX tomographical reconstructions have been performed on resign embedded biological specimen, which concluded that the use of $5kV$ was the maximum voltage to be used with acceptable resolution [58]. But, since the use of EDX in this regard is for mapping purposes, the candidate proposes that the highest voltage ($30kV$) is used.

The superimposed image of the elemental map and the SE image (**Fig. 5.26**) did show the poteintial for EDX preliminary mapping, as shown in **Fig. 5.16**. Despite the main disadvantage of investigating bulk specimen is the low spatial resolution ([32]), for preliminary mapping of trace elements this might be beneficial. The density of Pt is clearly indicated by the yellow color, and had one segregated the block into a matrix and performed similar intensity scans of the remainder, this cell would probably had the highest Pt intensity. Furthermore, the location of the Pt in the given cell would have been indicated by the yellow coloring. But what was also seen, was that the similarity in wavelength between Pt and Au might cause noise (**Fig. 5.25**). But, an option for the Au noise is that the block had earlier been coated with $40nm$ Au for another investigation. Before depositing the Pt on the block (bottom), EDX scans were conducted to see if Au was present before placing the new Pt layers; these results showed that Au was not present (data not shown).

The final tracing experiments did show that EDX could potentially be used for searching applications. EDX could trace elements through Epon epoxy for at least $17\mu m$. But the

density/amount of Pt be traced was very high; the layer used for had a thickness of $1\mu m$. The proof of principle sample investigated did not give very good results, some problems are discussed below.

The EDX ananlysis of the top surface did not reveal anything, such that a manual scalpel cut was conducted to expose a new surface. Irregular surfaces may create problems for EDX analysis ([68]) and this was experienced. Even though post-processing did flatted the surface, artifacts could be seen. And since X-ray tomography normally operates with a $1 - 10\mu m$ resolution ([8]), the homogeneous dispersion of gold in the sample could not be used for the interpretation of any concentration gradients.

The reduced hardening of the block might have been the cause for the problems with the ultramicrotoming. The results are seen in **Fig. 4.15**, where the glass knife could not be used to create smooth clear cut edges. In addition, the tissue in the block had not been extra contrasted by use of Uranyl acetate, which might have influenced the conductivity of the block. The block was coated with $40nm$ of Cr, but this was not sufficient regarding the charging. But, the silver/gold intensification should also have increased the conductivity. This procedure was not used for the other blocks investigated, and the lack of the heavy metal salt contrast enhancement makes it difficult to say anything about cause of the differences in conductivity. These questions are risen as the candidate did experience charging of the sample during the experiments (**Fig. 4.21**). It was difficult to focus properly and collect good SEM micrographs of the gold intensified sample. When collecting EDX elemental maps, this could also have been a contributing factor. In addition to the resolution of the EDX being lower, collecting elemental maps with multiple scans of the same surface would create an additional blurring effect. From the elemental maps of the doubly labeled tissue, the dispersion of gold was seemingly homogeneous, such that using EDX to pinpoint locations of higher gold density was impossible. But if this was caused by an even dispersion of gold through the tissue, or other effects due to e.g. charging is impossible to conclude.

Further Progress

It has been noted that correlative volume EM will reach its full potential when proteins of interest can be directly identified in the SEM [41], and **Fig. 5.26c** shows that superimposing EDX might be a route to investigate for reaching this potential in the future. By selective labeling with traceable elements, a superimposed image could be used directly to show the presence of the labeled entity, e.g. a medical marker.

Thus, new experiments may be conducted with new samples prepared and tested in an analogous manner to see if EDX could be used. Similar interneuron sections could be prepared, not only to see how this influenced the conductivity, but also how the double labeling influences the contrasting. As this process induces the deposition of silver, it is reasonable to suspect that the contrasts are strengthened and rendered thicker. If the object of interest is not quantitative mesurements of the interneurons (which the DAB staining also causes problems for) but 'merely' 3D reconstructions, a deposited gold layer might be easily visible in the electron micrographs. Furthermore, in the 3D reconstructions the contrasts might be more easily be traced.

A situation similar to the axon tracing could be used to test the tracing applicability of EDX. If a sample was created containing long axons (e.g. axon bundles visible with optical microscopy, high density of axons implying high density traceable element), one could stain heavily with Osmium and Uranyl acetate and test this ([27, 77]). By ultramicrotoming a very thin sheet of tissue (containing the bundle or sections of it) and re-embedding on empty epoxy, an EDX elemental map of this section could implicate the direction of the propagating axons. The optical microscope would function as a control. And by using empty Epon epoxy, the only wavelengths of interest would originate from the top layer. The Epon epoxy underneath would only excite characteristic wavelengths of C and O not interfering with the wavelengths of interest. Such a map might be used to orient the stage according to the axons. This could be used to obtain a very high magnification stack, as one knows the direction of the axonss (avoid an oblique angle like in **Fig. 5.11a**).

And, if double Au labeling of interneurons and EDX tracing proves of little value, a pre-

liminary map of axons might be useful in locating high interneuron density. Relatively short axons are characteristic for interneurons ([17]), and in the volume containing interneurons in this Thesis, the axon density was severly increased around (**Fig. 5.15b**). Thus, finding a relatively higher axon density might imply a higher density of interneurons.

The proposed experiment might avoid the two major problems for EDX which is interpretation of results under non-ideal conditions and time required to obtain a good map (4-12h) [83]. The non-ideal conditions (small peak size relative background) might not be a problem as the characteristic X-rays of C and O are not interferring with the rays of Os, U nor Au. And since the map is a preliminary map, detailed quantitative maps are of low importance.

Chapter 7

Conclusion

This Thesis have investigated aspects of the FIB/SEM protocol used for the generation of 3D models of brain tissue, and the potential for EDX for elemental tracing. The investigations revolved around how to make the Slice and View protocol most efficient, while optimizing the data quality of the experiments. The issues investigated was how the ion beam parameters influenced the accuracy of the ion milling, brain tissue preparation and the protocol used to regenerate the tissue, and different aspects of elemental tracing using EDX.

The ion beam accuracy investigations showed that the use of an acceleration voltage of $30kV$ and a current of $0.9nA$ gave the most efficient while still accurate milling. The dimensions investigated are resonable, as the samples should be prepared such as to place possible ROI as close or closer to 'the top' of the block. If ion beam accuracy is to be investigated further, a decreased acceleration voltage was not thoroughly investigated. The parameters used gave a sufficient accuracy for the dimensions of the embedded brain tissue investigated.

The brain tissue investigations showed that the extra processing step of re-embedding the sample was highly beneficial for the FIB/SEM protocol. Investigating re-embedded sam-

ples led to high quality data with the optimized SEM and FIB parameters. The high data quality made it possible to conduct 3D regeneration of the selectively labeled interneurons, and perform 3D tracing experiments of the stacks collected. The protocol did show the potential for semi-automatic tracing, if the staining was of an adequate extent. Further research questions might include how a decrease in SEM resolution may be suited for the regeneration, alternate labeling, and how the staining and data-processing may be used to create contrast thresholds for semi-automatic tracing.

The use of EDX and elemental mapping of the FIB block to be investigated did show a good potential to narrow down the areas to investigate in a stepwise fashion. Through the investigations, it was found that the use of a high excitation acceleration voltage and current of the electron beam provided an adequate tracing. EDX may be used to trace elements 'buried' $17\mu m$ in the block volume.

The ion beam accuracy investigations were accurate to $20\mu m$, the re-embedded samples created ROIs in a similar dimension, EDX tracing showed potential for tracing approximately $20\mu m$, and selective labeling with traceable elements gave identifiable morphology. Despite some problematic issues, the EDX tracing potential was revealed and might be used as a highly valuable tool. The candidate therefore proposes that the EDX tracing potential is investigated further by protocols of high similiraity as these gave good preliminary results.

Thus, FIB/SEM is an excellent approach for the 3D reconstruction of brain tissue. With FIB and SEM parameters used in this Thesis, very high quality data is obtained. The ion beam parameters gave sufficient accuracy, and the SEM quality further gave good 3D models and semi-automatic tracing options. The use of EDX, selective labeling and preliminary elemental mapping of ROIs showed a good potential in the investigations conducted and should be investigated further.

Bibliography

[1] A. Birch-Andersen, 1955. Reconstruction of the nuclear sites of salmonella ty-phimurium from electron micrographs of serial sections. Journal of General Microbiology 13 (2), 327–329.

[2] Alireza Minagar, John Ragheb, Roger E. Kelley, 2003. The edwin smith surgical papyrus: Description and analysis of the earliest case of aphasia. Journal of Medical Biography 11 (2), 114–117.

[3] Andrew J. Bushby et al., 2011. Imaging three-dimensional tissue architecture by focused ion beam scanning electron microscopy. Nature Protocols 6, 845–858.

[4] Angel Merchn-Prez et al., 2009. Counting synapses using FIB/SEM microscopy: a true revolution for ultrastructural volume reconstruction. Frontiers in Neuroanatomy 3 (18).

[5] Anil Patri et al., 2009. Energy dispersive x-ray analysis of titanium dioxide nanoparticle distribution after intravenous and subcutaneous injection in mice. Journal of Applied Toxicology 29 (8), 662–72.

[6] Ashok Veeraraghavan et al. , 2010. Increasing depth resolution of electron microscopy of neural circuits using sparse tomographic reconstruction. In: Computer Vision and Pattern Recognition (CVPR), 2010 IEEE Conference on. pp. 1767–1774.

[7] Bartelmez, G. W., Hoerr, N. L., 1933. The vestibular club endings in ameiurus. further evidence on the morphology of the synapse. The Journal of Comparative Neurology 3, 101–12.

[8] Beat Munch, Philippe Gasser, Lorenz Holzer, 2006. Fib-nanotomography of particulate systemspart ii: Particle recognition and effect of boundary truncation. Journal of the American Ceramic Society 89 (8), 2586–2595.

[9] Bodian, D., 1940. Further notes on the vertebrate synapse. The Journal of Comparative Neurology 73, 323–343.

[10] Briggman, K. L., Bock, D. D., 2012. Volume electron microscopy for neuronal circuit reconstruction. Current Opinion in Neurobiology 22 (1), 154 – 161.

[11] Bruce F. McEwen, Michael Marko, 2001. The emergence of electron tomography as an important tool for investigating cellular ultrastructure. Journal of Histochemistry & Cytochemistry 49 (5), 553–64.

[12] C. W. Oatley, 1982. The early history of the scanning electron microscope. Journal of Applied Physics 53 (2), R1–R13.

[13] Carlo Bertoni-Freddari et al., 1981. In vivo effects of vitamin e deficiency on the intracellular monovalent electrolyte concentrations in brain and liver of rat. an energy dispersive x-ray microanalytic stud. Mechanisms of Ageing and Development 16 (2), 169–80.

[14] D. A. De Winter et al., 2009. Tomography of insulating biological and geological materials using focused ion beam (fib) sectioning and low-kv bse imaging. Journal of Microscopy 233, 372–83.

[15] D J Stokes, T Vystavel, F. M., 2007. Focused ion beam (FIB) milling of electrically insulating specimens using simultaneous primary electron and ion beam irradiation. J. Phys. D: Appl. Phys. 40 (3), 874.

[16] D. Wei et al., 2012. High-resolution three-dimensional reconstruction of a whole

yeast cell using focused-ion beam scanning electron microscopy. BioTechniques 53, 41–8.

[17] DALE PURVES et al., 2004. Neuroscience-Third Edition. Sinauer.

[18] Damjana Drobne et al., 2007. Surface damage induced by fib milling and imaging of biological samples is controllable. Microscopy research and technique 70, 895–903.

[19] David Brandon, W. D. K., 2008. Microstructural Characterization of Materials, 2nd Edition. Wiley.

[20] David C. Joy, C. S. J., 1996. Low voltage scanning electron microscopy. Micron 27 (3-4), 247–263.

[21] DeFelipe, J., 2010. From the connectome to the synaptome: An epic love story. Science 330 (6008), 1198–1201.

[22] DeFelipe, Javier and Marco et al., 1999. Estimation of the number of synapses in the cerebral cortex: Methodological considerations. Cerebral Cortex 9, 722–32.

[23] Denk et al., 2011. Wiring specificity in the direction-selectivity circuit of the retina. Nature 47, 183–188.

[24] Douglas M. Tucker, Gary T. Barnes, Dev P. Chakraborty, 1991. Semiempirical model for generating tungsten target xray spectra. Medical Physics 18 (2), 211–8.

[25] Dykstra, Michael J., R. L. E., 2003. Biological Electron Microscopy; Theory, Techniques, and Troubleshooting; 2nd ed. Springer.

[26] E. G. Gray, 1959. Electron microscopy of synaptic contacts on dendrite spines of the cerebral cortex. Nature 183, 1592–1593.

[27] Elizabeth Jurrus et al., 2009. Axon tracking in serial block-face scanning electron microscopy. Medical Image Analysis 13 (1), 160–8.

[28] Elizabeth Schroeder-Reiter et al., 2009. Focused ion beam (fib) combined with high

resolution scanning electron microscopy: A promising tool for 3d analysis of chromosome architecture. Journal of Structural biology 165, 97–106.

[29] Endre Dobó et. al., 2011. New silver-gold intensification method of diaminobenzidine for double-labeling immunoelectron microscopy. Journal of Histochemistry and Cytochemistry 59 (3), 258–69.

[30] Eric N. Landisa, Denis T. Keaneb, 2010. X-ray microtomography. Materials characterization 61 (12), 1305–1316.

[31] Federico Luzzati,Aldo Fasolo, Paolo Peretto, 2011. Combining confocal laser scanning microscopy with serial section reconstruction in the study of adult neurogenesis. Frontiers in Neuroscience 5 (70).

[32] Friel, J. J., Lyman, C. E., 2006. Tutorial review: X-ray mapping in electron-beam instruments. Microscopy and Microanalysis 12, 2–25.

[33] G. Knott, Stéphanie Rosset, M. C., 2011. Focussed ion beam milling and scanning electron microscopy of brain tissue. Journal of Visualized Experiments (53), 2588.

[34] G. Knott et al., 2008. Serial section scanning electron microscopy of adult brain tissue using focused ion beam milling. The Journal of Neuroscience 28 (12), 2959–2964.

[35] G. Knott et al., 2013. Correlative in vivo 2 photon and focused ion beam scanning electron microscopy of cortical neurons. PLoS ONE 8 (2), e57405.

[36] Gerhard W. Hacker, J. G., 2002. Gold and Silver Staining: Techniques in Molecular Morphology. CRC Press.

[37] Gierak, J., Septier, A., Vieu, C., 1999. Design and realization of a very high-resolution {FIB} nanofabrication instrument. Nuclear Instruments and Methods in Physics Research Section A: Accelerators, Spectrometers, Detectors and Associated Equipment 427, 91–98.

[38] Goldstein et al., 2007. Scanning Electron Microscopy and X-Ray Microanalysis-Third Edition. Springer.

[39] Gregory J. Gage, Daryl R. Kipke, W. S., 2012. Whole animal perfusion fixation for rodents. Journal of Visualized Experiments, e3564.

[40] Günter Möbus and Beverley J. Inkson, 2007. Nanoscale tomography in materials science. Materials Today 10 (12), 18–25.

[41] Hannah E. J. Armer et al., 2009. Imaging transient blood vessel fusion events in zebrafish by correlative volume electron microscopy. PLOS One 4 (11), e7716.

[42] Hans-Ulrich Dodt et al. , 2007. Ultramicroscopy: three-dimensional visualization of neuronal networks in the whole mouse brain. Nature Methods 4 (4), 331–6.

[43] Hendrix Demers et al., 2011. Three-dimensional electron microscopy simulation with the casino monte carlo software. Scanning 33 (3), 135–146.

[44] Hennig, P., Denk, W., 2007. Point-spread functions for backscattered imaging in the scanning electron microscope. Journal of Applied Physics 102, e123101.

[45] Herculano-Houzel, S., 2009. The human brain in numbers: a linearly scaled-up primate brain. Frontiers in Human Neuroscience 3.

[46] Hiroshi Iwai et al., 2010. Quantification of sofc anode microstructure based on dual beam fib-sem technique. Journal of Power Sources 195, 955–965.

[47] Holzer, L., Cantoni, M., 2011. Review of FIB tomography. Oxford University Press.

[48] Hooke, R., 1665. Micrographia. Dover Publications.

[49] J. S. Earl et al., 2010. Characterization of dentine structure in three dimensions using fib-sem. Journal of Microscopy 240 (1), 1–5.

[50] J.C. Thaemert, 1966. Ultrastructural interrelationships of nerve processes and smooth muscle cells in three dimensions. Journal of Cell Biology 28 (1), 37–49.

[51] Jellinger K et al. , 1992. Iron-melanin complex in substantia nigra of parkinsonian brains: an x-ray microanalysis. Journal of Neurochemistry 59 (3), 1168–71.

[52] Joachim Mayer et al., 2007. Tem sample preparation and fib-induced damage. MRS Bulletin 32, 400–407.

[53] John A. Kiernan, 2000. Formaldehyde, formalin, paraformaldehyde and glutaraldehyde: What they are and what they do. Microscopy Today 8, 8–12.

[54] John J. Bozzola, L. D. R., 1992. Electron Microscopy: Principles and Techniques for Biologists. Springer.

[55] J.T.L. THONG, K.W. LEE, W.K. WONG, 2001. Reduction of charging effects using vector scanning in the scanning electron microscope. Scanning 23 (6), 395–402.

[56] Juan Morales et al., 2011. Espina: a tool for the automated segmentation and counting of synapses in large stacks of electron microscopy images. Journal of Applied Physics 5 (18).

[57] K. SCOTT, 2011. 3d elemental and structural analysis of biological specimens using electrons and ions. Journal of Microscopy 242 (1), 86–93.

[58] K. SCOTT & N.W.M. RITCHIE, 2009. Analysis of 3d elemental mapping artefacts in biological specimens using monte carlo simulation. Journal of Microscopy 233 (2), 331–9.

[59] Karel Svoboda, Ryohei Yasuda, 2006. Principles of two-photon excitation microscopy and its applications to neuroscience. Neuron 50 (6), 823–839.

[60] Kaye, Laby, 1995. Tables of Physical & Chemical Constants. National Physics Laboratory.

[61] Kenji Garno, 1996. Nanofabrication by fib. Microelectronic Engineering 32 (1–4), 159–171.

[62] K.R. Rao, D. N. Kim, J., 2010. Fast Fourier Transforms: Algorithms and Applications. Springer.

[63] Kreyszig, E., 2006. Advanced Engineering Mathematics 9. edition. JOHN WILEY & SONS, INC.

[64] Kuwajima M, Spacek J, H. K., 2013. Beyond counts and shapes: Studying pathology of dendritic spines in the context of teh surrounding neuropil through serial section electron microscopy. Neuroscience 251, 75–89.

[65] L. Holzer et al., 2004. Three-dimensional analysis of porous $batio_3$ ceramics using fib nanotomography. The Journal of Microscopy 216 (1), 84–95.

[66] L. Rayleigh, 1896. Xv. on the theory of optical images, with special reference to the microscope. London, Edinburgh and Dublin Philosophical Magazine and Journal of Science 42 (255), 167–195.

[67] L.A. Giannuzzia, F.A. Stevieb, 1999. A review of focused ion beam milling techniques for tem specimen preparation. Micron 30 (3), 197–204.

[68] Lešer, Vladka and Milani et al., 2010. Focused ion beam (fib)/scanning electron microscopy (sem) in tissue structural research. Protoplasma 246, 41–48.

[69] Lichtman et al., 2008. A technicolour approach to the connectome. Nat Rev Neuroscience 9, 417–22.

[70] Lidia Blazquez-Llorca et al., 2013. FIB/SEM technology and alzheimers disease three dimensional analysis of human cortical synapses. Journal of Alzheimers Disease 34 (4), 995–1013.

[71] Marx, V., 2013. Brain mapping in high resolution. Nature 503, 147–152.

[72] Masaaki Kuwajima, John M. Mendenhall, Kristen M. Harris, 2013. Large-volume reconstruction of brain tissue from high-resolution serial section images acquired by sem-based scanning transmission electron microscopy. Methods Mol Biol. 950, 253–73.

[73] Merli, P., Migliori, A., Nacucchi, M., Antisari, M. V., 1996. Comparison of spatial resolutions obtained with different signal components in scanning electron microscopy. Ultramicroscopy 65 (1–2), 23–30.

[74] Merli, P., Morandi, V., Corticelli, F., 2003. Backscattered electron imaging and scanning transmission electron microscopy imaging of multi-layers. Ultramicroscopy 94, 89–98.

[75] Michael T. Postek et al., 1998. Image sharpness measurement in scanning electron microscopy-part II. Scanning 20 (1), 24–34.

[76] Miroslava Schaffer et al., 2007. Automated three-dimensional x-ray analysis using a dual-beam fib. Ultramicroscopy 107, 587–97.

[77] Moritz Helmstaedter, Kevin L Briggman, W. D., 2008. 3d structural imaging of the brain with photons and electrons. Current Opinion in Neurobiology.

[78] Narayanan Kasthuri, Jeff W Lichtman, 2010. Neurocartography. Neuropsychopharmacology 35 (1), 342–343.

[79] Newbury, D. E., 2002. Barriers to quantitative electron probe x-ray microanalysis for low voltage scanning electron microscopy. Journal of Research of the National Institute of Standards and Technology 107, 605–619.

[80] Peter Gnauck, Peter Hoffrogge, J. G., 2003. A new crossbeam inspection tool combining an ultrahigh resolution field emission SEM and a high resolution FIB. Microscopy and Analysis 94, 11–13.

[81] Probst et al., 2012. Spatial resolution optimization of backscattered electron images using monte carlo simulation. Microscopy and Microanalysis 18 (3), 628–637.

[82] R. Schalek et. al., 2011. Development of high-throughput, high-resolution 3d reconstruction of large- volume biological tissue using automated tape collection ultramicrotomy and scanning electron microscopy. Microsc. Microanal. (Suppl 2) 17, 966–967.

[83] R. Wuhrer, K. Moran, L. M., 2006. Characterization of materials through x-ray mapping. Materials Forum 30, 63–70.

[84] Rebecca Teclemariam-Mesfh, et al., 1997. A simple silver-gold intensification procedure for double dab labeling studies in electron microscopy. The Journal of Histochemistry & Cytochemistry 45 (4), 619–621.

[85] Rene Van Grieken, A. M., 2001. Handbook of X-Ray Spectrometry, Second Edition. CRC Press.

[86] Robert Hovden, Huolin L. Xin, D. A. M., 2011. Extended depth of field for high-

resolution scanning transmission electron microscopy. Microscopy and Microanalysis 17, e2588.

[87] Rykaczewski, K., White, W. B., Fedorov, A. G., 2007. Analysis of electron beam induced deposition (ebid) of residual hydrocarbons in electron microscopy. Journal of Applied Physics 101 (5), e054307.

[88] Scott, K., 2011. Minimizing damage during fib sample preparation of soft materials. Journal of Microscopy 245, 288–301.

[89] Sergio Lozano-Perez, 2008. A guide on fib preparation of samples containing stress corrosion crack tips for tem and atom-probe analysis. Micron 39 (3), 320–8.

[90] Sporns, O., Tononi, G., Ktter, R., 2005. The human connectome: A structural description of the human brain. PLoS Comput Biol 1, e42.

[91] Steffen Maude Fagerland, 2013. Optimizing scanning electron microscope (sem) image sharpness used in focused ion beam (fib) slice and view for the generation of 3d models of brain tissue. NTNU.

[92] Takahiro Sonomura et al., 2013. Correlative analysis of immunoreactivity in confocal laser-scanning microscopy and scanning electron microscopy with focused ion beam milling. Frontiers in Neural Circuits 7 (26), 247–263.

[93] Tina Notter et al., 2014. A protocol for concurrent high-quality immunohistochemical and biochemical analyses in adult mouse central nervous system. European Journal of Neuroscience 39 (2), 165–75.

[94] Toshihiko Ogura, 2008. A high contrast method of unstained biological samples under a thin carbon film by scanning electron microscopy. Biochemical and Biophysical Research Communications 377, 79–84.

[95] Uchic, M. D., Groeber, M. A., Dimiduk, D. M., Simmons, J., 2006. 3d microstructural characterization of nickel superalloys via serial-sectioning using a dual beam FIB-SEM. Scripta Materialia 55, 23–28.

[96] V. LEŠER et al., 2009. Comparison of different preparation methods of biological

samples for FIB milling and SEM investigation. Journal of Microscopy 233, 309–19.

[97] Villinger, Clarissa and Gregorius et al., 2012. FIB/SEM tomography with TEM-like resolution for 3d imaging of high-pressure frozen cells. Histochemistry and Cell Biology 138, 549–56.

[98] W. K. Wong, J. C. H. Phang andJ. T. L. Thong, 1995. Charging control using pulsed scanning electron microscopy. Scanning 17 (5), 312–315.

[99] Weilie Zhou, Z. L. W., 2007. Scanning Microscopy for Nanotechnology, Techniques and Applications. Springer.

[100] Werner Gbel, Bjrn M Kampa, Fritjof Helmchen, 2007. Imaging cellular network dynamics in three dimensions using fast 3d laser scanning. Nature Methods 4, 73–79.

[101] Weston, A. E., Armer, H. E. J., Collinson, L. M., 2010. Towards native-state imaging in biological context in the electron microscope. Journal of Chemical Biology 3, 101–12.

[102] Winfried Denk, H. H., 2004. Serial block face scanning electron microscopy to reconstruct three-dimensional tissue nanostructure. PLoS Biol 2 (11), e329.

[103] Wirth, R., 2009. Focused ion beam (fib) combined with {SEM} and tem: Advanced analytical tools for studies of chemical composition, microstructure and crystal structure in geomaterials on a nanometre scale. Chemical Geology 261, 217–229.

[104] Xiaobing Chen, Christine A. Winters, Thomas S. Reese, 2008. Life inside a thin section: Tomography. The Journal of Neuroscience 28 (38), 9321–9327.

[105] Yao, N., 2011. Focused Ion Beam Systems. Cambridge.

[106] Z Liposits, T Gö rcs and K Trombità s, 1985. Ultrastructural analysis of central serotoninergic neurons immunolabeled by silver-gold-intensified diaminobenzidine chromogen. completion of immunocytochemistry with x-ray microanalysis. Journal of Histochemistry & Cytochemistry 33 (6), 604–10.

[107] Zhiming M. Wang, 2013. Fib nanostructures. Lecture Notes in Nanoscale Science and Technology 20.